IMPROVING CARDIOVASCULAR SIMULATIONS SPEED AND ACCURACY THROUGH ADVANCEMENTS IN NUMERICAL METHODS

A Dissertation

Presented to the Faculty of the Graduate School

of Cornell University

in Partial Fulfillment of the Requirements for the Degree of

Doctor of Philosophy

by

Dongjie Jia

December 2024

IMPROVING CARDIOVASCULAR SIMULATIONS SPEED AND ACCURACY THROUGH ADVANCEMENTS IN NUMERICAL METHODS

Dongjie Jia, Ph.D.

Cornell University 2024

The growing use of cardiovascular simulations for diagnosis and surgical planning is facilitated by constant advancements in numerical methods and modeling. This dissertation is a collection of three studies, two of which introduced improvements to the current CFD solver that improves the solution accuracy and speed, while the last study uses CFD simulations to perform a parametric optimization study, all in relation to cardiovascular flow. The first study introduced a method to perform cardiovascular CFD simulations in the Fourier domain. The growing use of cardiovascular simulations for diagnosis and surgical planning requires faster computational methods than those currently available. To address this need, we leverage the periodic nature of these flows by discretizing equations in terms of Fourier modes instead of time steps. This approach, known as the harmonic balance method, significantly reduces the size of the discrete problem and hence the simulation cost. In our study, we introduce a harmonic balance finite element solver for simulating physically stable time-periodic flows. The proposed solver is formulated using the baseline Galerkin's method with a least-squares stabilization term. The solver is tested on three physiological cases: a Glenn operation pulmonary arteries flow, a cerebral arteries flow, and a left main coronary arteries flow, against a conventional time-stepping solver. We demonstrate that simulations using the harmonic balance solver all converged around 30 minute, while cases run with the conventional time solver takes more than ten hours, resulting in 10 to 100 times simulation speedup. We compared the solutions between the proposed and conventional solvers and found that the results are very similar, with a margin of around 5%.

The second study proposed a new stabilization formulation for the streamline upwind Petrov-Galerkin finite element method. Several finite element methods for simulating incompressible flows rely on the streamline upwind Petrov-Galerkin stabilization (SUPG) term, which is weighted by τ_{SUPG}. The conventional formulation of τ_{SUPG} includes a constant that depends on the time step size, producing an overall method that becomes exceedingly less accurate as the time step size approaches zero. In practice, such method inconsistency introduces significant error in the solution, especially in cardiovascular simulations, where small time step sizes may be required to resolve multiple scales of the blood flow. To overcome this issue, we propose a consistent method that is based on a new definition of τ_{SUPG}. This method, which can be easily implemented on top of an existing streamline upwind Petrov-Galerkin and pressure stabilizing Petrov-Galerkin method, involves the replacement of the time step size in τ_{SUPG} with a physical time scale. This time scale is calculated in a simple operation once every time step for the entire computational domain from the ratio of the L^2-norm of the acceleration and the velocity. The proposed method is compared against the conventional method using four cases: a steady pipe flow, a blood flow through vascular anatomy, an external flow over a square obstacle, and a fluid-structure interaction case involving an oscillatory flexible beam. These numerical experiments, which are performed using linear interpolation functions, show that the proposed formulation eliminates the inconsistency issue associated with the conventional formulation in all cases. While the proposed method is slightly more costly than the conventional method, it significantly reduces the error, particularly at small time step sizes. For the pipe flow where an exact solution is available, we show the conventional method can over-predict the pressure drop by a factor of three. This large error is almost completely eliminated by the proposed formulation, dropping to approximately 1% for all time step sizes and Reynolds numbers considered.

The third study introduces an algebraic model informed by computational fluid dynamics (CFD) simulations to investigate the performance of the assisted bidirectional

Glenn (ABG) operation on a broad range of conditions. The performance of this operation, as measured by the superior vena cava (SVC) pressure, depends on the nozzle area in its ejector pump and the patient's pulmonary vascular resistance (PVR). Using the developed algebraic model to explore this two-dimensional parameter space shows that the ejector pump can create a pressure difference between the pulmonary artery and the SVC as high as 5 mmHg. The lowest SVC pressure is produced at a nozzle area that decreases linearly with the PVR such that, at PVR = 4.2 (Wood units-m^2), there is no added benefit in utilizing the ejector pump effect (optimal nozzle area is zero, corresponding to the bidirectional Glenn circulation). At PVR = 2 (Wood units-m^2), the SVC pressure can be lowered to less than 4 mmHg by using an optimal nozzle area of $\approx$ 2.5 mm^2. Regardless of the PVR, adding a 2 mm^2 nozzle to the baseline bidirectional Glenn boosts the oxygen saturation and delivery by at least 15%. The SVC pressure for that 2 mm^2 nozzle remains below 14 mmHg for all PVRs less than 7 Wood units-m^2. The mechanical efficiency of the optimal designs consistently remains below 30%, indicating the potential for improvement in the future. A good agreement is observed between the algebraic model and high-fidelity CFD simulations.

BIOGRAPHICAL SKETCH

Dongjie (Fred) Jia is a PhD candidate in Mechanical Engineering at Cornell University. Prior to the doctorate program, he received a M.Sc. degree in Mechanical Engineering at Cornell University and a B.Sc. degree in Mechanical Engineering at Rensselaer Polytechnic Institute. His early researches focused on the application of CFD simulation to understanding cardiovascular flows, in particular in surgical outcome prediction, procedural design, and flow optimization. Fred's doctorate work focus on constructing CFD methods and solvers to improve simulation accuracy and speed, with applications to cardiovascular simulations.

This dissertation is dedicated to you, the reader, for taking an interest in my work.

ACKNOWLEDGEMENTS

I am incredibly thankful to my advisor and the chair of my committee, Professor Mahdi Esmaily, for his unwavering patience, encouragement, and guidance throughout my program. I also want to express my gratitude to my defense committee members, Professor Olivier Desjardins and Professor Peter J. Diamessis, for generously sharing their knowledge, feedback, and insights.

I am also thankful for the support and collaboration of my peers during my program, particularly my lab mates Dr. Grant Rydquist, Saba Mansour, Priscilla Chang, and many others.

Finally, I want to extend my heartfelt thanks to my family, including my parents and my wife, Hanyu Chen, who inspires me daily. And last but not least, I am grateful to my cat Minerva for all the entertainment.

TABLE OF CONTENTS

LIST OF TABLES

LIST OF FIGURES

CHAPTER 1

INTRODUCTION

Heart disease is the leading cause of death in the United States, accounting for approximately 1 in 5 deaths [188]. The annual cost of heart disease in the United States exceeds 250 billion dollars, including expenses related to healthcare, medications, and lost productivity [182]. Significant resources have been invested in the diagnosis, analysis, and treatment of heart disease. Investigating and understanding the hemodynamics of the cardiovascular system—such as pressure distribution, flow patterns, turbulence, and stagnation—has been an essential component in understanding heart functionality and disease [152, 115]. Unfortunately, clinical methods alone have been inefficient in obtaining this information, especially when limited to non-invasive measurements. Historically, the only non-invasive measurements of blood hemodynamics have been blood pressure and cardiac output [3, 35]. In conjunction with blood biomarker measurements, diagnoses are typically inferred using clinical experience and predictive models [136, 195]. Recent advancements in 4D flow magnetic resonance imaging (MRI) have enabled additional non-invasive clinical measurements of blood hemodynamics, most notably flow velocity [109, 163]. However, the equipment required for 4D MRI measurements is expensive to purchase and maintain, making it inaccessible for many hospitals and patients. Even with 4D MRI, many parameters—such as pressure distribution, wall shear stress, and shear rate—remain inaccessible through non-invasive clinical measurements. Furthermore, predicting surgical hemodynanics outcomes, which requires performing virtual surgery and simulations, is not feasible using current clinical methods.

Since the late 20th century, flow simulations using computational fluid dynamics (CFD) have seen exponential growth owing to the advances in hardware capabilities and numerical methods [55, 102, 77, 18]. CFD was utilized for performing cardiovascular simulations since as early as the 1990s [173, 174, 171]. Blood flow simulations provide

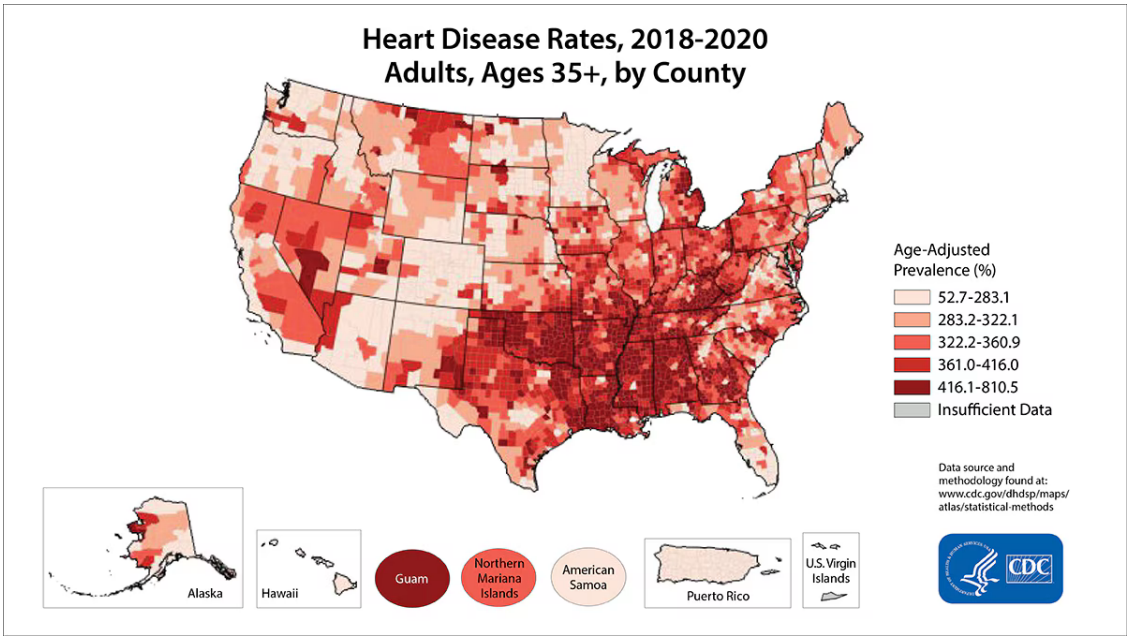

Figure 1.1: Heart Disease Death Rates, 2018–2020 for Adults, Ages 35+, by County. Retrieved from CDC website. [63]

hemodynamic information that is otherwise clinically unobtainable, enhancing our understanding of various cardiovascular systems and diseases. Early cardiovascular simulations used idealized geometries of the cardiovascular system due to limited computational power and difficulties in acquiring realistic geometries [170]. These early idealized simulations offered valuable insights into circulation patterns, but often ignored patient-specific variations. More recently, advances in medical imaging, image processing, and computational hardware and software have made cardiovascular simulation a viable tool for patient-specific diagnosis and surgical planning [89, 196]. These simulations can provide detailed, realistic spatiotemporal flow information of a patient's circulatory system for both diagnosis and potential surgical outcomes, with the help of virtual surgeries using computer-aided design (CAD) software [128, 160].

Performing a cardiovascular simulation for a patient involves several steps: obtaining a patient-specific model, conducting the CFD simulation, and post-processing to analyze the results and correlate them with clinical diagnoses or predictions. Currently, the bulk of the time is consumed by the first two steps, each of which can take hours or even days. Obtaining a patient-specific three-dimensional model is crucial for accurate personalized diagnosis and treatment, as variations in cardiovascular geometry between patients can significantly impact simulation outcomes and flow dynamics. Advancements in imaging tools and software have contributed to rapid progress in this area [108, 41, 153, 109]. Over the past three decades, the rapid advancement of non-invasive imaging techniques such as computed tomography (CT), positron emission tomography (PET), and magnetic resonance imaging (MRI) has provided clinicians and researchers with unprecedented high-resolution spatial images of the heart and vasculature [37, 159]. Segmenting these images to generate three-dimensional models is challenging due to image noise and the inherent variability of cardiovascular geometries among patients, which sometimes requires significant manual hours. Specialized algorithms have been instrumental in performing auto-segmentation on various parts of the cardiovascular system [137, 140]. However, these algorithms are often limited to specific regions or applications and typically take around 2 to 3 hours to complete [26]. More recently, rapid advancements in artificial intelligence over the past several years have paved the way for developing deep learning-based segmentation methods [134, 29]. For these methods, most of the computational cost is incurred during model training, which can be conducted as a preliminary step in research settings. Once trained, applying these models for segmentation in clinical settings typically takes less than one second [8, 27, 72]. With ongoing research in auto-segmentation, these costs will continue to decrease.

Currently, the majority of the cost associated with performing cardiovascular simulations is attributed to the computational expense of the CFD solver. Early adopters of CFD utilized finite volume and finite difference methods [55, 102]. Recently, the finite element

method has become more commonly used for cardiovascular simulations [169]. The finite element method offers the advantage of better handling unstructured meshes, making it more suitable for patient-specific geometries [184, 14]. Additionally, implementing fluid-structure interaction (FSI) to model heart muscle or blood vessel movements is relatively straightforward using the finite element method [15, 145]. The finite element method for fluid flow solves the weak form of the Navier-Stokes equations, and when spatially discretized, it results in the Galerkin form of the Navier-Stokes equations. The numerical solution using the Galerkin form is inherently unstable in advection-dominant flows, necessitating a stabilization scheme to counteract these numerical instabilities [23, 79, 156, 64]. The stabilization scheme is crucial for ensuring numerical stability and solution accuracy in finite element methods. A commonly used early stabilization method is the streamline upwind Petrov–Galerkin and pressure-stabilizing Petrov–Galerkin (SUPG/PSPG) formulation [23]. This stabilization is inspired by the upwind scheme used in finite difference methods. Streamline-upwind stabilization is formulated as an artificial diffusion, where the diffusivity is determined based on the streamline velocity and a stabilization parameter, τ. The value of τ is analytically derived from the solution of the steady advection-diffusion equation, ensuring that the nodal solution of the finite element method matches the analytical solution [79, 156]. Pressure stabilization is incorporated into the continuity equation, allowing for equal-order shape functions to be used for both the velocity and pressure fields. Over the decades, more advanced stabilization methods have evolved from the SUPG/PSPG stabilization. In this dissertation, in addition to the SUPG/PSPG method, we also employ the Galerkin least-square stabilization, which utilizes the differential operator of the governing equations to construct the stabilization term [56], and the residual-based variational multiscale method, which uses stabilization terms to model sub-grid scale turbulence [2, 10].

One challenge with the stabilized method is designing the stabilization parameter τ for unsteady equations. Conventional stabilization methods typically use a form of τ that

includes an acceleration contribution proportional to the time step size, Δt [79, 156]. This term makes the solution of the stabilized finite element solver dependent on the chosen time step size. This time-step dependency is not significant when the simulation's CFL number is around 1. However, when a very small time step is used, resulting in a low CFL number, the solution tends to diverge as the time step approaches zero. This issue is common in cardiovascular simulations, as the complexity of the geometry and flow conditions often necessitates using small time step sizes. Our numerical experiments demonstrated that the solver built with the conventional stabilization formulation can over-predict results by threefold in certain extreme cases. Chapter 3 of this dissertation, published in Scientific Reports [88], aims to address this time step size inconsistency issue. We proposed a new design for the stabilization parameter τ, which calculates the acceleration term contribution based on the physical properties of the fluid field. This formulation ensured that the stabilization parameter is independent of the time step size. We showed that the new formulation reduced solution variation to within 1% when the time step size changed by two orders of magnitude.

Other than the challenges related to the numerical accuracy of CFD results, one of the biggest challenges in using cardiovascular simulations in clinical settings remains the high computational cost. Currently, state-of-the-art high-accuracy cardiovascular CFD simulations typically require more than 5,000 CPU hours [52, 90, 111]. Existing efforts have focused on reducing the complexity of simulations to lower costs. One approach to achieve this is by reducing the size of the discretized mesh while preserving solution accuracy. This can be accomplished by using a physics-based mesh generation strategy that minimizes the total number of elements used without compromising overall accuracy [100, 90]. The cardiovascular system exhibits drastically different hemodynamics at various locations within the fluid domain. To capture the full complexity of the flow, a uniform mesh typically requires very small element sizes. However, this fine resolution may not be necessary in regions with non-complex flow, such as in the pulmonary arter-

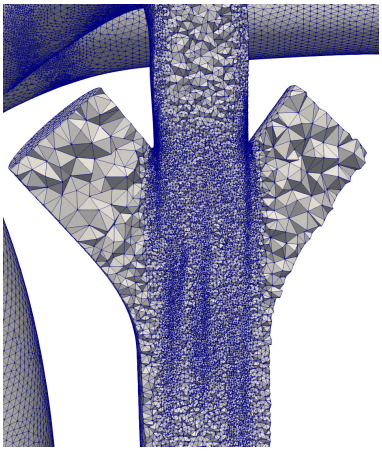

Figure 1.2: Example of mesh generated from the physics-based mesh generation method. The physical flow field is shown in Figure 1.3

ies. The physics-based mesh generation approach allows the fluid domain to be meshed according to the physical complexity of the flow (Figure 1.2 and 1.3). Given that cardiovascular CFD simulations use the finite element method with linear shape functions, the leading source of error in the fluid field is associated with the second derivative of the velocity field. The second derivative at each node can be estimated using values from adjacent nodes. With this information, the mesh is iteratively reconstructed, where the remeshed edge length is prescribed as inversely proportional to the error estimation. This method ensures mesh-independent solutions by limiting maximum local error while requiring significantly fewer elements than a uniform mesh. Consequently, this approach reduces overall simulation costs, especially when the mesh is used for multiple simulations.

Another approach to reduce simulation costs is through reduced-order modeling of the cardiovascular system. One of the earliest reduced-order model of the cardiovascular system is the lumped parameter network (LPN), where blood vessels are represented as resistors, capacitors, and inductors to simulate physical pressure head loss, vessel dilation, and external forces, respectively [104]. This modeling approach has been used in conjunction with CFD to reduce system complexity or even as a replacement for

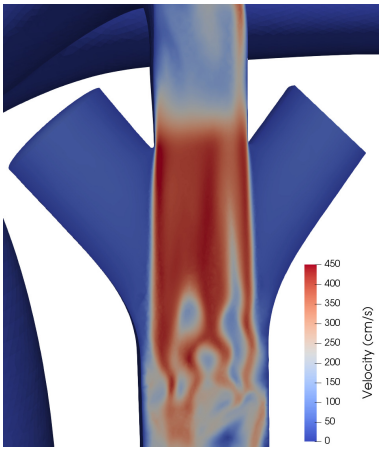

Figure 1.3: Velocity field which the physics-based mesh generation was based on. The mesh generated is shown in Figure 1.2

CFD [127, 111]. When used in conjunction with CFD, the lumped parameter network serves as a closed-loop system to model whole-body blood flow and provides realistic boundary conditions for the CFD domain (Figure 1.4). The high accuracy multi-domain CFD-LPN results can be used to further construct reduced order models for specific cardiovascular cases and inform surgical parameterization and optimization. In Chapter 4 of this dissertation, we developed a CFD-based reduced-order model that was built on conservation laws. This work was published in MDPI Fluids[87] and was a continuation of my master's research[90], which proposed a new surgical procedure and demonstrated its effectiveness using multi-domain CFD simulations. The scope of the reduced-order model was limited to a specific proposed surgical procedure under varying patient physiological conditions. The constructed reduced-order model can be used to support clinical decision-making. The primary drawback of the reduced-order model is the high cost associated with training. In this study, we used a total 15 CFD simulations to inform the model, which simultions took 30 days to run in parallel on 288 processors. More recently, data-driven machine learning has been considered as a potential replacement for CFD simulations [175, 103, 154]. However, such models require even more training data to develop, typically on the order of 100 CFD simulations or extensive clinical data [122, 57]. Overall, current reduced-order models suffer from three major drawbacks compared to

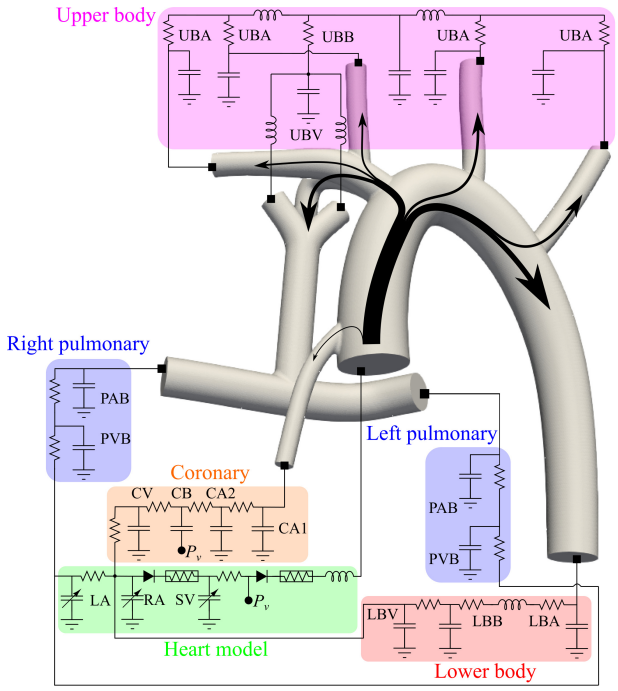

Figure 1.4: Example of lumped parameter network modeling the whole body blood flow coupled with CFD domain for a realistic multi-domain simulation. This simulation is performed in Chapter 4.

CFD simulations: limited personalization and flexibility, extensive data requirements for training, and lack of adherence to fundamental conservation laws, making them prone to significant errors.

For real-time patient-specific diagnosis or surgical outcome prediction, the simulation turnaround time must be within a few hours and run on a clinically accessible hardware, typically a desktop computer with around 10 CPU cores. This indicates that there is still a two- to three-order-of-magnitude gap in computational time between current CFD capabilities and the desired cost for clinical adoption. In a series of our recent studies, we proposed simulating cardiovascular flows in the time-spectral (frequency) domain rather than the time domain to address the cost constraints of cardiovascular simulations while preserving the benefits of CFD. Physically stable cardiovascular flows exhibit periodic and smooth temporal behavior, allowing their behavior to be approximated using fewer than ten frequency modes. By solving for selective frequency modes, we can significantly

reduce simulation costs compared to conventional time-stepping CFD, which often requires tens of thousands of time steps to achieve cycle-to-cycle convergence. Constructing the frequency finite element Navier-Stokes solver involved several studies, beginning with a specialized code structure to separate complex values and incorporate a pressure stabilization scheme [117, 45]. We also introduced a new finite element stabilization method to improve solution accuracy and tested it against existing approaches [44, 46]. Chapter 2 represents the most recent work in this series and marks the first comprehensive effort to construct a frequency solver with favorable linear cost scaling in relation to frequency modes. We achieved this by combining the harmonic balance method with the stabilized finite element method to solve the Navier-Stokes equations. The efficacy of our proposed harmonic balance solver is demonstrated through three different cardiovascular cases with patient-specific anatomy, and the results were compared to those obtained using a conventional time-stepping CFD solver. The goal is to demonstrate that the proposed frequency solver is ready for application in various physiological flow cases, paving the way for its potential future use. This work is planned to be submitted to the Journal of Biomechanical Engineering considering the proposed solver's physiological relevance and application potential.

The three studies included in this thesis are ordered as followed: Chapter 2 presents the details on the study on constructing a harmonic balance finite element solver and the related numerical experiments, Chapter 3 presents the improved stabilization parameter formulation for the stablized finite element method which fixed the solution consistencey issue related to change in time step size, Chapter 4 is the CFD-based reduced order model parametric study on a surgical procedure. We will conclude this dissertation in Chapter 5 and discuss the relation between these works, the remaining challenges, and possible future directions.

CHAPTER 2

ACCELERATING CARDIOVASCULAR CFD SIMULATIONS WITH A HARMONIC BALANCE FINITE ELEMENT SOLVER FOR THE NAVIER-STOKES EQUATIONS

2.1 Introduction

Computational Fluid Dynamics (CFD) has been foundational to cardiovascular studies in the recent decades [173, 59, 127, 130]. Cardiovascular flow simulations using CFD provide a non-invasive way of accessing information that is difficult or impossible to obtain using conventional clinical methods. Simulation results such as flow paths, pressure distribution, and wall shear stress can provide critical information for non-invasive diagnosis [4, 96, 30, 123], predictive surgical planning [139, 53, 89], and surgical optimisation [52, 110, 87]. Unfortunately, the applications are mainly limited to research settings due to the cost of performing high-accuracy simulations, which can take hours or days to run on a dedicated computing cluster [181, 90]. In real-life clinical settings where patient-specific simulations are considered, the cost becomes prohibitive because the computational resources are limited and the decision-making time is short.

At the current state, performing CFD simulations in clinical settings requires simplifying the flow condition, most commonly by assuming steady-state flow, for example, in most simulation-driven fractional flow reserve (FFRCFD, FFRCT) [172, 39, 124]. This assumption reduces the CFD simulation's convergence cost but significantly impacts the result accuracy since cardiovascular flows are inherently unsteady and cyclic. The steady-state assumption does not capture the dynamical behavior during a cardiac cycle, resulting in large errors in estimating parameters such as pressure, flow rate, and wall shear stress. Other speedup methods circumvent performing CFD in clinical settings altogether, such as reduced order modeling [104, 131, 142], and more recently, data-driven machine

learning [175, 103, 154]. In these methods, CFD simulations are performed beforehand, and the results are used to build CFD-informed models [122, 57]. The models constructed are cost-efficient for use in clinical settings. However, they often struggle to accommodate patient-specific variations in conditions or geometries. More importantly, these models do not yield the same full temporal-spacial results as CFD, nor are they inherently designed to satisfy conservation laws essential for ensuring physical validity.

To address the cost constraint of cardiovascular simulations while preserving the full advantages of CFD, we proposed simulating these flows in a time-spectral (or frequency) domain in a series of our recent work [117, 45, 44, 46]. Physically stable cardiovascular flows are periodic and vary smoothly in time; thus, their temporal behavior can be well-approximated using a few frequency modes. Solving those selective frequency modes can reduce the simulation cost significantly compared to conventional time-stepping CFD, which requires hundreds of time steps to represent one cardiac cycle and tens of thousands of time steps to reach cyclic solution convergence. The implementation of the frequency finite element solver requires several innovative approaches, starting with a specialized code structure to separate the complex values to strictly use real arithmetics in the solver, and a pressure stabilization scheme to allow equal shape functions for pressure and velocity [117, 45]. In addition, a new finite element stabilization method was proposed to improve solution accuracy and was tested against other existing stabilization methods in solving the frequency convection-diffusion equation [44].

The stabilized finite element method is widely used for cardiovascular simulations, owing to its convenience in dealing with complex geometries, unstructured grid, and modeling fluid-structure interaction [184, 15, 145, 94]. In our most recent work, we introduced a CFD solver that uses a specialized stabilized finite element method to solve the Navier-Stokes equation in frequency [46]. The requirements for performing a simulation using the frequency stabilized finite element solver are the same as those for a

conventional CFD solver: given boundary conditions and a volumetric mesh. The outlet flow rate and pressure results were accurate to less than 5% of that of a conventional CFD while achieving significant speedup in simulation time. Despite these favorable results, the previous study's most significant drawback is that the simulation cost scales quadratically with the number of simulated frequency modes. This cost scaling diminishes the cost-saving advantages of the frequency solver when a large number of frequency modes is required for a simulation.

Previously, the idea of solving unsteady non-linear equations in the frequency domain has been extensively studied in the field of harmonic balance methods. The harmonic balance method is a frequency domain method to used to calculate the frequency response without the need for time integration. [147] It is particularly widely used for simulating strong nonlinear behaviors such as mechanical vibration and nonlinear electrical circuits [190, 166]. Harmonic balance CFD simulations have been used in aerospace and turbomachinery applications using the finite volume and the finite difference methods [114, 83, 68, 161, 70, 5, 82]. However, using the harmonic balance method for simulating cardiovascular flow was only mentioned in one conference proceeding and has not been comprehensively considered [97]. In this paper, we will take advantage of the harmonic balance form of the Navier-Stokes equations proposed in a harmonic balance CFD paper [71]. The harmonic balance Navier-Stokes equations is a direct transform of the frequency Navier-stokes equations used in our previous study [46]. The harmonic balance form of the equations has the advantage of containing only real-valued variables and allowing approximately linear cost-scaling with the number of frequency modes.

To the best of our knowledge, this is the first paper that combines the harmonic balance method with the stabilized finite element method to solve the Navier-Stokes equations. We will simulate three different cardiovascular cases with patient-specific anatomy: a Glenn procedure pulmonary flow, a cerebral flow, and a coronary artery flow with the

proposed harmonic balance solver and compare the results to that of a conventional time-stepping CFD solver. These cases, each with its unique clinical significance and hemodynamic flow patterns, will serve as compelling examples to demonstrate the efficacy of the proposed harmonic balance solver. We aim to demonstrate that our proposed solver is ready for application in various physiological cases, paving the way for its potential use in future studies. This paper is organized as follows: We will first introduce the derivation of the harmonics-balance Navier-Stokes equation and present the stabilized finite element method used. We will then give comprehensive details about the solution procedure to solve the system of equations. We will use the results obtained from the three cardiovascular cases to demonstrate the harmonic balance solver's cost and accuracy relative to the conventional solver. Lastly, we will discuss the implications of the results, the existing limitations, and future works.

2.2 Methods

This section details the numerical methods used to construct the proposed harmonic balance CFD solver, beginning with deriving the governing equations: the harmonic balance Navier-Stokes equations. We will then formulate the stabilized finite element weak form used in this study and briefly discuss other common stabilization methods. Lastly, we will provide the solution procedure to solve the resulting system of equations to achieve optimal speed and cost scaling. This section provides sufficient details for readers to modify an existing conventional finite element solver to solve the harmonic balance Naiver-Stokes equations.

2.2.1 Harmonic balance Navier-Stokes equations

In this study, the fluid (blood) is incompressible. The blood is considered Newtonian since the length scale of the major blood vessels is significantly larger than the length scale of a red blood cell. In addition, we are only considering non-moving walls. Future studies are required to extend our method to include fluid-structure interactions.

With these assumptions, the three-dimensional incompressible Navier-Stokes equation in the Cartesian coordinate system and the time domain is formulated as

$$\begin{aligned}
\rho\frac{\partial \hat{u}_i}{\partial t} + \rho\hat{u}_j\frac{\partial \hat{u}_i}{\partial x_j} &= -\frac{\partial \hat{p}}{\partial x_i} + \frac{\partial}{\partial x_j}\left(\mu\frac{\partial \hat{u}_i}{\partial x_j}\right), && \text{in} \quad \Omega \times (0, N_c T] \\
\frac{\partial \hat{u}_i}{\partial x_i} &= 0, && \text{in} \quad \Omega \times (0, N_c T] \\
\hat{u}_i &= \hat{g}_i, && \text{on} \quad \Gamma_{\mathrm{g}} \times (0, N_c T] \\
-\hat{p}n_i + \mu\frac{\partial \hat{u}_i}{\partial x_j}n_j &= \hat{h}n_i, && \text{on} \quad \Gamma_{\mathrm{h}} \times (0, N_c T]
\end{aligned} \tag{2.1}$$

where subscripts i and j denotes the spatial orientation where $i, j = 1, 2, 3$. $\rho \in \mathbb{R}^+$ and $\mu \in \mathbb{R}^+$ are the fluid density and dynamic viscosity, respectively, and $\hat{u}_i(\boldsymbol{x}, t) \in \mathbb{R}$ and $\hat{p}(\boldsymbol{x}, t) \in \mathbb{R}$ are the unknown fluid velocity and pressure, respectively, at position $\boldsymbol{x}$ and time t. Ω denotes the entire computational domain, and Γ_{h} and Γ_{g} are the portion of the boundary where a Neumann and Dirichlet boundary condition is imposed, respectively. $\hat{g}_i(\boldsymbol{x}, t) \in \mathbb{R}$ and $\hat{h}(\boldsymbol{x}, t) \in \mathbb{R}$ are the imposed Dirichlet and Neumann boundary conditions, respectively, and N_c and T are the number and duration of cardiac cycles. n_j denotes the normal direction at the Neumann boundaries. Note that the Neumann boundary condition is simplified by decoupling the velocity components, which is common for cardiovascular applications [186, 12, 46].

To write (2.1) in the frequency domain, we take advantage of the underlying frequency of the flow field, $\omega = 2\pi/T$, calculated from the duration of the cardiac cycle. With this knowledge, we can write the solution and boundary conditions in a discretized and trun-

cated frequency form up to the M-th frequency mode as

$$\begin{aligned}
\hat{u}_i(\boldsymbol{x},t) &= \sum_{|m|<M} u^*_{mi}(\boldsymbol{x}) e^{\hat{i}m\omega t}, \\
\hat{p}(\boldsymbol{x},t) &= \sum_{|m|<M} p^*_{m}(\boldsymbol{x}) e^{\hat{i}m\omega t}, \\
\hat{g}_i(\boldsymbol{x},t) &= \sum_{|m|<M} g^*_{mi}(\boldsymbol{x}) e^{\hat{i}m\omega t}, \\
\hat{h}(\boldsymbol{x},t) &= \sum_{|m|<M} h^*_{m}(\boldsymbol{x}) e^{\hat{i}m\omega t},
\end{aligned} \tag{2.2}$$

where

$$\begin{aligned}
g^*_{mi}(\boldsymbol{x}) &\coloneqq \frac{1}{T}\int_0^T \hat{g}_i(\boldsymbol{x},t) e^{-\hat{i}m\omega t} dt, \\
h^*_{m}(\boldsymbol{x}) &\coloneqq \frac{1}{T}\int_0^T \hat{h}(\boldsymbol{x},t) e^{-\hat{i}m\omega t} dt,
\end{aligned}$$

are the Fourier coefficients computed such that the spectral content of the boundary conditions is exact up to the M-th mode. This way, the error associated with discretizing the boundary conditions in (2.2) scales with the frequency content of the truncated terms and is minimized. The asterisk (*) denotes the variables in frequency and $\hat{i} = \sqrt{-1}$.

To write the frequency Navier-Stokes equation in a compact matrix form, we organize unknowns and boundary conditions in vectors as

$$\boldsymbol{u}^*_i(\boldsymbol{x}) \coloneqq \begin{bmatrix} u^*_{(-M+1)i} \\ \vdots \\ u^*_{0i} \\ \vdots \\ u^*_{(M-1)i} \end{bmatrix}, \quad \boldsymbol{p}^*(\boldsymbol{x}) \coloneqq \begin{bmatrix} p^*_{-M+1} \\ \vdots \\ p^*_{0} \\ \vdots \\ p^*_{M-1} \end{bmatrix}, \quad \boldsymbol{g}^*_i(\boldsymbol{x}) \coloneqq \begin{bmatrix} g^*_{(-M+1)i} \\ \vdots \\ g^*_{0i} \\ \vdots \\ g^*_{(M-1)i} \end{bmatrix}, \quad \boldsymbol{h}^*(\boldsymbol{x}) \coloneqq \begin{bmatrix} h^*_{-M+1} \\ \vdots \\ h^*_{0} \\ \vdots \\ h^*_{M-1} \end{bmatrix}. \tag{2.3}$$

With these definitions, (2.1) is expressed in the frequency domain as

$$\begin{aligned}
\rho\boldsymbol{\Omega}\boldsymbol{u}_i^* + \rho\boldsymbol{A}_j\frac{\partial \boldsymbol{u}_i^*}{\partial x_j} &= -\frac{\partial \boldsymbol{p}^*}{\partial x_i} + \frac{\partial}{\partial x_j}\left(\mu\frac{\partial \boldsymbol{u}_i^*}{\partial x_j}\right), && \text{in} \quad \Omega \\
\frac{\partial \boldsymbol{u}_i^*}{\partial x_i} &= 0, && \text{in} \quad \Omega \\
\boldsymbol{u}_i^* &= \boldsymbol{g}_i^*, && \text{on} \quad \Gamma_{\mathrm{g}} \\
-\boldsymbol{p}^* n_i + \mu\frac{\partial \boldsymbol{u}_i^*}{\partial x_j}n_j &= \boldsymbol{h}^* n_i, && \text{on} \quad \Gamma_{\mathrm{h}}
\end{aligned} \tag{2.4}$$

where the frequency-source matrix, $\boldsymbol{\Omega}$, is a diagonal matrix with imaginary entries, $\boldsymbol{\Omega}(j,j) \coloneqq \hat{i}(j-M)\omega$, and $\boldsymbol{A}_i$ is a convolution matrix given as $\boldsymbol{A}_i(j,k) \coloneqq u^*_{(j-k)i}, |j-k| < M$. The constraint $|j-k| < M$ results in zero entries on the top right and bottom left of $\boldsymbol{A}_i$, which eliminates the aliasing effect by preventing the generation of frequency that is equal or higher than M from the nonlinear convective acceleration term.

In our previous paper, we solved equations (2.4) using the finite element method with a specialized stabilization scheme [46]. One of the challenges was the complex form of the frequency equation, which requires a particular code structure to handle the complex arithmetic. But more importantly, the solver yielded quadratic cost scaling due to the full convective mode-coupling matrix $\boldsymbol{A}$ and its resulting stabilization formulation. In other words, the overall computational cost scales with the square of the number of frequency modes, $O(M^2)$. This second-order scaling diminished the frequency formulation's cost advantage as the number of frequencies captured in a simulation increased.

This study uses a transformation proposed in a previous harmonic balance method paper to achieve first-order cost scaling [71]. We write the vectors containing the variables in frequency as discrete Fourier operations

$$\boldsymbol{u}_i^*(\boldsymbol{x}) \coloneqq \boldsymbol{E}\boldsymbol{u}_i(\boldsymbol{x}), \quad \boldsymbol{p}^*(\boldsymbol{x}) \coloneqq \boldsymbol{E}\boldsymbol{p}(\boldsymbol{x}), \quad \boldsymbol{g}_i^*(\boldsymbol{x}) \coloneqq \boldsymbol{E}\boldsymbol{g}_i(\boldsymbol{x}), \quad \boldsymbol{h}^*(\boldsymbol{x}) \coloneqq \boldsymbol{E}\boldsymbol{h}(\boldsymbol{x}), \tag{2.5}$$

where $\boldsymbol{E}$ is the discrete Fourier transform matrix defined as $\boldsymbol{E}(j,k) \coloneqq (1/N)e^{-2\pi\hat{i}jk/N}$, where $j,k = 0,\ldots,N-1$ and $N = 2M-1$. The unknowns and boundary conditions are now vectors that contain variables at N equally spaced time points in a cycle, given as

$$\boldsymbol{u}_i(\boldsymbol{x}) \coloneqq \begin{bmatrix} u_{0i} \\ u_{1i} \\ \vdots \\ u_{(N-1)i} \end{bmatrix}, \quad \boldsymbol{p}(\boldsymbol{x}) \coloneqq \begin{bmatrix} p_0 \\ p_1 \\ \vdots \\ p_{(N-1)} \end{bmatrix}, \quad \boldsymbol{g}_i(\boldsymbol{x}) \coloneqq \begin{bmatrix} g_{0i} \\ g_{1i} \\ \vdots \\ g_{(N-1)i} \end{bmatrix}, \quad \boldsymbol{h}(\boldsymbol{x}) \coloneqq \begin{bmatrix} h_0 \\ h_1 \\ \vdots \\ h_{(N-1)} \end{bmatrix}. \tag{2.6}$$

Plugging equations (2.5) in (2.4) and multiplying all equations by the discrete inverse Fourier transform matrix, $\boldsymbol{E}^{-1}$, gives us the final form of the harmonic balance Navier-Stokes equation as

$$\begin{aligned} \rho \boldsymbol{H}\boldsymbol{u}_i + \rho \boldsymbol{U}_j \frac{\partial \boldsymbol{u}_i}{\partial x_j} &= -\frac{\partial \boldsymbol{p}}{\partial x_i} + \frac{\partial}{\partial x_j}\left(\mu \frac{\partial \boldsymbol{u}_i}{\partial x_j}\right), && \text{in} \quad \Omega \\ \frac{\partial \boldsymbol{u}_i}{\partial x_i} &= 0, && \text{in} \quad \Omega \\ \boldsymbol{u}_i &= \boldsymbol{g}_i, && \text{on} \quad \Gamma_{\mathrm{g}} \\ -\boldsymbol{p} n_i + \mu \frac{\partial \boldsymbol{u}_i}{\partial x_j} n_j &= \boldsymbol{h} n_i, && \text{on} \quad \Gamma_{\mathrm{h}} \end{aligned} \tag{2.7}$$

where $\boldsymbol{H}$ is a zero diagonal time point-coupling matrix where $\boldsymbol{H} = \boldsymbol{E}^{-1}\boldsymbol{\Omega}\boldsymbol{E}$, and $\boldsymbol{U}_i$ is a diagonal convective acceleration matrix where $\boldsymbol{U}_i = \mathrm{diag}\,(\boldsymbol{u}_i)$.

Remarks:

1. The harmonic balance equations in (2.7) is a direct transform of the frequency equations in (2.4) by a discrete inverse Fourier transform operator. Therefore, the solutions from the harmonic balance equations still maintain the numerical characteristics of the frequency equations, including spectral accuracy in terms of the truncated frequency series used to represent the unknown variables.
2. The discretization of the acceleration term comes from writing the solution and boundary conditions in a truncated frequency form, which then are transformed

back to unknowns at equally spaced time points for the harmonic balance equations. This form assumes that the solution only contains integer multiplication frequencies of ω. This assumption is reasonable for cardiovascular flows because the energy in each mode is either directly injected by the boundary condition or produced by mode-mode interaction. However, for some instances, another distinct frequency might be triggered by geometric shape-induced instabilities or turbulence, ω_g, which is not integer multiples of ω. This situation typically arrises when the Reynolds number in the fluid domain reaches or exceeds the transient flow limit at $2,000$ to $3,000$. For these cases, the solutions will not converge to steady values.

3. Other than the time-coupling term, $\rho \boldsymbol{H}\boldsymbol{u}_i$, in equations (2.7), all other terms can be calculated at each time point independent of other time points. This calculation means that the code structure for solving conventional time-domain Navier-Stokes equations can remain mostly unchanged. Furthermore, the fact that $\boldsymbol{H}$ is calculated from two discrete Fourier transform matrices means that a fast Fourier transform routine can be used to make the cost scaling $O(N \log(N))$. The implementation will be explained in the following sections.

2.2.2 Stabilized finite element method

The discrete finite element form of the Naiver Stokes equation, namely the Galerkin form, needs to be stabilized to mitigate nonphysical solution oscillation resulting from discretizing the convective-acceleration and dissipative terms [78, 33, 81], and also a pressure stabilization term to allow the use of equal order shape functions [76, 23]. There have been decades of work that proposed various stabilization methods and formulations for the finite element method [178, 75, 168, 191]. In this study, we chose Galerkin's least square stabilization (GLS), which produces both of these terms and is consistent with the con-

ventional time formulation used for comparison.

The GLS method for the harmonic balance Navier-Stokes equations is stated as finding $\boldsymbol{u}_i^h$ and $\boldsymbol{p}^h$ such that for any test functions $\boldsymbol{w}_i^h$ and $\boldsymbol{q}^h$, we have

$$\begin{aligned}&\left(\boldsymbol{w}_i^h, \rho \boldsymbol{H}\boldsymbol{u}_i^h + \rho \boldsymbol{U}_j \frac{\partial \boldsymbol{u}_i^h}{\partial x_j}\right)_\Omega + \left(\frac{\partial \boldsymbol{w}_i^h}{\partial x_j}, -\boldsymbol{p}^h \delta_{ij} + \mu \frac{\partial \boldsymbol{u}_i^h}{\partial x_j}\right)_\Omega + \left(\boldsymbol{q}^h, \frac{\partial \boldsymbol{u}_i^h}{\partial x_i}\right)_\Omega \\ &+\left(\mathscr{L}_i(\boldsymbol{w}_i^h, \boldsymbol{q}^h), \frac{\boldsymbol{\tau}}{\rho}\mathscr{L}_i(\boldsymbol{u}_i^h, \boldsymbol{p}^h)\right)_{\tilde{\Omega}} = \left(\boldsymbol{w}_i^h, \boldsymbol{h} n_i\right)_{\Gamma_\mathrm{h}},\end{aligned} \tag{2.8}$$

where

$$\mathscr{L}_i(\boldsymbol{u}_i^h, \boldsymbol{p}^h) \coloneqq \rho \boldsymbol{H}\boldsymbol{u}_i^h + \rho \boldsymbol{U}_j \frac{\partial \boldsymbol{u}_i^h}{\partial x_j} + \frac{\partial \boldsymbol{p}^h}{\partial x_i} - \frac{\partial}{\partial x_j}\left(\mu \frac{\partial \boldsymbol{u}_i^h}{\partial x_j}\right),$$

is the momentum equation differential operator. The inner product notation for two vector functions $\boldsymbol{f}(\boldsymbol{x})$ and $\boldsymbol{g}(\boldsymbol{x})$ over S is defined as

$$\left(\boldsymbol{f}, \boldsymbol{g}\right)_S \coloneqq \int_S \boldsymbol{f}^\intercal \boldsymbol{g} dS. \tag{2.9}$$

$\tilde{\Omega}$ on the stabilization terms indicates elemental integration. Note that the terms corresponding to the Dirichlet boundary conditions are not included in (2.8) as $\boldsymbol{u}_i^h = \boldsymbol{g}_i$ and $\boldsymbol{w}_i^h = \boldsymbol{0}$ on Γ_g are directly built into the solution and trial functions spaces, respectively.

The stabilization parameter $\boldsymbol{\tau}$ in (2.8), which plays a vital role in the performance of the stabilization method, is defined such that in the steady limit when $\omega = 0$, the equations recover the traditional GLS stabilization parameter as in the conventional finite element formulations [80, 156]. Since the convective matrix, $\boldsymbol{U}_j$, is diagonal, $\boldsymbol{\tau}$ becomes a diagonal matrix, $\boldsymbol{\tau} = \mathrm{diag}\,(\emptyset_0, \emptyset_1, \ldots, \emptyset_{(\mathrm{N}-1)})$, which entries can be calculated pointwise for each time point as

$$\tau_n = \left(u_{ni}^h \cdot \boldsymbol{\xi} u_{ni}^h + C_\mathrm{I} \nu^2 \boldsymbol{\xi} : \boldsymbol{\xi}\right)^{-\frac{1}{2}}, n \in [0, N) \tag{2.10}$$

where ν is the kinematic viscosity, $\boldsymbol{\xi}$ is the covariant tensor obtained from the mapping of the physical-parent elements, and C_I is a shape-function-dependent constant, which is 3 in our study.

Remarks:

1. The least-square stabilization terms encapsulate two traditional stabilization terms, the streamline upwind Petrov/Galerkin (SUPG) term $\rho \boldsymbol{U}_j \frac{\partial \boldsymbol{w}_i^h}{\partial x_j} \boldsymbol{\tau} \boldsymbol{U}_k \frac{\partial \boldsymbol{u}_i^h}{\partial x_k}$, and the pressure stabilized Petrov/Galerkin (PSPG) term $\frac{1}{\rho} \frac{\partial \boldsymbol{q}^h}{\partial x_i} \boldsymbol{\tau} \frac{\partial \boldsymbol{p}^h}{\partial x_i}$. However, only including the SUPG/PSPG stabilization will result in solution instabilities. The inclusion of the full differential operator $\mathscr{L}$, which includes the $\boldsymbol{H}$ terms, is crucial to the stability of this method. This is in contrast to the stabilization for the traditional time-stepping solvers, where the acceleration contribution in $\mathscr{L}$ is commonly ignored.

2. Expanding out the least-square stabilization terms will show that this stabilization method resembles the residual-based variational multiscale method (RBVMS) [11, 2, 15], if the subscale velocity $\boldsymbol{u}_i'$ is included only on the time-coupling term and the velocity gradient in the convection term, i.e.

$$\left(\boldsymbol{w}_i^h, \rho \boldsymbol{H}\left(\boldsymbol{u}_i^h + \boldsymbol{u}_i'\right) + \rho \boldsymbol{U}_j \frac{\partial \left(\boldsymbol{u}_i^h + \boldsymbol{u}_i'\right)}{\partial x_j}\right)_\Omega.$$

   Note that the diffusive term is dropped from $\mathscr{L}$ because we use linear interpolation functions. We tested including the full RBVMS terms, identical to the stabilization method in [11]. We observed that the RBVMS formulation is less stable than GLS, especially near the regime of transition flows, but the solution convergence rate using RBVMS is slightly faster than that of GLS.

3. The GLS method yields accurate results when the flow Wombersly number is small, which is valid for cardiovascular applications where the cardiac cycle oscillation frequency is small and mesh resolution is high. We have previously proposed a specialized stabilization method that yields superior accuracy [44].

4. The conventional design of the stabilization parameter $\boldsymbol{\tau}$ for unsteady problems also includes a time-discretization or frequency term proportional to Δt or $1/\omega$, respectively [88], which account for the acceleration term in the momentum equation. We

do not observe a difference in convergence or final solution in our cases with the inclusion of such a term. This is due to the low element Womersley numbers for cardiovascular simulations, defined as $\beta := h\sqrt{\frac{(N-1)\omega}{2\nu}}$. For $\beta < 1$, the frequency term's contribution to τ becomes negligible. In all the cases presented in this study, $\beta < 0.2$. Therefore, we do not include a frequency term in $\boldsymbol{\tau}$.

2.2.3 Solution Procedure

This section provide an overview of the solution procedure used for solving (2.8). We assume all interpolation functions are linear in the following derivations, which align with what is commonly used in finite element solvers specialized for cardiovascular flow. Therefore, we drop the terms that include second derivatives that cannot be transformed to only first derivatives through integration by parts. The unknowns at all time points are solves simultaneously resulting in $4N$ unknowns on each interior node. The Newton-Raphson method is used to account for iterative root-finding. Matrix splitting is used on the tangent matrix to enable the use of fast Fourier transforms when performing matrix-vector multiplications. A pseudo time-stepping scheme was developed in our previous study and used here to improve the convergence of the solver [46].

The test functions $\boldsymbol{w}_i^h$ and $\boldsymbol{q}^h$ in (2.8) are discretized in space using

$$\boldsymbol{w}_i^h(\boldsymbol{x}) = \sum_A \boldsymbol{c}_{Ai}^{\mathrm{w}} N_A(\boldsymbol{x}),$$
$$\boldsymbol{q}^h(\boldsymbol{x}) = \sum_A \boldsymbol{c}_A^{\mathrm{q}} N_A(\boldsymbol{x}),$$

where $N_A(\boldsymbol{x})$ is the interpolation function associated with node A. Since $\boldsymbol{w}_i^h$ and $\boldsymbol{q}^h$ are arbitrary functions, (2.8) must hold for any $\boldsymbol{c}_{Ai}^{\mathrm{w}}$ and $\boldsymbol{c}_A^{\mathrm{q}}$ arbitrary vectors. That permits us

to obtain a system of equations from (2.8), which are

$$\begin{aligned}
\boldsymbol{r}^{\mathrm{m}}_{Ai} &= \int_{\Omega}\left(\rho N_A \boldsymbol{H}\boldsymbol{u}^h_i + \rho N_A \boldsymbol{U}_j \frac{\partial \boldsymbol{u}^h_i}{\partial x_j} - \frac{\partial N_A}{\partial x_i}\boldsymbol{p}^h + \mu \frac{\partial N_A}{\partial x_j}\frac{\partial \boldsymbol{u}^h_i}{\partial x_j}\right) d\Omega - \int_{\Gamma_{\mathrm{h}}} N_A \boldsymbol{h} n_i d\Gamma \\
&\quad + \int_{\tilde{\Omega}}\left(-\boldsymbol{H}N_A + \boldsymbol{U}_j \frac{\partial N_A}{\partial x_j}\right)\boldsymbol{\tau}\mathscr{L}_i(\boldsymbol{u}^h_i, \boldsymbol{p}^h) d\Omega = \boldsymbol{0}, \qquad A \in \eta - \eta_g,\ i = 1, 2, \text{ and } 3, \qquad (2.11) \\
\boldsymbol{r}^{\mathrm{c}}_A &= \int_{\Omega} N_A \frac{\partial \boldsymbol{u}^h_i}{\partial x_i} d\Omega + \int_{\tilde{\Omega}} \frac{1}{\rho}\frac{\partial N_A}{\partial x_i}\boldsymbol{\tau}\mathscr{L}_i(\boldsymbol{u}^h_i, \boldsymbol{p}^h) d\Omega = \boldsymbol{0}, \qquad A \in \eta.
\end{aligned}$$

In (2.11), η and η_g denote the set of nodes in the entire domain Ω and those located on the Dirichlet boundaries Γ_{g}, respectively. Note that the negative sign in front of the $\boldsymbol{H}N_A$ in the least-square term results from performing transpose on the first momentum differential operator where $\boldsymbol{H}^{\intercal} = -\boldsymbol{H}$ and $\boldsymbol{U}_j^{\intercal} = \boldsymbol{U}_j$ because $\boldsymbol{H}$ is a skew-symmetric matrix and $\boldsymbol{U}_j$ is a diagonal matrix.

The velocity and pressure are discretized using the same interpolation functions as those of the test functions. Namely

$$\begin{aligned}
\boldsymbol{u}^h_i(\boldsymbol{x}) &= \sum_A \boldsymbol{u}^{\mathrm{d}}_{Ai} N_A(\boldsymbol{x}), \\
\boldsymbol{p}^h(\boldsymbol{x}) &= \sum_A \boldsymbol{p}^{\mathrm{d}}_A N_A(\boldsymbol{x}),
\end{aligned}$$

where $\boldsymbol{u}^{\mathrm{d}}_{Ai}$ and $\boldsymbol{p}^{\mathrm{d}}_A$ contain velocity and pressure, respectively, at all time points at node A. In our implementation, we build the Dirichlet boundary condition into the unknown vector so that $\boldsymbol{u}^{\mathrm{d}}_{Ai} = \boldsymbol{g}_i(\boldsymbol{x}_A)$, where $\boldsymbol{x}_A$ is the position of node A.

At the discrete level, our goal is to find $\boldsymbol{u}^{\mathrm{d}}_{Ai}$ and $\boldsymbol{p}^{\mathrm{d}}_A$ such that all equations in (2.11) are satisfied. Given that these equations are nonlinear, this feat is accomplished in an iterative process using the Newton-Raphson iterations, given as solving

$$\boldsymbol{y}^{(n+1)} = \boldsymbol{y}^{(n)} - \left(\boldsymbol{L}^{(n)}\right)^{-1} \boldsymbol{r}^{(n)} \qquad (2.12)$$

at each Newton-Raphson iteration n to update the solution from the last iteration $\boldsymbol{y}^{(n)}$ and compute it at the next iteration $\boldsymbol{y}^{(n+1)}$. $\boldsymbol{r}^{(n)}$ is the residual vector calculated based on the unknowns at the last iteration n using (2.11) and $\boldsymbol{L}^{(n)}$ is the tangent matrix calculated from

$\boldsymbol{y}^{(n)}$ due to the problem nonlinearity. The unknowns and equations are written in vectors as

$$\boldsymbol{y} \coloneqq \begin{bmatrix} \boldsymbol{u}_1^{\mathrm{d}} \\ \boldsymbol{u}_2^{\mathrm{d}} \\ \boldsymbol{u}_3^{\mathrm{d}} \\ \boldsymbol{p}^{\mathrm{d}} \end{bmatrix}, \quad \boldsymbol{r} \coloneqq \begin{bmatrix} \boldsymbol{r}_1^{\mathrm{m}} \\ \boldsymbol{r}_2^{\mathrm{m}} \\ \boldsymbol{r}_3^{\mathrm{m}} \\ \boldsymbol{r}^{\mathrm{c}} \end{bmatrix},$$

Before providing the form of the tangent matrix, it is evident that all terms that do not contain $\boldsymbol{H}$ in (2.11) can be calculated pointwise. In another word, the residual at each time point can be calculated using strictly the unknowns associated with such time point if the terms involving the time-coupling acceleration matrix $\boldsymbol{H}$ can be calculated separately. Using this knowledge, we perform matrix splitting on the tangent matrix $\boldsymbol{L}^{(n)}$ to separate time-coupling terms from the non-coupled terms as

$$\boldsymbol{L} = \frac{\partial \boldsymbol{r}}{\partial \boldsymbol{y}} = \boldsymbol{C} + \boldsymbol{P}, \tag{2.13}$$

where the superscript (n) is dropped to simplify the notation. The non-coupled pointwise tangent matrix $\boldsymbol{P}$ is identical to that of the form in a conventional steady-state finite element Navier-Stokes solver as,

$$\boldsymbol{P} = \begin{bmatrix} \boldsymbol{K} & \boldsymbol{0} & \boldsymbol{0} & \boldsymbol{G}_1 \\ \boldsymbol{0} & \boldsymbol{K} & \boldsymbol{0} & \boldsymbol{G}_2 \\ \boldsymbol{0} & \boldsymbol{0} & \boldsymbol{K} & \boldsymbol{G}_3 \\ \boldsymbol{D}_1 & \boldsymbol{D}_2 & \boldsymbol{D}_3 & \boldsymbol{L} \end{bmatrix}, \tag{2.14}$$

where

$$\begin{aligned}
\boldsymbol{K}_{AB} &= \int_{\Omega} \left(\rho N_A \boldsymbol{U}_k \frac{\partial N_B}{\partial x_k} + \mu \frac{\partial N_A}{\partial x_k} \frac{\partial N_B}{\partial x_k} \boldsymbol{I} \right) d\Omega + \int_{\tilde{\Omega}} \boldsymbol{U}_k \frac{\partial N_A}{\partial x_k} \rho \boldsymbol{\tau} \boldsymbol{U}_k \frac{\partial N_B}{\partial x_k} d\Omega, \\
(\boldsymbol{G}_{AB})_i &= -\int_{\Omega} \frac{\partial N_A}{\partial x_i} N_B \boldsymbol{I} d\Omega + \int_{\tilde{\Omega}} \boldsymbol{U}_k \frac{\partial N_A}{\partial x_k} \boldsymbol{\tau} \frac{\partial N_B}{\partial x_i} d\Omega, \\
(\boldsymbol{D}_{AB})_j &= \int_{\Omega} N_A \frac{\partial N_B}{\partial x_j} \boldsymbol{I} d\Omega + \int_{\tilde{\Omega}} \frac{\partial N_A}{\partial x_j} \boldsymbol{\tau} \boldsymbol{U}_k \frac{\partial N_B}{\partial x_k} d\Omega, \\
\boldsymbol{L}_{AB} &= \int_{\tilde{\Omega}} \frac{1}{\rho} \frac{\partial N_A}{\partial x_k} \boldsymbol{\tau} \frac{\partial N_B}{\partial x_k} d\Omega.
\end{aligned} \tag{2.15}$$

Note that all matrix blocks in $\boldsymbol{P}$ are diagonal matrices. Therefore, the computational cost associated with matrix multiplications of $\boldsymbol{P}$ is $O(N)$ with a correct sparse matrix implementation.

The time point-coupling tangent matrix $\boldsymbol{C}$, which handles all terms that include the $\boldsymbol{H}$ matrix, takes one contribution from the Galerkin's terms and four contributions from the least-square stabilization terms in (2.7). Our numerical experiments showed that keeping only the Galerkin's term's contribution in $\boldsymbol{C}$ has a negligible effect on the solution convergence. Therefore, the tangent contributions from the stabilization terms are neglected, simplifying the number of operations required to perform operations using $\boldsymbol{C}$. Note that this simplification happens only to the calculation of the tangent matrix but not to the residual vector, so it does not have an effect on the final solution. The simplified time-coupling tangent matrix has the form

$$\boldsymbol{C} = \begin{bmatrix} \boldsymbol{F} & \boldsymbol{0} & \boldsymbol{0} & \boldsymbol{0} \\ \boldsymbol{0} & \boldsymbol{F} & \boldsymbol{0} & \boldsymbol{0} \\ \boldsymbol{0} & \boldsymbol{0} & \boldsymbol{F} & \boldsymbol{0} \\ \boldsymbol{0} & \boldsymbol{0} & \boldsymbol{0} & \boldsymbol{0} \end{bmatrix}, \tag{2.16}$$

where

$$\boldsymbol{F}_{AB} = \boldsymbol{H} \int_{\Omega} \rho N_A \boldsymbol{I} N_B d\Omega, \tag{2.17}$$

Since $\boldsymbol{H}$ is defined as $\boldsymbol{H} = \boldsymbol{E}^{-1}\boldsymbol{\Omega}\boldsymbol{E}$. Matrix multiplications involving $\boldsymbol{E}$ and $\boldsymbol{E}^{-1}$ can be replaced by a fast Fourier transform and a inverse fast Fourier transform scheme, respectively. This way, the cost scaling for performing the matrix-vector multiplication involving $\boldsymbol{H}$ is reduced from $O(N^2)$ to $O(Nlog(N))$, which can be approximated as $O(N)$ if the range of N is small. This study used the open-source library FFTW [65] to perform the fast Fourier transforms.

Before solving the final linear system, a pseudo time stepping scheme is added to improve linear solver convergence and reduce the cost. Pseudo time-stepping schemes

have been used previously in solving harmonic balance equations [71] and the specific method used here was proposed in our previous study [46]. The implementation of the pseudo time-stepping involves adding

$$\left(\boldsymbol{w}_i^h, \rho \frac{\partial \boldsymbol{u}_i^h}{\partial \tilde{t}}\right)_\Omega, \tag{2.18}$$

to (2.8), and integrating $\boldsymbol{u}_i^h$ in pseudo-time $\tilde{t}$ similar to the conventional time formulation of the Navier-Stokes equation. Choosing to use the generalized-α method [84], the tangent matrix is supplemented by adding

$$\left(N_A, \frac{c_1 \rho}{\Delta \tilde{t}} N_B \boldsymbol{I}\right)_\Omega,$$

to $\boldsymbol{K}_{AB}$ in (2.15), where we used $\rho_\infty = 0$ resulting in $c_1 = 1.5$. Note that the added pseudo time step term will go to zero as the solution converges to a steady result. Therefore, it improves the convergence behavior without affecting the final solution. The choice of the pseudo time step size $\Delta \tilde{t}$ is essential for achieving convergence and optimizing convergence speed. Our numerical experiments show that the system of equations will generally converge when the convective Courant–Friedrichs–Lewy (CFL) number calculated from the pseudo time step size is $O(1)$ or less, defined as

$$C_{\text{CFL}} = \frac{u_c \Delta \tilde{t}}{h_c},$$

where the characteristic length, h_c, is taken as the mean element edge length of the domain and the characteristic convective velocity, u_c, is taken as the mean velocity at the inlet boundary for the maximum flow rate in the inlet flow profile. Therefore, the optimal choice of pseudo time step size can be approximated as

$$\Delta \tilde{t} \sim \frac{h_c}{u_c}.$$

To illustrate the impact of the CFL number on convergence, we conducted four identical simulations, varying only the pseudo time step size. The simulation case is the same as

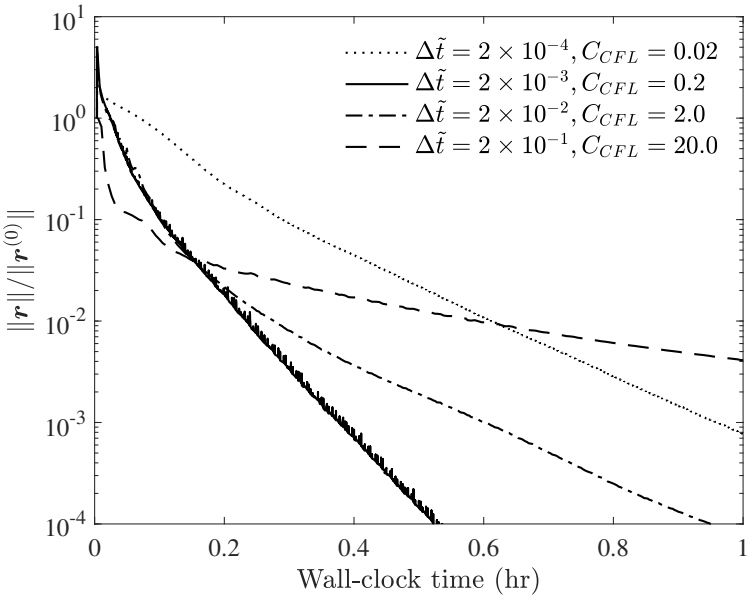

Figure 2.1: Simulation convergence speed for four pseudo time step sizes, $\Delta\tilde{t}$. The y-axis is the relative residual compared to the residual at the initialization step, $\|\boldsymbol{r}\|/\|\boldsymbol{r}^{(0)}\|$.

the $N = 13$ case in Section 3.2. As depicted in Figure 2.1, the simulation with a large CFL number converges extremely slowly. On the other hand, excessively small CFL number also leads to increased simulation costs due to the cost for constructing the linear system at each pseudo time step. It's important to note that the specific CFL number and the optimal pseudo time step size for achieving the fastest convergence can vary based on other factors such as the geometry of the case, mesh uniformity, and flow dynamics. In general, optimal convergence is attained when the CFL number is around 1.

A backflow stabilization scheme is used to prevent instabilities in the presence of reversal flow through Γ_h where a Neumann boundary condition is imposed. The method is identical to the backflow stabilization scheme used for a conventional time-stepping Navier-Stokes finite element solver [43] by adding

$$\left(\boldsymbol{w}_i^h, \frac{\rho}{2}\beta|\boldsymbol{U}_i n_i|_- \boldsymbol{u}_i^h\right)_{\Gamma_h},$$

to the right-hand side of (2.8), where

$$|\boldsymbol{U}_i n_i|_- = \frac{\boldsymbol{U}_i n_i - |\boldsymbol{U}_i n_i|}{2},$$

and $\beta \in [0, 1]$ is a user-defined coefficient, which we used $\beta = 0.2$ in all cases.

Lastly, we used a standard Jacobi preconditioner on the tangent matrix $\boldsymbol{L}$ to improve the conditioning of the linear system [49]. Since $\boldsymbol{C}$ is a zero diagonal matrix, the preconditioner is taken as the diagonal entries of matrix $\boldsymbol{P}$. We used the generalized minimal residual method (GMRES) to iteratively solve the linear system in (2.12) [149]. Simulations are considered converged after the second norm of the residual drops by three orders of magnitudes, which was established in our precious study [46].

2.3 Results

The proposed harmonic balance solver is constructed from our in-house finite-element solver named Multi-physics finite-element solver (MUPFES) [127, 50]. The solver has been verified [165] and extensively employed for cardiovascular modeling in the past [52, 51, 90]. This solver is parallelized using a message passing interface (MPI) and a specialized parallelization strategy [48, 47]. The workload is parallelized using spatial partitioning by employing ParMETIS library [95]. All computations are performed on a cluster of AMD Opteron^{TM} 6378 processors that are interconnected via a QDR Infiniband.

In the results section, our primary focus is to compare the accuracy and cost of the proposed harmonic balance CFD solver with the conventional time-stepping CFD solver. For consistency with the harmonic balance solver, the time-stepping CFD solver also uses the GLS stabilization method. Unlike the proposed solver, The stabilization parameter for the time solver, $\hat{\tau}$, includes contribution from the acceleration term since the time step sizes used are significantly small. The exact form was introduced in a prior paper as [88]

$$\hat{\tau} = \left(\hat{\omega}^2 + \hat{u}_i^h \cdot \boldsymbol{\xi} \hat{u}_i^h + C_I \nu^2 \boldsymbol{\xi} : \boldsymbol{\xi}\right)^{-\frac{1}{2}}, \tag{2.19}$$

where $\hat{\omega} = \|\frac{\partial \hat{u}_i^h}{\partial t}\|_\Omega / \|\hat{u}_i^h\|_\Omega$. To keep the time and harmonic balance solver comparison as

close as possible, the linear solver tolerance is set at 0.03 for both solvers. The time solver Newton-Ralphson iteration tolerance is set at three order of magnitudes, consistent with the convergence criteria of the harmonic balance solver.

We conducted simulations on three cardiovascular cases using both solvers: a Glenn procedure pulmonary arteries case, a cerebral arteries case, and a left main coronary arteries case. These cases were selected to encompass a wide range of scenarios, distinguished both numerically and fluid-dynamically. The geometries and inlet flow rate boundary conditions of these cases were obtained from an online repository [194]. The Reynolds number for the Glenn case is higher than the other two cases, featuring a smooth inflow profile, accurately captured with a few time points. The cerebral arteries case involves a more complex smooth inflow profile with higher geometric complexity, while the left main coronary artery case has distinct kinks in the flow profile, which will require significantly more Fourier modes to fully represent the curve.

The outlets are all proscribed as Neumann boundaries with steady physiological pressure values. Previous cardiovascular simulations have proscribed the outlet as resistance condition using a resistor, an indicator, and a capacitor for more realistic outlet responses [52, 180]. However, the implementation of the resistance boundary in the proposed harmonic balance solver is not within the scope of this study. All walls were assumed to be non-moving and non-slip. The whole blood density ($\rho = 1.06$ g/cm^3) and dynamic viscosity ($\mu = 4$ mPa $\cdot$ s) were consistent across all cases. The primary aim of these results is to establish the solution validity and cost efficiency of the harmonic balance solver as an alternative to the conventional time solver. Since the geometries and boundary conditions for all cases are physiological, we will also briefly discuss the clinical relevance of each case.

2.3.1 Glenn pulmonary flow

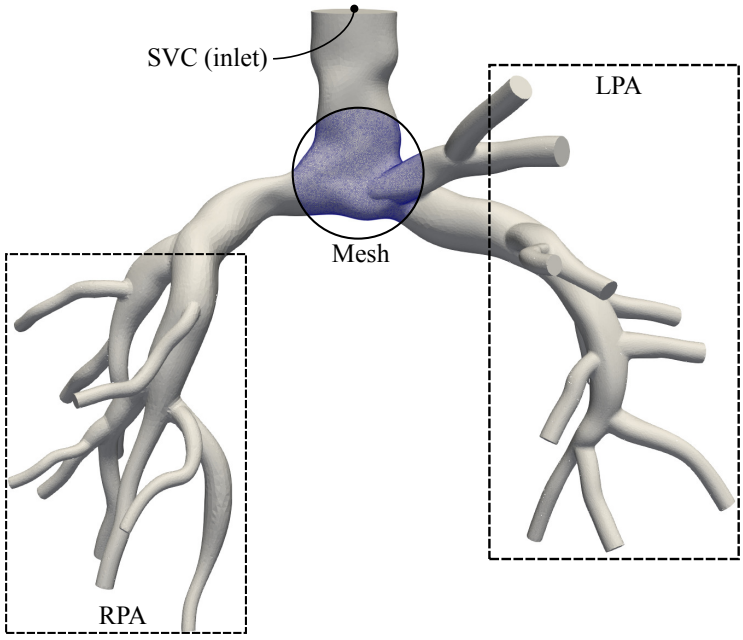

Figure 2.2: Clinically obtained Glenn pulmonary geometry with a sectional view of the mesh resolution. SVC, superior vena cava; LPA, left pulmonary artery; RPA, right pulmonary artery.

The Glenn procedure is used as an early-stage surgical intervention for patients with single ventricle birth defects [107, 143]. The operation surgically establishes the pulmonary circulation by directly connecting the superior vena cava (SVC) to the pulmonary arteries (PA), as shown in the geometry in Figure 2.2. Prior studies have used this geometry to perform conventional CFD simulations [180]. The inflow boundary condition is taken from the prior study, which gives the SVC flow rate as a function of time in a cardiac cycle. The outlet boundaries are set at a steady of 7.5 mmHg. The cardiac cycle period is 0.6979 seconds, and the peak Reynolds number is around $1,000$.

In this study, four simulations are performed: one using the conventional time-stepping CFD solver and run for 4 cardiac cycles or $4,000$ time steps, and three using the harmonics balance solver with different numbers of time points, $N = 7$, 13, and 19. The geometry used is discretized with $1,946,676$ tetrahedral elements. For the harmonic

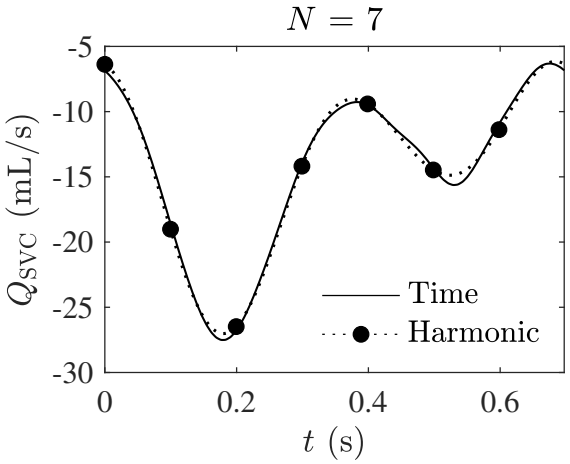

Figure 2.3: Discretized harmonics balance boundary conditions at each time point (black circle) on the SVC inlet. The dotted line represents the reconstructed profile from the time points. For reference, the solid line is the original flow profile in time. $N = 7$.

balance simulations, the pseudo time step size is $\Delta\tilde{t} = 5 \times 10^{-3}$ resulting in $C_{\mathrm{CFL}} = 2.5$. The inlet boundary conditions for the harmonic balance simulations are generated by performing a Fourier transform on the inflow profile and then performing a discrete inverse Fourier transform on the truncated frequency series, as defined in Equations (2.2) and (2.5). The resulting inlet boundary conditions are given in Figure 2.3 to 2.5. As shown by the boundary condition plots, this inlet profile for this case is smooth and can be captured with a few time points. In fact, the truncation error for the inflow profile is already less than 1% for $N = 13$.

All simulations are performed on our in-house cluster using 288 cores at 2.4 GHz clock speed. The cost of performing the harmonic balance simulations is shown in Figure 2.6, with the left axis showing the wall-clock time of the simulations and the right axis showing the speedup compared to the conventional time-stepping solver, which simulation took 50 wall-clock hours to run. The figure is drawn on a log-log scale to demonstrate the cost scaling of our solver as the number of time points increases. The harmonics balance simulation using $N = 3$ was only performed to help demonstrate the cost scaling. Even for the harmonics balance case with $N = 19$, the solution speed is still 40 times faster than

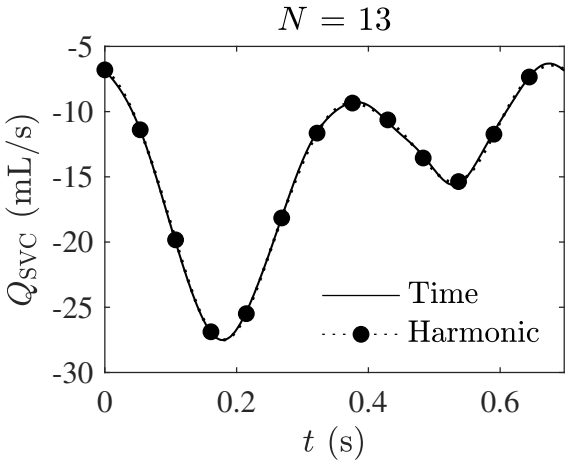

Figure 2.4: Discretized harmonics balance boundary conditions at each time point (black circle) on the SVC inlet. The dotted line represents the reconstructed profile from the time points. For reference, the solid line is the original flow profile in time. $N = 13$.

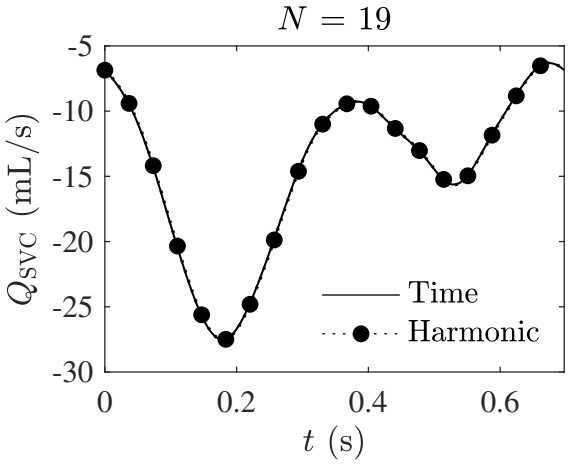

Figure 2.5: Discretized harmonics balance boundary conditions at each time point (black circle) on the SVC inlet. The dotted line represents the reconstructed profile from the time points. For reference, the solid line is the original flow profile in time. $N = 19$.

the conventional solver.

Using the solution obtained at the time points of the harmonics balance solver, we can reconstruct the flow field at any time by performing a Fourier transform on the time point results to obtain the spectral results and reconstruct the solution at any time in the cycle. Figure 2.7 and 2.8 shows the velocity and pressure field results at $t = 0.2$ of the cardiac cycle, where the inlet flow rate is at its peak. Qualitative differences are only noticeable for the $N = 7$ case at specific locations in the domain, such as the SVC-PA junction.

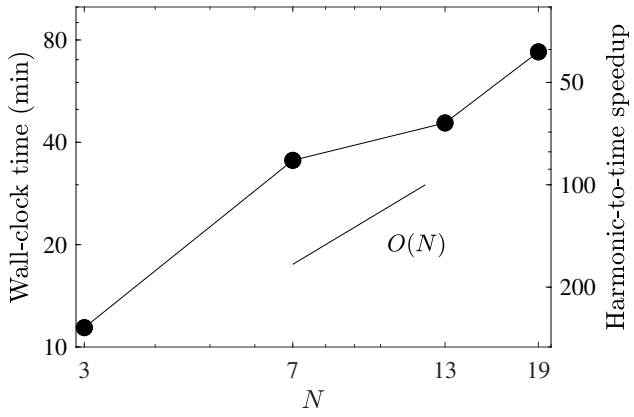

Figure 2.6: The cost performance of the harmonic balance solver for the pulmonary flow case. The left axis shows the wall-clock time of the harmonic balance simulations. The right axis shows the speedup of the harmonic balance simulations compared to the conventional time-stepping simulation.

Besides qualitatively examining the velocity and pressure field, we want to establish a quantitative way to measure the accuracy of the harmonics balance solver's results. We introduce a notation for the integrated relative root mean squared error, $E_X^{f(x)}$, to understand the difference between the conventional time solver results and the proposed harmonic balance solver results. The error is defined as

$$E_X^{f(x)} = \frac{\int_X \| f_{\text{harmonic}}(x) - f_{\text{time}}(x) \| dx}{\int_X \| f_{\text{time}}(x) \| dx}, \tag{2.20}$$

where the dependent variable $f(x)$ can be the velocity vector, $\boldsymbol{u}$, or the pressure, p, with subscripts denoting whether the results are taken from the harmonics balance solver or the conventional time solver. The integral can be performed over the geometry, Ω, the temporal cycle, T, or both.

Using this definition, we can calculate the spacial integral relative error for both the velocity and pressure and plot it over one solution cycle, shown in Figure 2.9 and 2.10. Note that the curve does not appear smooth since we stored the results from the conventional time solver every 50 time steps for processing, resulting in 20 data points for the error calculation.

We can further integrate the error in time over one cycle and show the error trend as

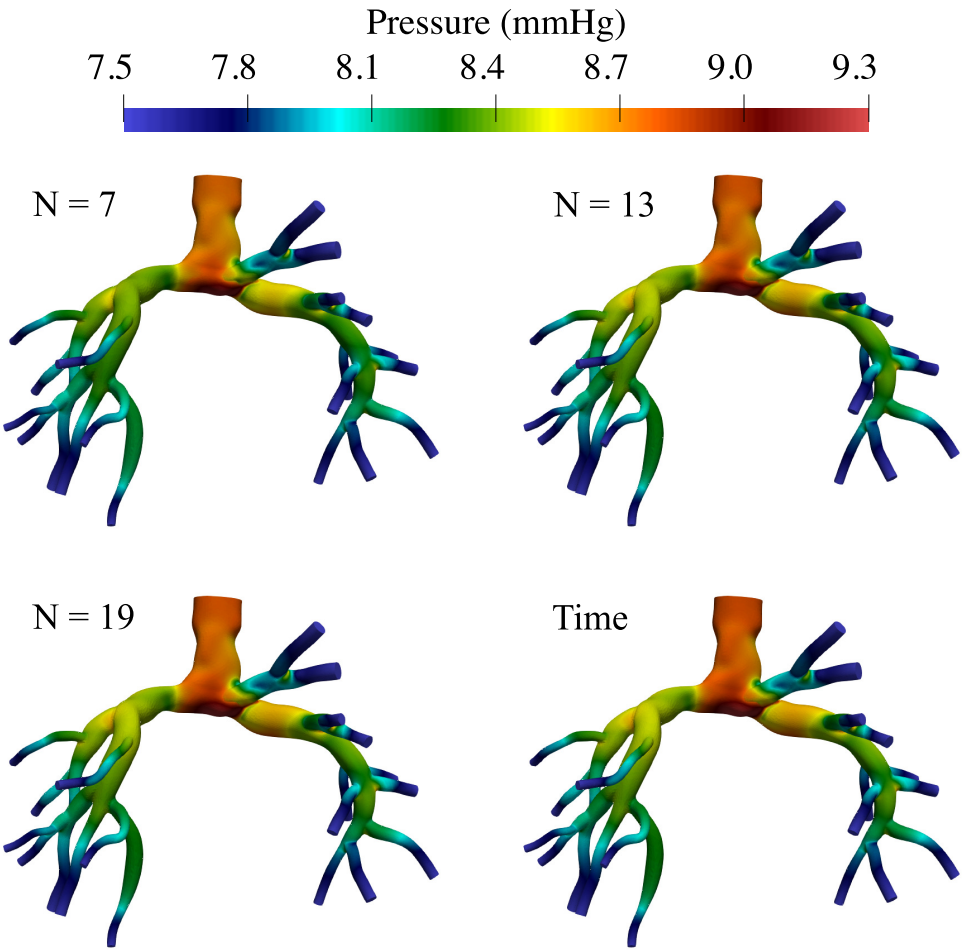

Figure 2.7: Harmonics balance results using $N = 7$, 13, and 19 compared to the conventional time results for the pulmonary flow case. The pressure contours are taken at $t = 0.2$ seconds of the cardiac cycle.

the harmonics resolution N increases. As shown in Figure 2.11, the error of the variables is integrated both over the fluid domain, Ω, and over one cardiac cycle, T. The pressure relative error is much smaller than the velocity error because the Neumann outlets of both the time and harmonic balance simulations are set at a fixed pressure value, which is much larger than the range of pressure in the solution field. We will discuss how this error might change if the outlet boundary type is different in the discussion section. The velocity error drops significantly as the number of time points increases, down to less than 5% when $N = 19$. Note that although the inlet flow profile can already be well represented with $N = 7$, due to the intermediate Reynolds number of this case (Re = 1000),

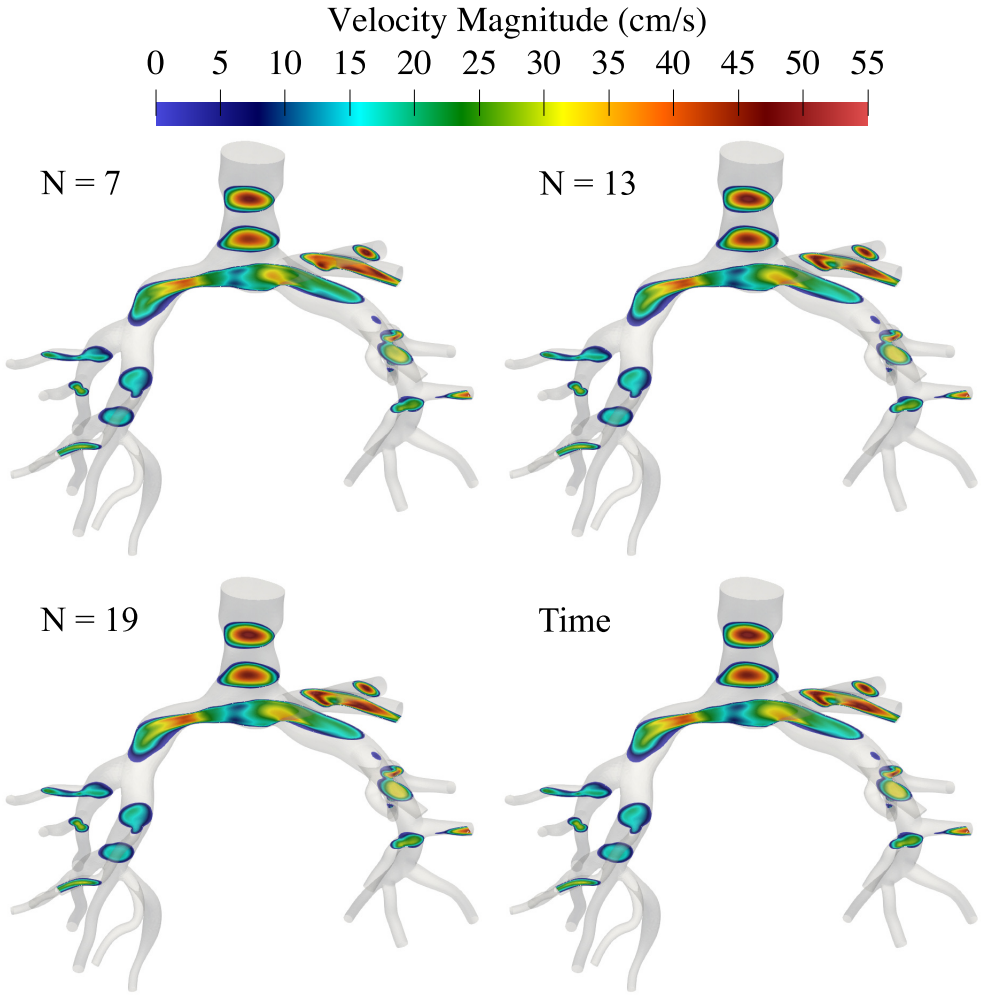

Figure 2.8: Harmonics balance results using $N = 7$, 13, and 19 compared to the conventional time results for the pulmonary flow case. The velocity magnitude contours are taken at $t = 0.2$ seconds of the cardiac cycle.

the solution requires higher than 7 harmonics resolution to fully capture the dynamics of the fluid field.

We want to emphasize that this relative error, $E_{\Omega,T}$, is calculated as the relative error at each node in the computational domain, then integrated over the solution space and the cardiac cycle. The error calculation's aggregate nature makes it an estimate of the upper limit of the relative numerical error of the entire solution field. In reality, the parameters of significance in a physiological sense are not individual nodal (or local) values but summarized values at specific locations, such as flow rates at the outlets. For example,

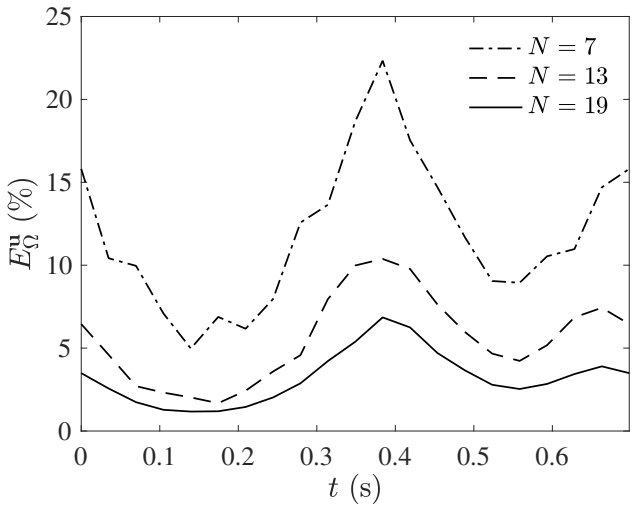

Figure 2.9: The volumetric integral relative root mean square error over the fluid domain for the velocity vector as functions of time in the cardiac cycle of the pulmonary flow.

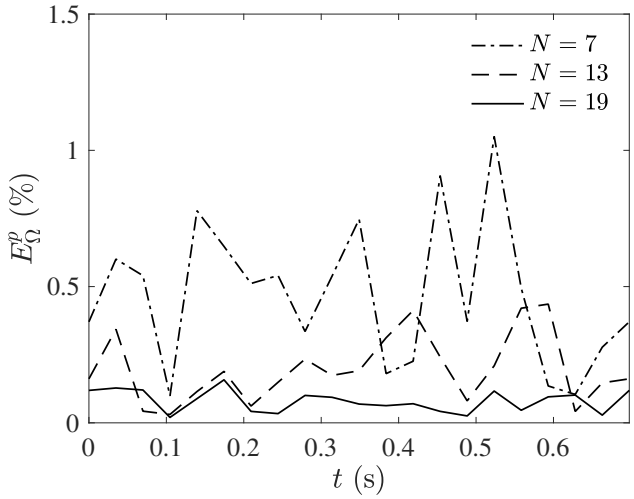

Figure 2.10: The volumetric integral relative root mean square error over the fluid domain for the pressure as functions of time in the cardiac cycle of the pulmonary flow.

the flow rate to each side of the pulmonary artery in the Glenn operation is essential for indicating potential asymmetry in future lung development [31, 116]. Figure 2.13 to 2.15 shows the flow rate over one cardiac cycle of the (LPA), Q_{LPA}, obtained by integrating the norm of the velocity at the LPA outlet surface. The flow profiles between the harmonics balance results and the conventional time results are similar, even for the simulation with only seven time points. We can calculate the relative error of the LPA flow rate results and overlay it with the inlet SVC flow rate truncation error in Figure 2.12. As demonstrated

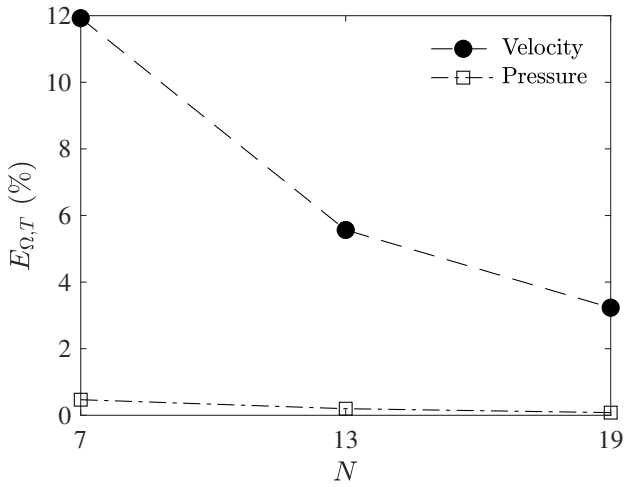

Figure 2.11: Pulmonary flow relative root mean square error for the velocity and pressure integrated over the fluid domain and one cardiac cycle.

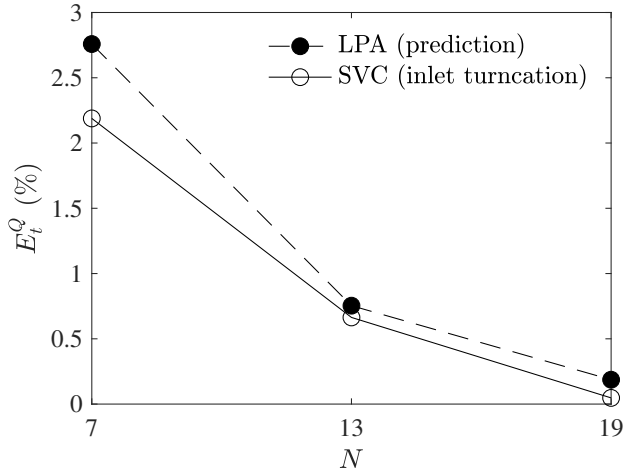

Figure 2.12: Pulmonary flow relative root mean square error for the inlet SVC flow rate (truncation) and the LPA outlet flow rate (prediction).

in this figure, the inlet discretization error is an excellent estimate of the solution error of the LPA flow rate, which is below 5% for $N = 7$ and well below 1% if the number of time points goes beyond $N = 13$.

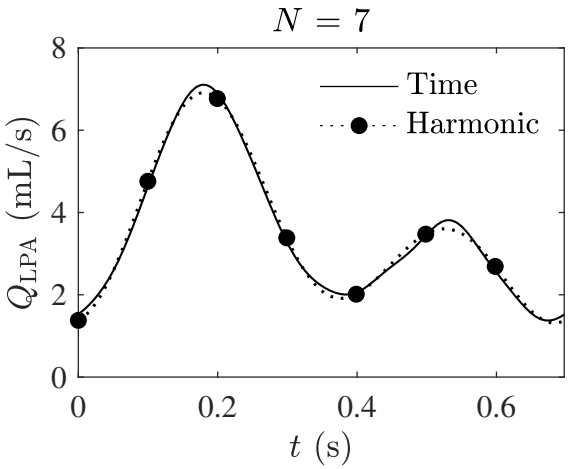

Figure 2.13: Left pulmonary artery (LPA) flow rate results obtained with the harmonics balance solver (solid circles) and the with the conventional time solver (solid line). The dotted line represents the reconstructed profile from the harmonics balance time points. $N = 7$.

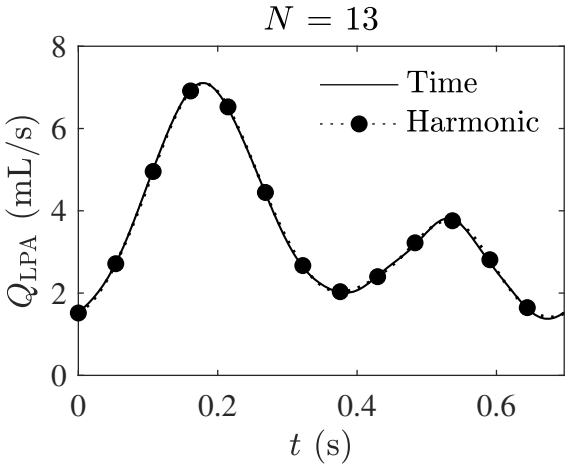

Figure 2.14: Left pulmonary artery (LPA) flow rate results obtained with the harmonics balance solver (solid circles) and the with the conventional time solver (solid line). The dotted line represents the reconstructed profile from the harmonics balance time points. $N = 13$.

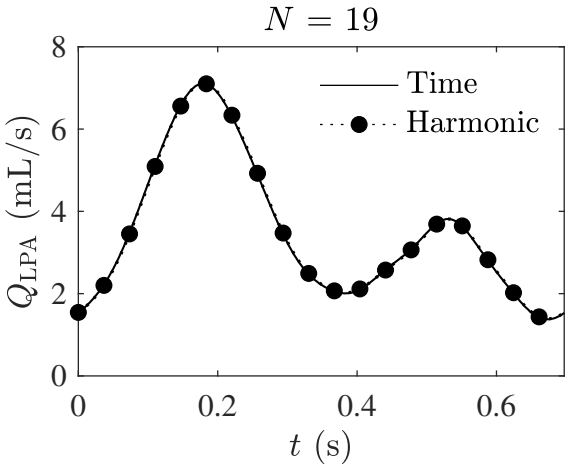

Figure 2.15: Left pulmonary artery (LPA) flow rate results obtained with the harmonics balance solver (solid circles) and the with the conventional time solver (solid line). The dotted line represents the reconstructed profile from the harmonics balance time points. $N = 19$.

2.3.2 Cerebral flow

The second case presented in the study involves the flow of cerebral arteries. The cerebral arteries provide about 20% of the blood to the brain. The geometry contains two vertebral arteries (VA) inlets that merge into the basilar artery, as shown in Figure 2.16. The specific geometry used in this study was used for performing conventional CFD simulations previously [20] to understand the mixing of flows from each side of the vertebral arteries. The inlet flow rate profile in time is taken identically to the prior study with a period of 1 second. The outlet pressure is set at 115 mmHg. The peak Reynolds number in this flow is around 120. The inflow function for cerebral flow is more complex than that of the pulmonary flow, requiring more time points to represent accurately.

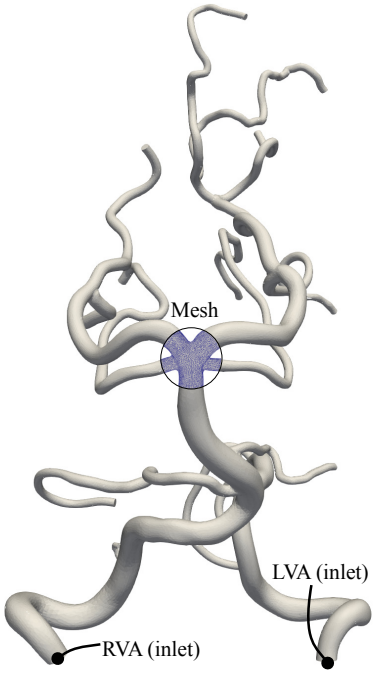

Figure 2.16: Clinically obtained cerebral arteries geometry used in this study with a sectional view of the mesh resolution. LVA, left vertebral artery; RVA, left vertebral artery.

Four simulations are performed, one using the conventional time solver and three using the harmonic balance solver, with different numbers of time points used: $N = 7$, 13, and 19. The harmonic balance boundary conditions are calculated and represented in Figure 2.17 to 2.19, prescribed identically at the LVA and the RVA inlet faces. The geometry is discretized using $734,863$ tetrahedral elements. The pseudo time step size is 2×10^{-2} resulting a CFL number of $C_{\mathrm{CFL}} = 2$.

Each simulation was run on 288 CPU cores at a 2.4 GHz clock rate. The simulation cost of the harmonics balance solver is shown in Figure 2.20. The conventional time simulation took 12 hours to run four cardiac cycles using 1000 time steps per cycle. The cases ran with $N = 3$ and 21 are only used for demonstrating the cost scaling. One thing to note is that the cost scaling becomes $O(N \log(N))$ as the number of time points, N, gets larger, which is as expected from using fast Fourier transforms in our solver.

The pressure and velocity contours for the highest number of time points simulated

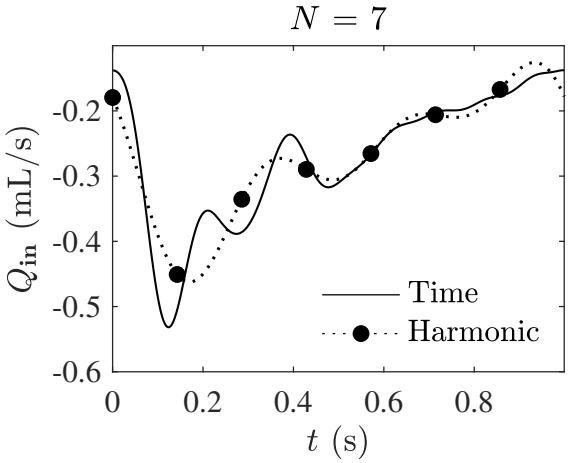

Figure 2.17: Discretized harmonics balance boundary conditions at each time point (black circle) on the LVA and RVA inlets. The dotted line represents the reconstructed profile from the time points. For reference, the solid line is the original flow profile in time. $N = 7$.

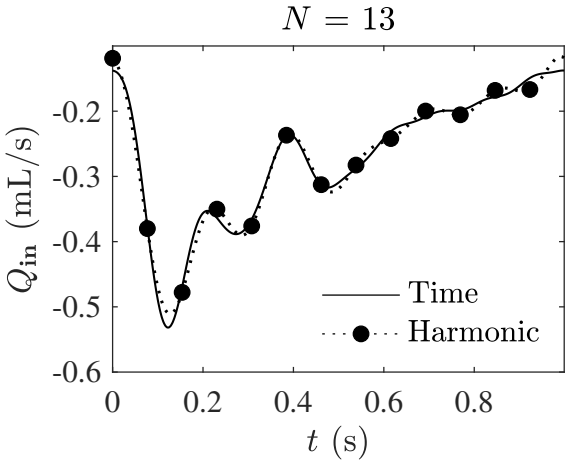

Figure 2.18: Discretized harmonics balance boundary conditions at each time point (black circle) on the LVA and RVA inlets. The dotted line represents the reconstructed profile from the time points. For reference, the solid line is the original flow profile in time. $N = 13$.

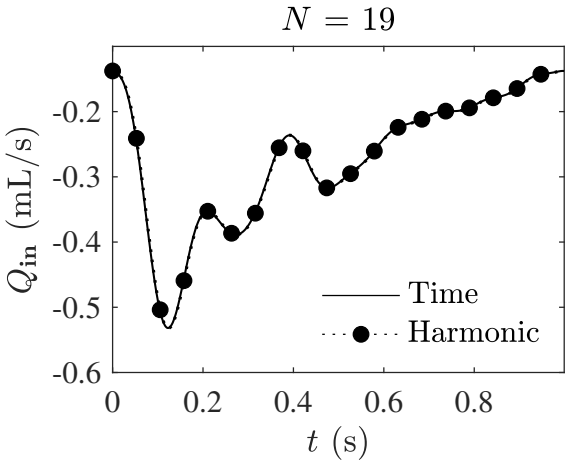

Figure 2.19: Discretized harmonics balance boundary conditions at each time point (black circle) on the LVA and RVA inlets. The dotted line represents the reconstructed profile from the time points. For reference, the solid line is the original flow profile in time. $N = 19$.

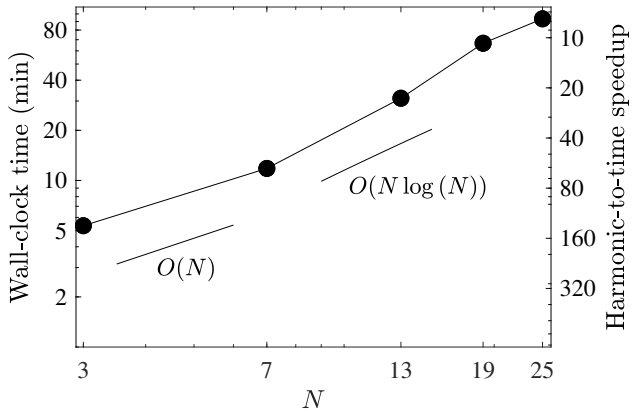

Figure 2.20: The cost performance of the harmonic balance solver for the cerebral flow case. The left axis shows the wall-clock time of the harmonic balance simulations. The right axis shows the speedup of the harmonic balance simulations compared to the conventional time-stepping simulation.

($N = 19$) at $t = 0.2$ in the cardiac cycle are shown in Figure 2.21. As shown in the figure, the results show no noticeable qualitative differences.

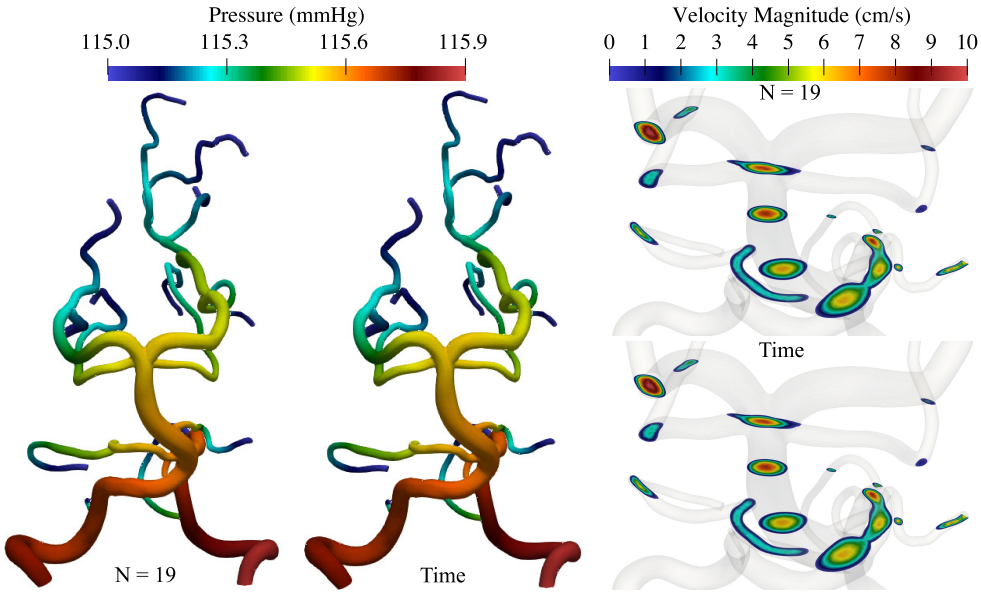

Figure 2.21: Harmonics balance results using $N = 19$ compared to the conventional time results for the pulmonary flow case. The pressure and velocity magnitude contours are taken at $t = 0.2$ seconds of the cardiac cycle.

Similar to the pulmonary flow case, the integral relative errors can be calculated. Figure 2.22 and 2.23 shows the spacial integrated relative error, where the solution error obtained using 19 time points is well under 10% at any point of the cardiac cycle. Figure 2.24 shows the spacial and time-integrated error of the solution along with the truncation error for the inlet boundary condition. The inlet flow rate truncation error is a good indication for the velocity field solution error for this case. The pressure error is significantly small due to the large steady pressure boundary conditions at the outlets.

Figure 2.24 includes one additional set of result points at $N = 25$. We can see that as the number of time points increases further past $N = 19$, the errors remain the same, indicating that the source of this difference between the results of the harmonic balance solver and the conventional time solver lies within the mathematical formulation itself rather than the temporal discretization of the harmonic balance solver. It is difficult to determine which formulation is closer to the physiological results without extensive clinical-to-simulation comparison studies, which are outside the scope of this study.

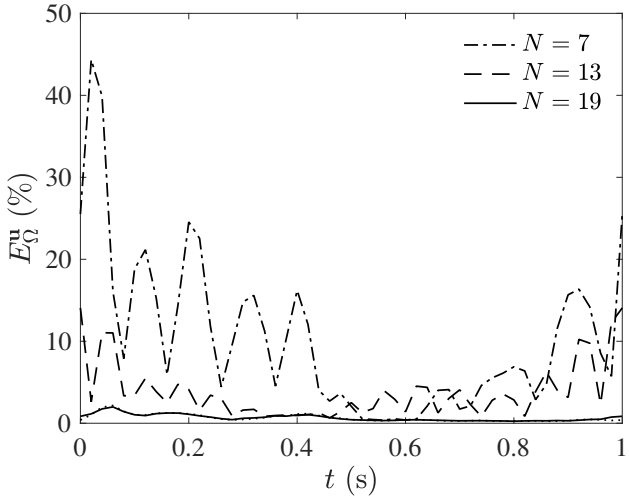

Figure 2.22: The volumetric integral relative root mean square error over the fluid domain for the velocity vector as functions of time in the cardiac cycle of the cerebral flow.

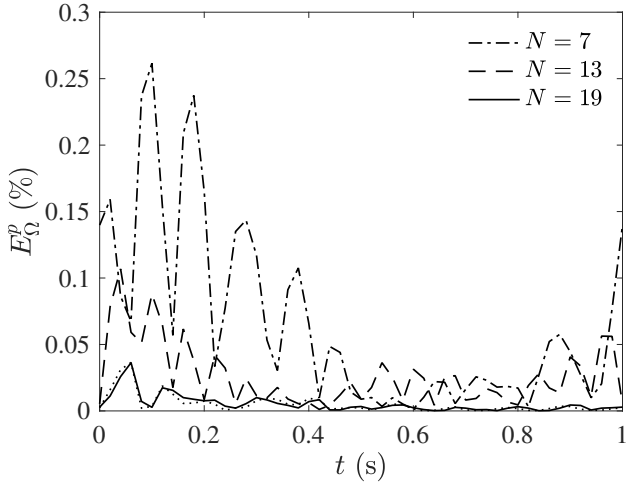

Figure 2.23: The volumetric integral relative root mean square error over the fluid domain for the pressure as functions of time in the cardiac cycle of the cerebral flow.

2.3.3 Left main coronary arteries flow

Coronary artery disease is the leading cause of death in the United States [158, 105]. This disease is most commonly caused by atherosclerosis of coronary arteries, which causes narrowing or blockage of the blood supply to the heart. In the final case of this study, we

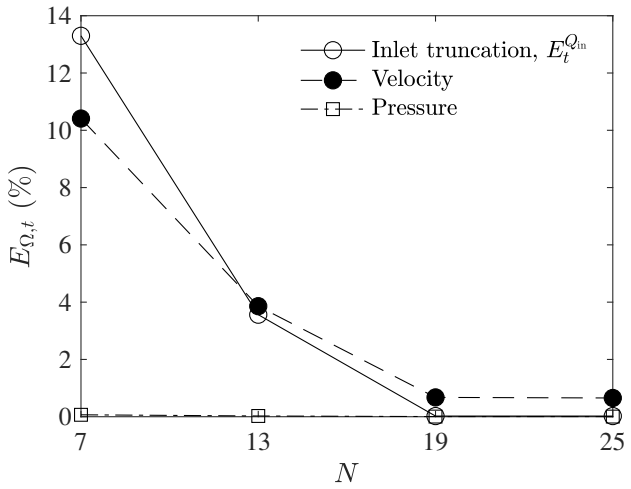

Figure 2.24: The volumetric and temporal integral relative root mean square error over the fluid domain and one cardiac cycle of the cerebral flow results.

will test our solver on the flow of the left main coronary arteries. The left main coronary arteries (LMCA) stem from the root of the ascending aorta and supply blood to the left side of the heart muscles, including the left ventricle. CFD simulations have been used as a noninvasive tool to gather the flow rate and pressure in patient-specific coronary geometries, which can inform the severity of coronary artery disease and help with surgical decision-making. The LMCA geometry used in this case was segmented from a clinically obtained image. The aorta and right coronary arteries are discarded from the original image, so only the LMCA remains, as shown in Figure 2.25. This decision results from the flow instabilities and backflow introduced by the aorta, which makes simulation convergence difficult for both the conventional CFD solver and the proposed harmonic balance solver. The clinically realistic inlet flow profile is taken from literature [17] and was used as the boundary condition for prior conventional CFD studies [135]. This inlet boundary condition is challenging numerically because the time flow profile has distinctive kinks which means requires significant number of time points to accurately represent the function in the harmonic balance solver. Nonetheless, we will show that the harmonic balance solver produces reasonable solutions using finite numbers of time points. The outlets are set at a steady pressure of 70 mmHg. The resulting peak Reynolds number of the domain

is around 100.

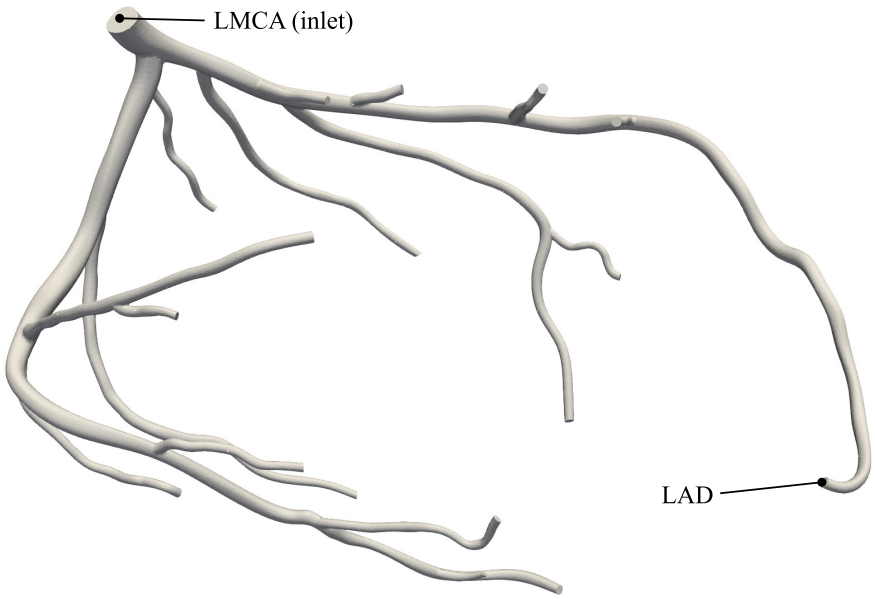

Figure 2.25: Clinically obtained left main coronary arteries (LMCA) geometry used in this study. The left anterior descending artery (LAD) is marked as the location for reporting results.

Six simulations are performed, one using the conventional time solver and three using the harmonics balance solver with $N = 1$, 7, 13, 19, and 25. In this case, we simulated a case with steady state boundaries ($N = 1$) to demonstrate that steady state flow assumption, which is commonly used for saving computational cost in clinical settings, is not appropriate to capture the full thermodynamics of the flow. The inlet boundary conditions $N = 13$, 19, and 25 are shown in Figure 2.26 to 2.28, with $T = 0.8$ seconds. Obviously, using 13 time points or lower, the sharp changes in the actual flow rate profile cannot be fully captured. As the number of time points increases, the general shapes of the profile get better captured. The computational domain is discretized using $1,336,207$ tetrahedral elements. The pseudo time step size is 5×10^{-3} resulting a CFL number of $C_{\text{CFL}} = 1.3$.

Each simulations is performed on using 288 cores at 2.4 GHz clock speed. The simulation wall clock time and speedup of the harmonics balance solver are summarized in Figure 2.29. The conventional time-stepping simulation took 30.3 hours to run for 4 car-

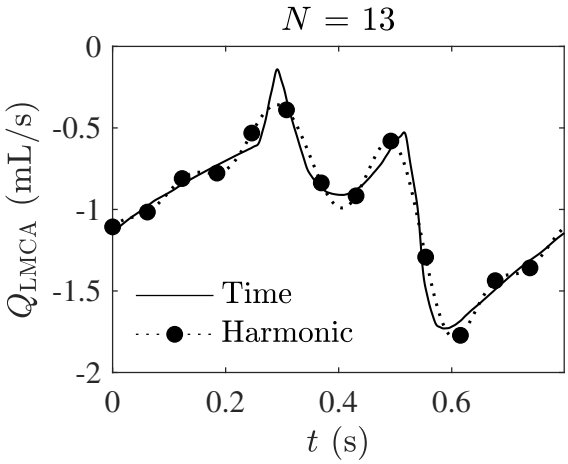

Figure 2.26: Discretized harmonics balance boundary conditions at each time point (black circle) on LMCA inlet. The dotted line represents the reconstructed profile from the time points. For reference, the solid line is the original flow profile in time. $N = 13$.

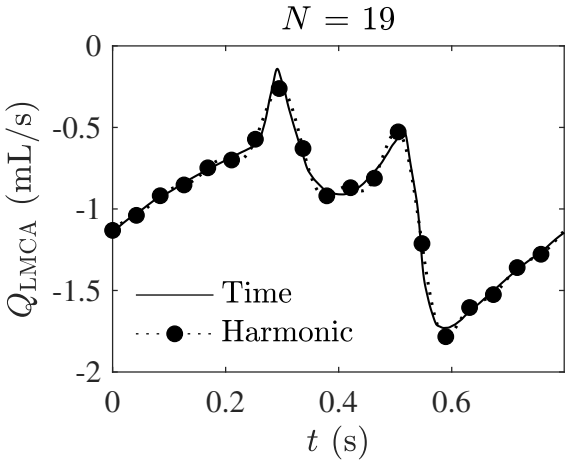

Figure 2.27: Discretized harmonics balance boundary conditions at each time point (black circle) on LMCA inlet. The dotted line represents the reconstructed profile from the time points. For reference, the solid line is the original flow profile in time. $N = 19$.

diac cycles, using 800 time steps per cycle. The cost scaling trend is similar to that of the cerebral flow cases, going from $O(N)$ to $O(N \log(N))$ as N increases. For the most number of time points used ($N = 25$), the harmonics balance solver is still more than 30 times faster than the conventional time solver.

The pressure and velocity magnitude contours for the harmonic balance solver solution using $N = 25$ and the conventional time solver solution are shown in Figure 2.30. The snapshots are taken at $t = 0.5$ seconds in the cycle.

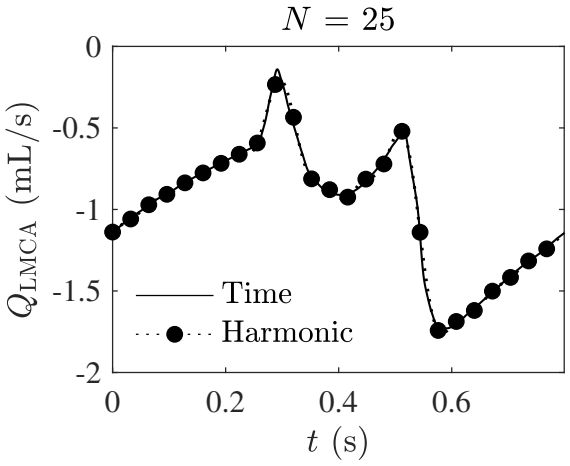

Figure 2.28: Discretized harmonics balance boundary conditions at each time point (black circle) on LMCA inlet. The dotted line represents the reconstructed profile from the time points. For reference, the solid line is the original flow profile in time. $N = 25$.

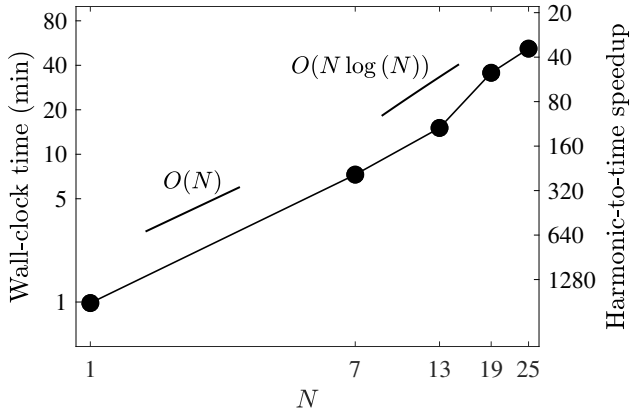

Figure 2.29: The cost performance of the harmonic balance solver for the coronary flow case. The left axis shows the wall-clock time of the harmonic balance simulations. The right axis shows the speedup of the harmonic balance simulations compared to the conventional time-stepping simulation.

The spacial integral relative errors, E_Ω, are presented in Figure 2.31 and2.32 as functions of time in the cardiac cycle. Note that only $N = 13$ and 25 results are shown for graph clarity purposes. The errors lower as the number of time points used increases. The times in the cycle where the errors peak coincide with the times when the inlet flow profile exhibits sharp changes. Although the maxima of the error curves can be fairly large, the duration of these error spikes is short, which means that their effects are not significant to the overall solution accuracy.

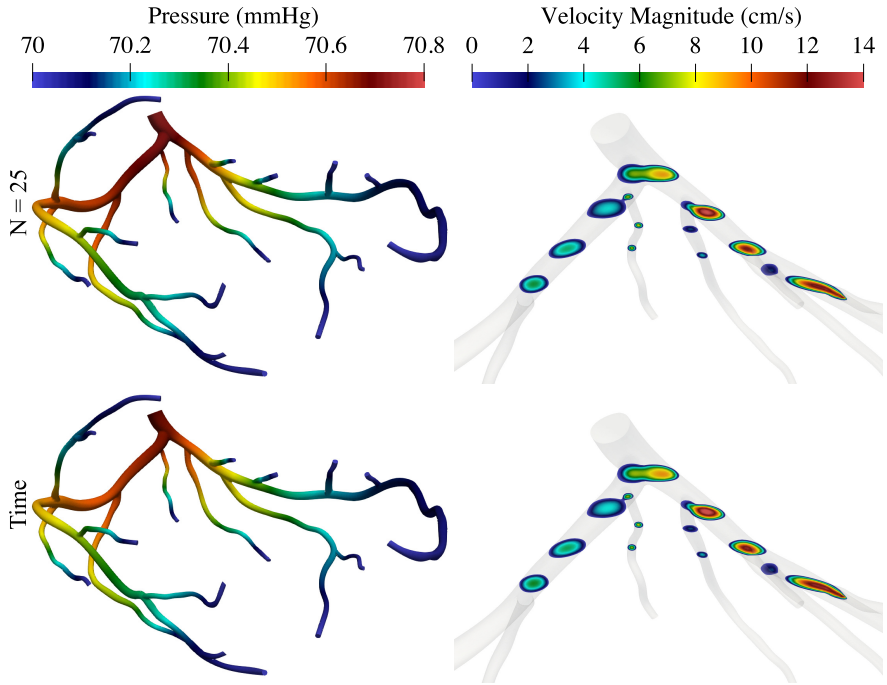

Figure 2.30: Harmonics balance results using $N = 25$ compared to the conventional time results for the coronary flow case. The pressure and velocity magnitude contours are taken at $t = 0.5$ seconds of the cardiac cycle.

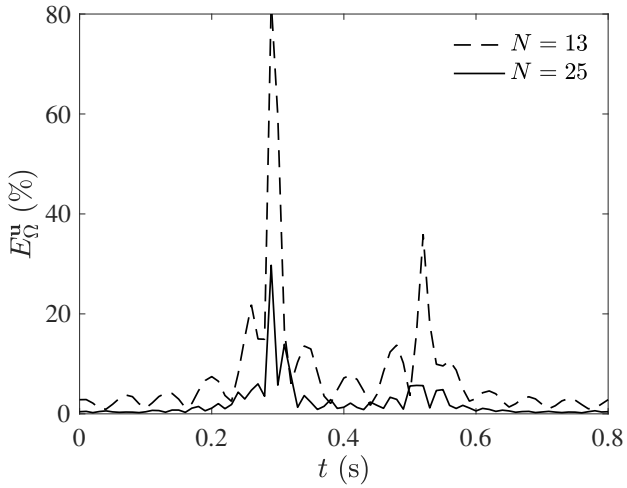

Figure 2.31: The volumetric integral relative root mean square error over the fluid domain for the velocity vector as functions of time in the cardiac cycle of the coronary flow.

Taking both the spacial and time integral of the relative error in Figure 2.33 shows that the harmonics balance velocity result is within 5% of that of the conventional time solver results when $N > 19$. This result also show the significant error produced by the steady state flow assumption ($N = 1$). Similar to the cerebral flow case, the inlet boundary

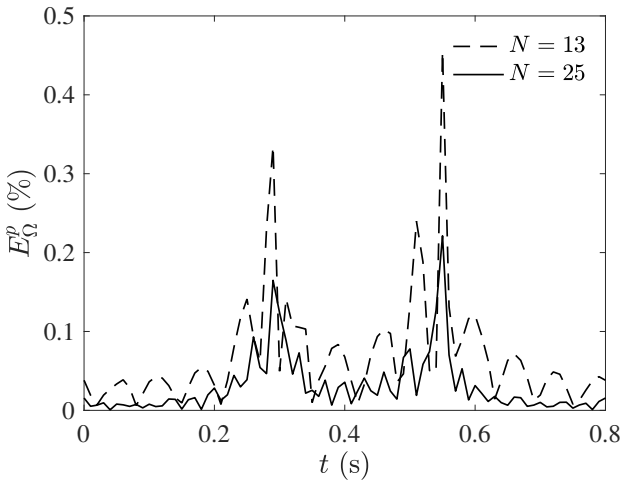

Figure 2.32: The volumetric integral relative root mean square error over the fluid domain for the pressure as functions of time in the cardiac cycle of the coronary flow.

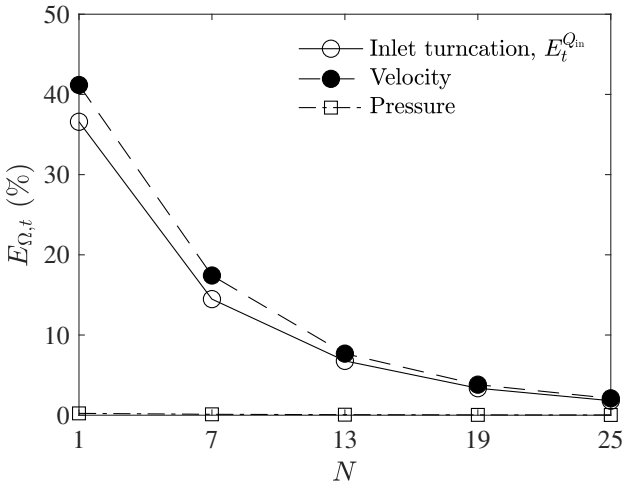

Figure 2.33: Left main coronary arteries flow relative root mean square error for the velocity and pressure integrated over the fluid domain and one cardiac cycle.

condition truncation error is a good estimate of the overall error in the solution domain due to the flow's low Reynolds number.

For certain parameters of interest, the results error will be even smaller than the inlet truncation error due to the fluid viscous effect, which smooths out the sharp changes of the inflow over the length of the fluid domain. For example, the flow rate out of the left anterior descending artery (LAD), marked in Figure 2.25, can be already well captured by using 13 time points ($N = 13$), as shown in Figure 2.34. As shown in Figure 2.35, the errors

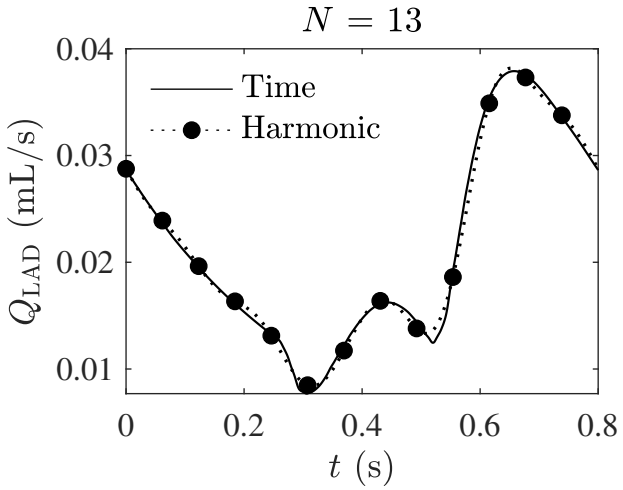

Figure 2.34: Left anterior descending artery (LAD) flow rate results obtained with the harmonics balance solver (solid circles) and the with the conventional time solver (solid line). The dotted line represents the reconstructed profile from the harmonics balance time points. N = 13.

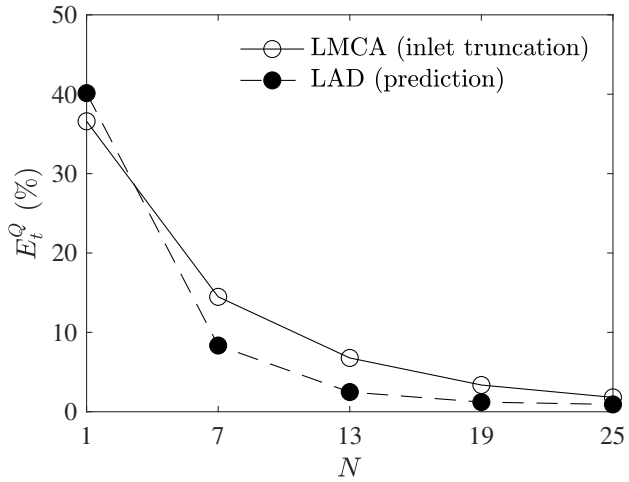

Figure 2.35: Left main coronary arteries flow relative root mean square error for the inlet LMCA flow rate (truncation) and the outlet LAD flow rate (prediction).

for the LAD flow rates are all under 3% for the cases simulated. The flow rate errors for the LAD outlet are also well below the inlet truncation error at the LMCA.

2.4 Discussion

The above results demonstrated that the proposed harmonic balance CFD solver is a viable option for performing various cardiovascular simulations and provides a significant speedup. The requirements for performing harmonics balance CFD simulations are almost identical to those for conventional CFD simulations: a discretized computational domain (mesh) and boundary conditions. In addition to two requirements on the flow field: 1. the flow needs to exhibit a periodic behavior, which is fundamentally satisfied by cardiovascular flows, and 2. there are no geometry-triggered instabilities or turbulence in the fluid field, which means that the Reynolds number has to be below the transitional flow Reynolds number, typically between $2,500$ and $3,000$. For cardiovascular flows, the Reynolds number can only exceed this limit in the aorta, where the peak Reynolds number can be around $4,000$, which is why we did not include the aorta in the coronary flow case. Nonetheless, a significant part of the human circulatory system falls within the limit, and the proposed harmonic balance solver can benefit hemodynamics simulations. Since the proposed harmonic balance solver is based on the fundamental conservation laws, the simplicity of the requirements to run the harmonic balance CFD simulations helps distinguish it from other cost-reducing methods, such as lumped parameter networks or data-driven models, which all require extensive training and model building prior to the simulations.

For all cases simulated in this study, even those requiring a large number of time points, the harmonic balance solver is 10 to more than 100 times faster than the conventional time solver. This impressive speedup is made possible by using the fast Fourier transform scheme in the implementation of the solver to achieve $O(N \log(N)$ scaling, which is a clear distinction from our previous paper where the second-order cost scaling ($O(N^2)$) decimates the speedup advantage when the number of captured frequency gets large. The harmonics balance solver has the same parallel scalability advantage that

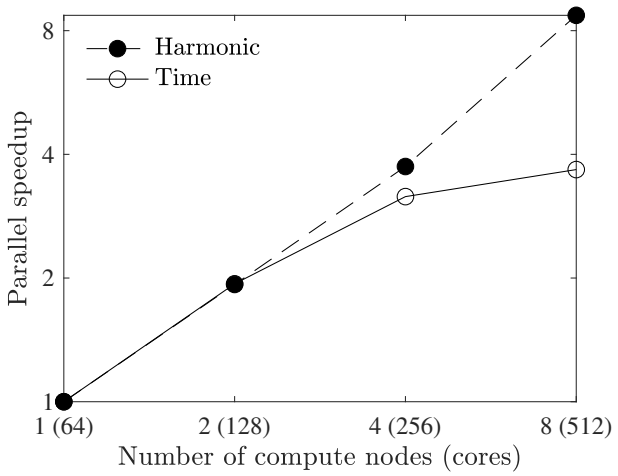

Figure 2.36: [NOTE: this result is incomplete, will update in final version] Strong scaling of the harmonic balance and the conventional time-stepping solvers using the $N = 25$ case in Section 3.3.

came for "free" without changing the parallelization scheme from the conventional solver as detailed in the previous study [46]. As shown in Figure 2.36, the harmonics balance simulations can be run on more parallel cores than the conventional time CFD solver while maintaining strong scaling.

The results from all three cases show that the truncation error from the boundary condition is a good indicator of the solution error. The choice of N for running using the harmonic balance simulations can be decided by how much solution error the user is willing to accept, indicated by the boundary condition truncation error. For simulations with intermediate Reynolds numbers on the order of $1,000$, simulating a few additional time points is beneficial for accessing the higher frequency flow information created by the convective term. It is important to note that the study does not determine the harmonics balance solver's true error compared to real-life physical measurements since all errors are reported relative to the conventional time solvers. Our previous paper has provided an extensive error analysis and provided the bounds of the numerical errors on the frequency form solver [46].

One potential improvement to the proposed solver is the implementation of resistance

outlet boundary conditions. This boundary type is considered more physiological accurate [180]. For resistance boundaries, the pressure at the boundary becomes proportional to the instantaneous flow rate that that surface. As a result, the the pressure error resulting from resistance boundaries will be proportional to the outlet flow rate error.

Future applications of the harmonic balance solver include respiratory flow simulations, which are also periodic in time, and the peak Reynolds number is typically less than $2,000$. Broadly speaking, the harmonic balance CFD solver is an excellent tool for any other application with a time-periodic flow field and low to intermediate Reynolds number flow. Using the harmonics balance CFD solver solutions to build lumped parameter networks or generate machine learning datasets can also be studied. It has the potential to significantly speed up the process of constructing and training these models. Future addition to the solver can include the use of resistance outlet boundary conditions, where the pressure is calculated based on the flow rate through the boundary. This boundary condition is more physiologically accurate than the current Neumann condition. The proposed solver can be coupled with fluid-structure interaction codes, in which governing equations must be formulated in the harmonics balance form.

CHAPTER 3

A TIME-CONSISTENT STABILIZED FINITE ELEMENT METHOD FOR FLUIDS WITH APPLICATIONS TO HEMODYNAMICS

3.1 Introduction

Studies of the human cardiovascular system have greatly benefited from the advances in computational fluid dynamics (CFD) since the end of the 20th century[173, 174, 171]. Among the numerical methods for solving the Navier-Stokes equations[55, 102, 77], the finite element method has found popularity for cardiovascular CFD simulations because it is a convenient framework for dealing with complex geometries and modeling fluid-structure interaction[184, 14, 15, 145]. Together with advancements in clinical imaging techniques[108, 41, 153, 109], CFD simulations using the finite element method have taken a significant part in in-vitro studies, clinical diagnosis, and surgical planning for cardiovascular diseases[4, 169, 96, 150, 172, 123].

The finite element method for solving the unsteady Navier-Stokes equations relies on an upwind term that adds an artificial diffusion along the stream-wise directions, weighted by a stabilization parameter τ, to prevent nonphysical oscillations inherent to the Galerkin method in strongly convective regimes[23, 79, 156, 64]. One of the most commonly used formulations of τ has been the one proposed in the streamline upwind Petrov-Galerkin formulations (SUPG)[23], τ_{SUPG}, which is also adopted in others such as the residual-based variational multiscale (RBVMS) formulation[2, 10].

Traditionally, the steady form of τ_{SUPG} is derived from a 1D steady advection-diffusion model problem, such that the added diffusion to the Galerkin's formulation is just enough to recover the exact solution, thereby eliminating numerical oscillations at higher element Peclet numbers[23, 79, 177, 155]. While this steady form of τ_{SUPG} works well for

strongly advective steady-state flows, it is not readily applicable to time-varying flows, as it exhibits poor convergence behavior, particularly at smaller time step sizes (Δt). The traditional strategy to overcome this issue has been adding a Δt-dependent term to the definition of τ_{SUPG}[79, 155, 32]. The added Δt-dependent term, which is based on the discrete approximation of the inverse of the strong differential operator, dominates the contributions associated with the advection and diffusion terms at small time step sizes. This design, which has found widespread use for its excellent convergence characteristics, produces a strong solution dependency on the time step size, such that the solution becomes less accurate as the time step size is reduced toward zero[19, 34, 75] (also see the results section). As a consequence, this time step size-dependent design of τ_{SUPG} produces an inconsistent method with regard to the time step size. This inconsistency issue is particularly exacerbated in a subset of cardiovascular simulations that demand a small time step size for their multiscale behaviors, such as those involving lumped parameter network modeling[144, 187, 127, 6]. In fact, some of the most popular packages for cardiovascular simulation[183, 7] are based on a stabilized finite element formulation that also suffers from the described issue, thereby motivating the present study.

There has been some effort in the past to overcome the inconsistency issue associated with this design of τ_{SUPG}[19, 91, 25]. T.E. Tezduyar and others introduced an element-vector-based τ_{SUPG} that uses the relative elemental magnitude of terms in the weak form of the Navier-Stokes equations[178, 75]. Although time step size dependency is not entirely eliminated with the proposed formulation, a notable reduction in the solution variation with the time step size was reported in turbulent channel flow simulations. Furthermore, this method relies on sets of integrals on each element that must be performed before the evaluation of the discrete form at the Gauss quadrature. Thus, it may not be simple to implement this technique in an existing finite element program that is not already designed based on the element-vector-based method. In another study, R. Codina and others proposed a subscale-tracking approach that solves a time-dependent ordinary differential

equation at each Gauss integration point to evolve its stabilization parameter in time[34]. This method eliminates the time step size dependency for steady-state solutions. The additional computational cost to solve an ordinary differential equation at each Gauss point, however, is non-negligible for this method. Despite the relatively better time step size consistency shown by these methods in the numerical experiments, they have not found widespread implementation in cardiovascular simulations [93, 183].

In this study, we propose a formulation for τ_{SUPG} that eliminates the solution's dependency on the time step size. This method is simple to implement in existing CFD solvers that are based on the streamline upwind Petrov-Galerkin and pressure stabilizing Petrov-Galerkin (SUPG/PSPG) method. More specifically, we replace the inverse of the time step size in the definition of the τ_{SUPG} with a measure of the flow frequency. The motivation behind such formulation lies in the spectral formulation of the unsteady Stokes equations where the time step size dependent parameter in the τ_{SUPG} is replaced by the spectral mode number[45]. The same parameter, when expressed in a spatio-temporal setting, inspires the use of a flow-dependent time scale in the τ_{SUPG} definition, hence motivating the present design.

The idea of replacing the time step size in τ_{SUPG} with an acceleration-to-velocity ratio has been proposed independently earlier by J. Evans and others[54] to simulate turbulent flows. Our present study nonetheless distinguishes from the previous study both in the formulation and the application. First, the previous study adopts an elemental measure of velocity and acceleration, while we use the global-averaged values in defining τ_{SUPG}. As we discuss later in the formulation section, this choice was made for stability reasons. While a local measure produces stable results when used in conjunction with an explicit time integration, it creates instabilities in implicit solvers, which is the concern of the present study. Second, the present study investigates the behavior of the new τ_{SUPG} using a range of canonical and realistic anatomical cases, thereby evaluating its potential for

cardiovascular simulations.

The article is organized as follows: We first present the formulation of the stabilized finite element method for the Navier-Stokes equations, the motivation behind the proposed τ_{SUPG}, and its formulation. We present four cases to compare the present formulation against the conventional one: a pipe flow with steady boundary conditions, a time-periodic blood flow in a complex cardiovascular geometry (modified Blalock-Taussig shunt), a two-dimensional external flow over a square, and a two-dimensional flow over a square with an attached flexing beam. We will also discuss the convergence and computational cost of the present formulation. Lastly, we conclude our study and discuss the future outlook in the broader fields of cardiovascular simulations and stabilized finite element methods.

3.2 Formulation

The Navier-Stokes equations for incompressible flows are stated as

$$\begin{aligned} \mathbf{R}_{\text{M}} = \rho\left(\frac{\partial \mathbf{u}}{\partial t} + \mathbf{u}\cdot\boldsymbol{\nabla}\mathbf{u} - \mathbf{f}\right) - \boldsymbol{\nabla}\cdot\boldsymbol{\sigma} = \mathbf{0} \qquad & \text{in } \Omega\times(0,T], \\ R_{\text{C}} = \boldsymbol{\nabla}\cdot\mathbf{u} = 0 \qquad & \text{in } \Omega\times(0,T], \end{aligned} \tag{3.1}$$

where ρ is the density, $\mathbf{u}(\mathbf{x},t)$ is the velocity, $\mathbf{f}(\mathbf{x},t)$ is the external forcing, $\Omega\times[0,T]$ is the fluid computational spatio-temporal domain, and the stress tensor

$$\begin{aligned} \boldsymbol{\sigma}(p,\mathbf{u}) &= -p\mathbf{I} + 2\mu\boldsymbol{\epsilon}(\mathbf{u}), \\ \boldsymbol{\epsilon}(\mathbf{u}) &= \frac{1}{2}\left((\boldsymbol{\nabla}\mathbf{u}) + (\boldsymbol{\nabla}\mathbf{u})^{\intercal}\right), \end{aligned} \tag{3.2}$$

where $p(\mathbf{x},t)$ is pressure and μ is the dynamic viscosity. The Dirichlet and Neumann boundary conditions are defined as

$$\begin{aligned} \mathbf{u} &= \mathbf{g} \quad \text{on } \Gamma_{\text{g}}, \\ \boldsymbol{\text{œ}}\mathbf{n} &= \mathbf{h} \quad \text{on } \Gamma_{\text{h}}, \end{aligned} \tag{3.3}$$

respectively, where Γ_g and Γ_h are subsets of the boundary Γ where the Dirichlet and Neumann boundaries are prescribed, $\mathbf{n}$ is the outward unit normal vector, and $\mathbf{g}$ and $\mathbf{h}$ are the given Dirichlet and Neumann boundary conditions, respectively.

The discrete form of the Navier-Stokes equations we used in this study is stated as finding $\mathbf{u}^h \in S^h_{\mathbf{u}}$ and $p^h \in S^h_p$ such that for all $\mathbf{w}^h \in V^h_{\mathbf{u}}$ and $q^h \in V^h_p$,

$$\int_\Omega \mathbf{w}^h \cdot \rho\left(\frac{\partial \mathbf{u}^h}{\partial t} + \mathbf{u}^h \cdot \boldsymbol{\nabla}\mathbf{u}^h - \mathbf{f}\right) d\Omega + \int_\Omega \boldsymbol{\epsilon}\left(\mathbf{w}^h\right) : \boldsymbol{\sigma}\left(p^h, \mathbf{u}^h\right) d\Omega - \int_{\Gamma^h} \mathbf{w}^h \cdot \mathbf{h}^h d\Gamma + \int_\Omega q^h \boldsymbol{\nabla} \cdot \mathbf{u}^h d\Omega + \sum_{e=1}^{n_{el}} \int_{\Omega^e} \left[\tau_{\mathrm{SUPG}}\left(\mathbf{u}^h \cdot \boldsymbol{\nabla}\mathbf{w}^h + \frac{1}{\rho}\boldsymbol{\nabla} q^h\right) \cdot \mathbf{R}_{\mathrm{M}}{}^h + \rho \nu_{\mathrm{C}} \nabla \cdot \mathbf{w}^h R^h_{\mathrm{C}}\right] d\Omega = 0. \quad (3.4)$$

In the above problem statement, $S^h_{\mathbf{u}}$ and S^h_p are the discrete solution spaces for the velocity and pressure, respectively, and $V^h_{\mathbf{u}}$ and V^h_p are the finite-dimensional test function spaces for the velocity and pressure, respectively.

In Equation (3.4), the terms directly obtained from Equation (3.1) are supplemented with three elemental stabilization terms. The two terms multiplied by τ_{SUPG} are the conventional SUPG and PSPG stabilizations to ensure stability in strongly convective flows and allow for equal order interpolation functions for velocity and pressure, respectively[23, 79]. The term involving ν_{C} comes from the residual-based variational multiscale methods (VMS)[11, 13, 1]. While there are some variations in defining these terms, we consider

$$\tau_{\mathrm{SUPG}} = \left(\left(\frac{2}{\Delta t}\right)^2 + \mathbf{u}^h \cdot \boldsymbol{\xi}\mathbf{u}^h + C_{\mathrm{I}}\nu^2 \boldsymbol{\xi} : \boldsymbol{\xi}\right)^{-\frac{1}{2}}, \quad (3.5)$$

and

$$\nu_{\mathrm{C}} = \left(\mathrm{tr}\left(\boldsymbol{\xi}\right)\, \tau_{\mathrm{SUPG}}\right)^{-1}, \quad (3.6)$$

as the common conventional definition of these stabilization parameters for later comparisons[155, 11, 176]. In Equation (3.5), $\nu = \mu/\rho$ is the kinematic viscosity, Δt is the time step size, $\boldsymbol{\xi}$ is the covariant tensor obtained from the mapping of the physical-parent elements, and C_{I} is a shape-function-dependent constant, which is 3 in our study.

The inconsistency of the above-mentioned stabilized formulation is caused by Δt in τ_{SUPG}. In a steady flow, in which the solution should be independent of Δt, τ_{SUPG} and thus the overall added diffusion will change with Δt, creating a time step size dependent solution. In the later sections, we will demonstrate that this inconsistency issue is not unique to steady-state flows and also occurs for unsteady flows.

In an earlier study, we introduced a pressure-stabilized technique for solving the unsteady Stokes equations expressed in the frequency domain rather than the time domain[45]. The resulting complex-valued stabilization parameter was derived systematically by taking the divergence of the momentum equation and estimating the Laplacian in the diffusion term using a characteristic element size. The modulus of that PSPG-type stabilization parameter is

$$|\tau| \propto \left(\omega^2 + \nu^2 \boldsymbol{\xi} : \boldsymbol{\xi}\right)^{-1/2}, \tag{3.7}$$

where ω is the spectral mode appearing as a source term in the frequency formulation of the unsteady Stokes equations. This spectral formulation of τ closely resembles the conventional definition of τ_{SUPG} in Equation (3.5) if $2/\Delta t$ is replaced by ω. The $\mathbf{u}^h \cdot \boldsymbol{\xi}\mathbf{u}^h$ term does not appear in Equation (3.7) as the convective acceleration term is not present in the unsteady Stokes equations. Adding this term into Equation (3.7) and incorporating the $O(1)$ constant C_{I} results in

$$\tau_{\text{SUPG}} = \left(\omega^2 + \mathbf{u}^h \cdot \boldsymbol{\xi}\mathbf{u}^h + C_{\text{I}}\nu^2 \boldsymbol{\xi} : \boldsymbol{\xi}\right)^{-1/2}, \tag{3.8}$$

which is adopted in this study to replace the conventional definition of τ_{SUPG} from Equation (3.5) when solving Equation (3.4).

The new definition of τ_{SUPG} in Equation (3.8) becomes identical to the traditional formulation (Equation (3.5)) if $\omega = 2/\Delta t$. This value is close to the largest frequency associated with the time discretization, namely $\pi/\Delta t$ that occurs when the solution oscillates between consecutive time steps. In practice, especially in cardiovascular simulations, the

solution is a much smoother function of time and has a frequency content that peaks at a much smaller ω than $\pi/\Delta t$. The distinction of these two frequencies inspires the proposed definition of τ_{SUPG}.

It is straightforward to evaluate Equation (3.8) in a spectral formulation as ω is the computed frequency and readily available as an independent parameter. However, its adoption is not straightforward in a traditional time formulation, where ω does not appear as an independent parameter. Ideally, ω must satisfy several properties. First, it must produce a scheme that remains stable under a variety of conditions. Second, it must be extracted from physical variables, such as the velocity and acceleration, rather than the time step size, so that τ_{SUPG} converges to a unique quantity as the time step size goes to zero. Third, it should be simple to implement and cost-efficient to calculate. Given these criteria, we propose

$$\omega = \frac{||\frac{\partial \mathbf{u}^h}{\partial t}||_{L^2}}{||\mathbf{u}^h||_{L^2}}, \tag{3.9}$$

where $||\mathbf{f}||^2_{L^2} = \int_\Omega ||\mathbf{f}||^2 d\Omega$. This formulation of ω is designed to go to zero as the flow reaches a steady state, where $\frac{\partial \mathbf{u}^h}{\partial t}$ goes to zero. We will show in the results section that this formulation is consistent in both steady and unsteady flows as $\Delta t \to 0$. We will also show that the present formulation is relatively robust even though it increases the computational cost compared to the conventional method.

For moving domain simulations that express Equation (3.4) in an arbitrary Eulerian-Lagrangian framework, $\mathbf{u}^h$ in the convective acceleration term is replaced by the fluid velocity relative to moving mesh $\mathbf{u}^h - \hat{\mathbf{u}}^h$, where $\hat{\mathbf{u}}^h$ denotes mesh velocity. It is this velocity that is employed in the definition of τ_{SUPG} and also ω in Equation (3.9), changing it to

$$\omega = \frac{||\frac{\partial \mathbf{u}^h}{\partial t}|_{\hat{\mathbf{x}}}||_{L^2_{\Omega^f}}}{||\mathbf{u}^h - \hat{\mathbf{u}}^h||_{L^2_{\Omega^f}}}, \tag{3.10}$$

where the acceleration term is measured at the mesh node location $\hat{\mathbf{x}}$ and integrals performed over the fluid domain Ω^f. By subtracting the mesh velocity from the fluid velocity

in Equation (3.10), the resulting definition of ω will be Galilean invariant. This results in a scheme that produces a unique solution if all velocities were to be measured from a moving inertial reference frame. Later in the result section, we demonstrate the consistency of this method in a moving domain configuration using a fluid structure interaction simulation test case.

Ideally, one would compute velocity and acceleration locally at the Gauss quadrature point when evaluating ω so that the solution becomes a function of the local dynamics of the problem. Unfortunately, this choice, which has been successfully employed with explicit time integration in the past[54], fails to converge in our implicit formulation. This lack of convergence can be attributed to the velocity appearing in the denominator of Equation (3.9), thereby creating widely varying ω in regions where flow is temporarily stagnant. This convergence issue is avoided for all cases tested here by using a global measure of velocity and acceleration through integrating their norms over the entire domain as in Equation (3.9).

In theory, using a global measure of velocity and acceleration could produce a solution that depends on the domain size. Consider an external flow over an obstacle in which the $||\frac{\partial \mathbf{u}^h}{\partial t}||_{L^2}$ term receives non-zero contribution only from regions near the obstacle whereas $||\mathbf{u}^h||_{L^2}$ receives a contribution from the entire domain. In this setting, ω goes to zero as the size of the computational domain grows, resulting in a domain size-dependent value.

As we will show later in the results section, this domain-size dependency issue does not translate to inconsistency of the formulation in practice. That is because the ω^2 term in Equation (3.8) is much smaller relative to the sum of the other two terms. In fact, we show that the solution obtained from the proposed formulation is very similar to that of the conventional formulation with a very large Δt. Therefore, increasing the domain size will decrease a parameter in the definition of τ_{SUPG} that is already small, thus hardly changing the solution.

Even though the ω^2 value in τ_{SUPG} is very small, dropping it from its definition will create convergence issues, as it has been established in the past[177, 155]. The reason that the inclusion of the ω^2 term in τ_{SUPG} prevents such scenarios is that a widely varying solution in time will lead to a relatively large ω. As a result, the contribution of ω grows as the solution becomes more unstable, thereby creating a recovery effect that stabilizes the simulation.

In CFD applications, the velocity field may be initialized from zero, thus creating a divide-by-zero operation in the code when evaluating Equation (3.9). To avoid such possibilities, we set $\omega = 2/\Delta t$ at the first time step, recovering the conventional definition of τ_{SUPG}.

As detailed in a previous publication[50], we use the implicit generalized-α time integration scheme[85] in our solver. The use of this time integration scheme significantly simplifies the implementation of the proposed formulation since velocity and acceleration are readily available as discrete state variables. Thus, in our implementation, $\frac{\partial \mathbf{u}^h}{\partial t}$ and $\mathbf{u}^h$ in Equation (3.9) are explicitly computed from those variables in a single operation. As we will demonstrate in the results, ω is a slowly varying parameter, thus we perform this operation only once in each time step using the solution at the previous time step. Given that the generalized-α method also provides access to variables at the intermediate time points (i.e., $n + \alpha_m$ and $n + \alpha_f$ for the acceleration and velocity, respectively), one may elect to use those intermediate variables to update ω within each Newton-Raphson iterations. This choice, however, is not adopted in this study as it entails extra computations and has little effect on the overall stability of the solver. The rest of the implementation, including the computation of τ_{SUPG} at the Gauss quadrature points based on the intermediate variables are left unchanged and are identical to the conventional formulation.

3.3 Simulations and Results

The above formulation is implemented in our in-house finite-element solver, multi-physics finite-element solver (MUPFES)[127, 50, 49]. A specialized iterative algorithm, preconditioner, and parallelization strategy are employed for an efficient and scalable solution of the linear system of equations[49, 50, 47, 111]. The solver has been verified[165] and extensively employed for cardiovascular modeling in the past[52, 51, 90]. This solver is parallelized using a message passing interface (MPI). The workload is parallelized using spatial partitioning by employing ParMETIS library[95]. All computations are performed on a cluster of AMD Opteron™ 6378 processors that are interconnected via a QDR Infiniband.

At each time step, several Newton-Raphson iterations are performed to ensure the residual falls by over three orders of magnitude. At each Newton-Raphson iteration, a linear system is solved using the generalized minimal residual (GMRES) method[149] with a tolerance of 10^{-2}.

Four cases are simulated using both the conventional formulation (Equation (3.5)) and the present formulation (Equation (3.8)) for τ_{SUPG}: a pipe flow, flow in a modified Blalock-Taussig shunt geometry[52], a two-dimensional external flow over a square, and a flow over a square with an attached flexible beam. These numerical experiments are designed to stress-test various aspects of the two formulations in canonical and physiologic settings. More specifically, these cases represent three classes of flow simulations where 1) the boundary conditions and the solution are both steady, 2) the boundary condition and the solution are both unsteady, 3) the boundary conditions are steady but the solution is unsteady (in this case due to vortex shedding), and 4) the fluid domain is not fix with unsteady solution. All of the simulations are initialized using $\mathbf{u_0} = 0$ and continued in time to reach cycle-to-cycle convergence or steady-state solutions. For apple-to-apple compar-

ison, all parameters, except for the τ_{SUPG} definition, are kept the same when comparing the present formulation against its conventional counterpart.

3.3.1 Steady pipe flow

We first consider the case of flow in a straight pipe with steady boundary conditions, which can be considered the most simple and fundamental flow in the cardiovascular system with an existing analytical solution for comparison. In our simulations, a steady flow rate is imposed at the inlet and the pressure drop across the pipe is predicted using the present and conventional methods. The pipe has a length of 15 cm and a radius of 1 cm. A parabolic velocity profile is imposed at the inlet with an amplitude that results in a 10 mL/s flow rate. A zero Neumann boundary condition is imposed at the outlet. The dynamic viscosity is fixed at 1 g/cm-s. Three different densities, 1.571, 15.71, and 157.1 g/mL are selected to produce three Reynolds numbers (Re), 10, 100, and 1000, respectively. This way, we capture a wide range of Reynolds numbers that occur in cardiovascular flows[121]. For all cases, the pressure drop must remain the same according to the Hagen–Poiseuille analytical solution[167], thereby allowing us to measure the accuracy of each method.

The mesh generated for this case contains $207,063$ tetrahedral elements, which are used for the velocity and pressure interpolation as well as their test functions. Each Reynolds number is simulated using four different time step sizes of $\Delta t = 10^{-1}$, 10^{-2}, 10^{-3}, and 10^{-4} seconds. This range of time step sizes, which is typical in cardiovascular simulations, results in Courant–Friedrichs–Lewy numbers (CFL $= \overline{u}\Delta t/\overline{\Delta x}$) ranging from 5.2 to 5.2×10^{-3}, based on the mean element size of the mesh, $\overline{\Delta x}$, and the mean flow velocity, $\overline{u}$. This range of CFL numbers, which captures under-resolved to over-resolved time discretizations, can be encountered in a typical simulation due to the differences in

velocity and mesh resolution in different cardiovascular branches. Furthermore, multi-domain simulations can require the use of a smaller time step size (hence CFL) to ensure stability[127].

All simulation cases were run in parallel with 32 cores. Equations are integrated for five seconds (approximately three flow-through times) to ensure steady conditions are reached. The l^2-norm of the residual is dropped by 3.5 orders of magnitude at each time step using Newton-Raphson iterations. Considering three Reynolds numbers, four time step sizes, and two formulations, we ran a total of 24 simulations for this case.

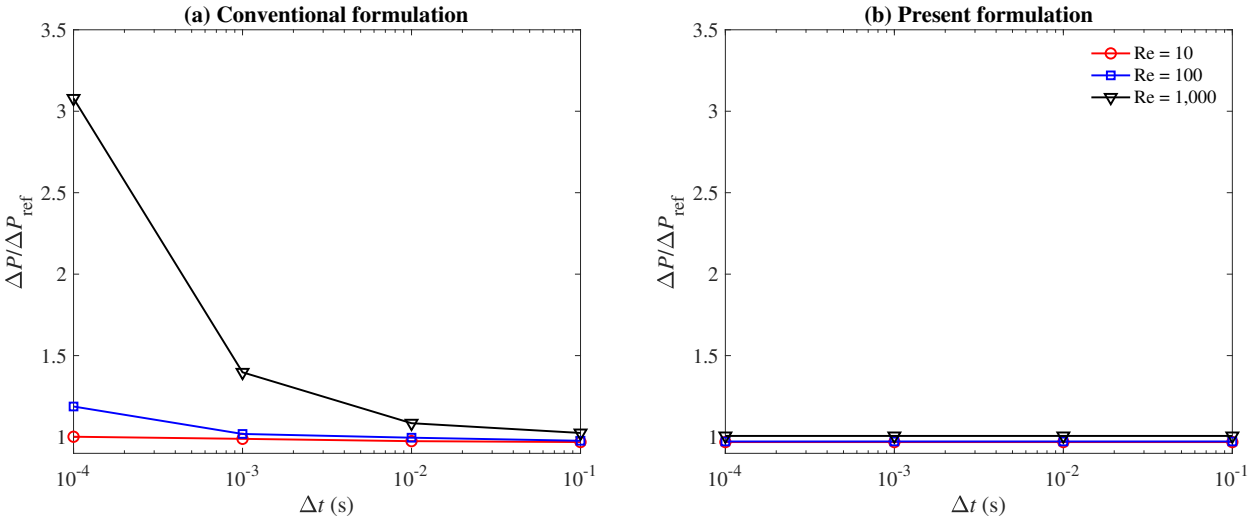

Figure 3.1: The predicted pressure drop normalized by the analytical solution ($\Delta P/\Delta P_{\text{ref}}$) for the steady pipe flow case as a function of the time step size (Δt) for (a) the conventional formulation and (b) the present formulation. The three Reynolds numbers are 10 (red circle), 100 (blue square), and 1,000 (black triangle).

The results for this case are condensed in Figure 3.1, which shows the predicted pressure drop, normalized by that of the Poiseuille solution[167], as a function of the time step size for three different Reynolds numbers. The solutions calculated using the conventional τ_{SUPG} formulation becomes exceedingly less accurate as the Reynolds number is increased and the time step size is reduced (Figure 3.1(a)). That produces a very large error at Re =1,000 and $\Delta t = 10^{-4}$ where the predicted pressure drop is three times that

of the analytical prediction. This large deviation from the reference solution confirms the inconsistency of the conventional formulation that we discussed earlier. This effect is amplified at higher Reynolds numbers when the artificial viscosity introduced through τ_{SUPG} is larger in comparison to the physical viscosity, thus creating a larger variation in the solution as τ_{SUPG} is varied with Δt.

The present formulation, on the other hand, produces predictions that are independent of the time step size, confirming that it is a consistent formulation for steady-state flows (Figure 3.1(b)). The overall error, which is primarily associated with spatial discretization, is negligible in comparison to the conventional formulation. The error for the case discussed above (Re = $1,000$ and $\Delta t = 10^{-4}$) drops from 300% to 0.7% when one uses the present rather than the conventional formulation.

Such a large difference in the solutions can be attributed to the large difference between ω and $2/\Delta t$ term in τ_{SUPG} definition. The large difference between the two is depicted in Figure 3.2 which shows the history of ω over the course of the simulation. Given that $\omega = 2/\Delta t$ at $t = 0$, the two methods are equivalent at the beginning of the simulation. However, as time progresses, the conventional formulation will significantly deviate from the present formulation by producing an ω that differs by around fifteen orders of magnitude.

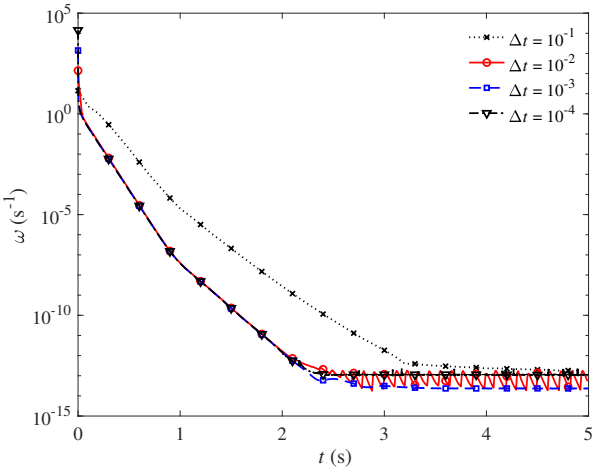

Figure 3.2: The time evolution of ω (Equation (3.9)) over the course of the simulation for the pipe flow case at Re = 10 and at four different time step sizes of $\Delta t = 10^{-1}$ (dotted), 10^{-2} (solid), 10^{-3} (dashed), and 10^{-4} (dot-dashed) seconds.

Given these attractive results and the fact that $\omega \to 0$ in the present formulation, one may be tempted to entirely drop $2/\Delta t$ term from the definition of τ_{SUPG}. As we argued earlier, such a modification results in a method that fails to converge particularly at a relatively small time step size and in cases where the flow is highly unsteady. Such regime corresponds to the initial stage of the pipe flow simulation, where the flow is rapidly evolving and $\omega \neq 0$ (Figure 3.2). Therefore, incorporating ω into the definition of τ_{SUPG} plays a crucial role in improving the stability of the overall scheme.

Lastly, we must note that although the present method converges for all cases considered, it produces a linear system that is stiffer than that of the conventional formulation. As a consequence, the solution of the linear system through an iterative solver will require more iterations, which can be over an order magnitude per time step when compared against the conventional method (Figure 3.3). This larger number of iterations translates to a higher overall cost of these calculations, which is on average twice higher than that of the conventional formulation.

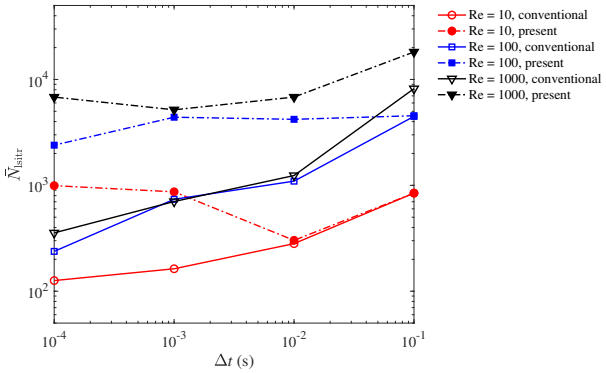

Figure 3.3: The average number of the linear solver (GMRES) iterations per time step ($\bar{N}_{\mathrm{lsitr}}$) as a function of the time step size (Δt) for the steady pipe flow case. The results correspond to the three simulated Reynolds numbers: 10 (red circle), 100 (blue square), and 1,000 (black triangle) using the conventional (solid line) and the present formulation (dot-dashed line) of τ_{SUPG}.

3.3.2 Blood flow in vascular anatomy

In this case, we compare the performance of the conventional formulation and our present formulation in a realistic cardiovascular geometry with a wide range of Reynolds and CFL numbers. The adopted anatomy represents that of an infant who has undergone the modified Blalock-Taussig shunt procedure[52, 51] (Figure 3.4). The geometry contains multiple branches, among which an unsteady flow with a parabolic profile is imposed at the ascending aorta, which is interpolated from earlier multi-domain simulations[90, 87]. Zero Neumann boundary conditions are imposed on all other branches, which are non-physiological, but nevertheless selected to highlight the difference between the two formulations. Since the flow rate through the pulmonary arteries is critical in understanding the performance of the shunt for this procedure, it is used here for simulation results comparison. The blood is assumed Newtonian with a density of 1.06 g/mL and a dynamic viscosity of 0.04 g/cm-s. The Reynolds number ranges from 50 to 1300 depending on the branch and the time within the cardiac cycle. Although the primary source of flow unsteadiness can be traced to the unsteady boundary condition, the complex geometry

may also induce more local variations in the solution as a function of time, in this case (namely, generating frequency content in the solution that is not present in the boundary condition).

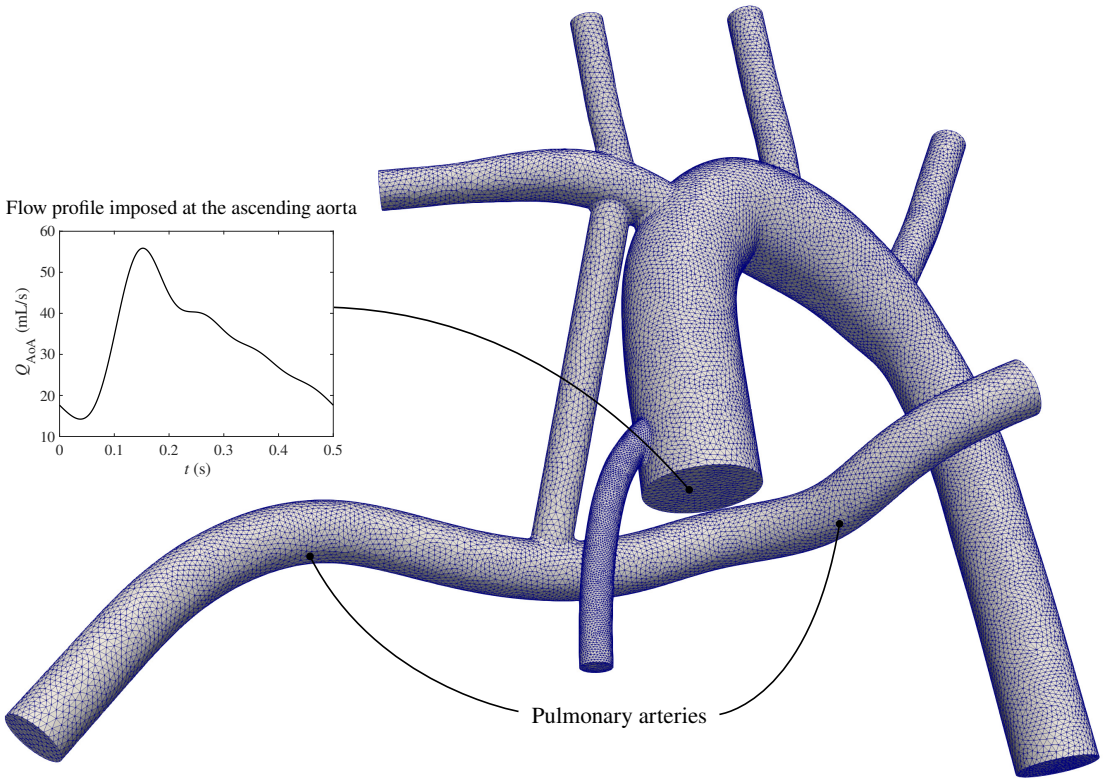

Figure 3.4: The meshed geometry and the inlet condition (the ascending aorta flow rate, Q_{AoA}) for the modified Blalock-Taussig shunt simulation.

We performed simulations using time step sizes of $\Delta t = 2.5 \times 10^{-2}$, 2.5×10^{-3}, and 2.5×10^{-4} seconds, which are within the range of actual time step sizes used for these types of studies[52, 51, 90]. The geometry is discretized using 400,936 tetrahedral elements (Figure 3.4). All simulations are run in parallel with 288 processors. Simulations are continued for at least six cardiac cycles (3 seconds) to ensure cycle-to-cycle convergence.

The predicted flow rate through the pulmonary arteries is extracted as a parameter of interest and plotted over one cardiac cycle in Figure 3.5. For the conventional formulation, we can see a similar trend of solution deterioration as the time step size gets smaller. There

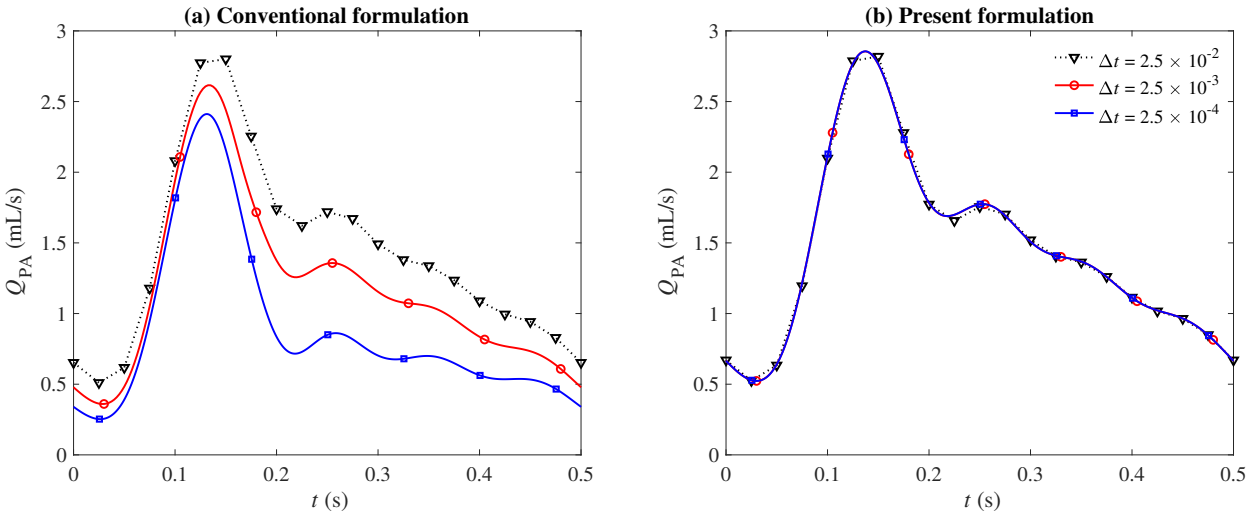

Figure 3.5: The predicted flow rate through the pulmonary arteries (Q_{PA}) using $\Delta t = 2.5 \times 10^{-2}$ (dotted), 2.5×10^{-3} (red circle), and 2.5×10^{-4} (blue square) seconds, when the computations are performed using (a) the conventional formulation and (b) the present formulation of τ_{SUPG}.

is a 10% change in flow rate as the time step size is reduced from 2.5×10^{-2} to 2.5×10^{-3} seconds. There is another 15% deviation in the prediction of the conventional formulation when the time step size is further reduced by another order of magnitude, from 2.5×10^{-3} to 2.5×10^{-4} seconds. Such large variations in the results are rather alarming because 500 times steps per cardiac cycle or more (corresponding to $\Delta t \leq 10^{-3}$) is a very modest number and has been commonly used in the past cardiovascular CFD studies[52, 51, 185, 90, 157, 150]. According to our numerical experiment with the conventional method, such a commonly used time step size is already too small that it produces substantial error in the results.

In contrast to the conventional formulation, the method proposed is consistent with results that are almost independent of the time step size (the observed changes were less than 0.1%). ω values using the present formulation is shown in Figure 3.6 for three different time step sizes. At the beginning of the simulations, ω quickly drops from that of the conventional formulation values to physics-based periodic values. As expected, the converged periodic ω values are almost independent of the time step size, thus resulting

in predictions that do not change as $\Delta t \to 0$.

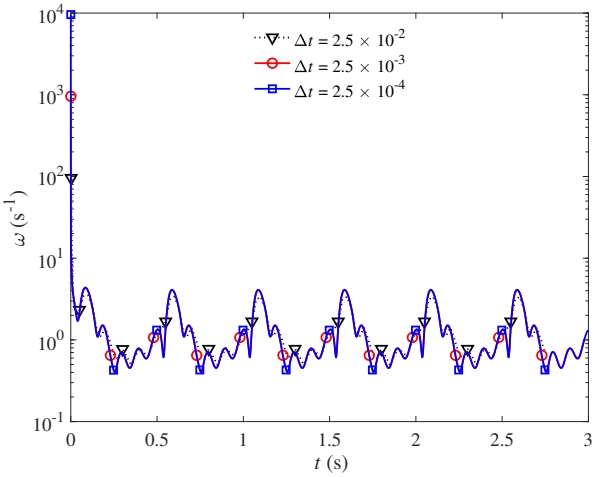

Figure 3.6: ω value used in the present formulation as the simulations progress in time for three different time step sizes, $\Delta t = 2.5 \times 10^{-2}$ (dotted), 2.5×10^{-3} (red circle), and 2.5×10^{-4} (blue square) seconds.

The total CPU time of the computations performed with the present formulation is around 1.5 times that of the conventional formulation, which is acceptable but warrants future improvements. Simulation results generated with the present formulation will enable researchers and clinicians to have high resolution in terms of time discretization without concerns about solution accuracy.

3.3.3 Flow over a square

In this case, we will present a more textbook unsteady CFD numerical experiment to demonstrate that the consistency issue is not unique to cardiovascular applications. We will demonstrate that the present formulation solves the inconsistency issue for this case but also demonstrate where the limitation of our formulation currently lies. We will also use this case to discuss the domain size dependency of (or lack thereof) the present formulation for external flows.

We consider a two-dimensional unsteady flow over a square object with a steady in-

flow boundary condition. The geometry and mesh used for this case are shown in Figure 3.7. The square has a side length of 1 m in a 12 m by 29.2 m fluid domain. The square obstacle is centered vertically and placed at a distance of 5 m from the inlet on the left side of the domain. Uniform horizontal flow with a velocity magnitude of 51.3 m/s is prescribed at the inlet and the outlet is a zero Neumann boundary. The top and bottom of the domain are both no-penetration boundaries ($u_y = 0$) with zero traction in the horizontal direction ($h_x = 0$). The fluid has a density of 1.18×10^{-3} kg/m^3 and a dynamic viscosity of 1.82×10^{-4} kg/m-s. The Reynolds number of this case is 332, which results in vertex shedding downstream of the obstacle.

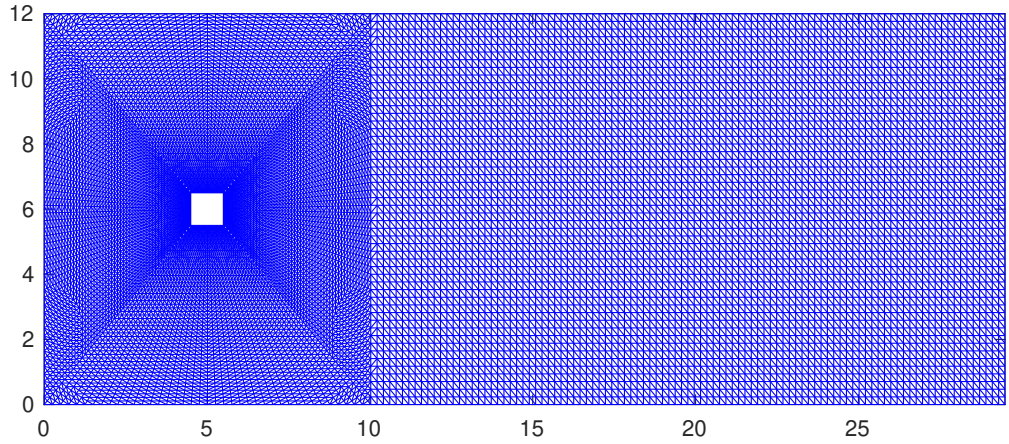

Figure 3.7: The mesh constructed for the flow over a square obstacle simulation.

The mesh generated for this case contains 28,502 triangular elements. Three different time step sizes are considered, $\Delta t = 10^{-3}$, 4×10^{-4}, and 10^{-4} seconds. At each time step, the time integration residual is dropped by more than three orders of magnitude through Newton-Raphson iterations. The simulations are continued for 5 seconds to ensure statistically stationary conditions are established. We used 16 cores to perform these calculations.

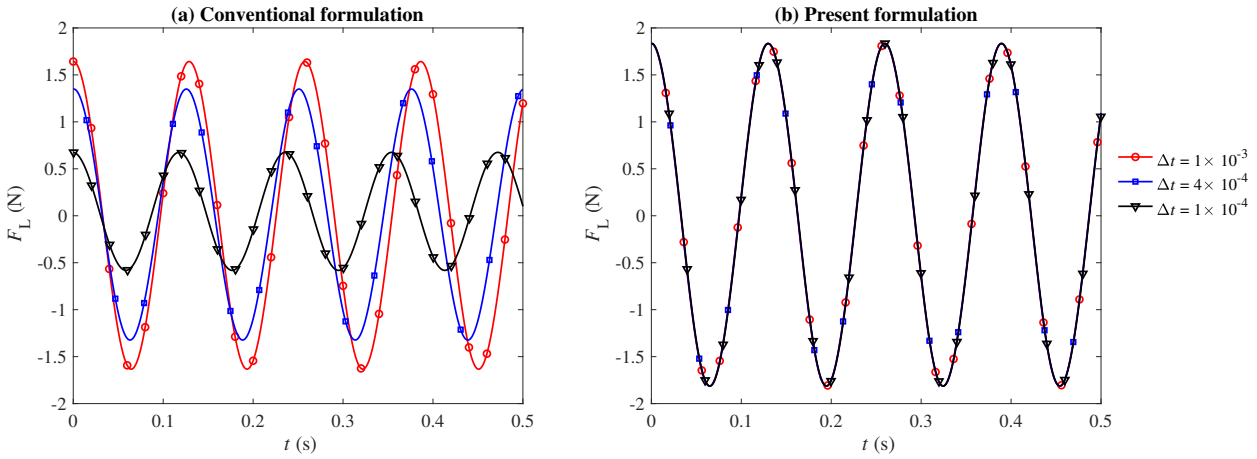

Figure 3.8: Predicted lift on the obstacle (F_L using $\Delta t = 10^{-3}$ (red circle), 4×10^{-4} (blue square), and 10^{-4} (black triangle) seconds, where τ_{SUPG} is computed using (a) the conventional formulation and (b) the present formulation of τ_{SUPG}. Re = 332.

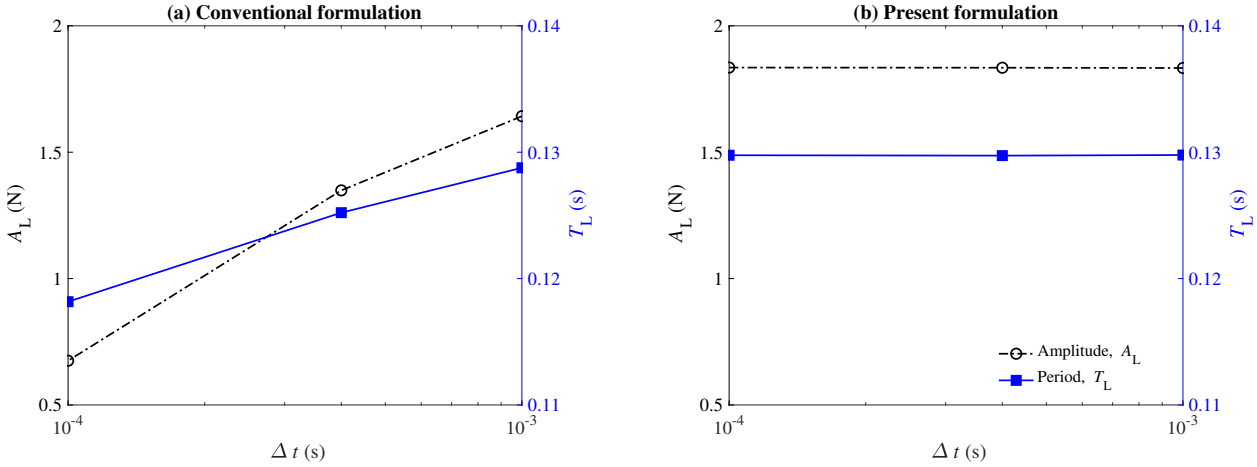

Figure 3.9: Predicted amplitude (black dash-dotted line) and period (blue solid line) of the lift profile as a function of the time step size (Δt) using (a) the conventional formulation and (b) the present formulation.

The lift exerted on the square obstacle during the last 0.5 seconds of the simulation is shown in Figure 3.8. Consistent with what we observed in the previous cases, this case also shows significant improvement in the results when the present design of τ_{SUPG} is adopted. The conventional formulation prediction of the oscillation amplitude and period strongly depends on the time step size, with both values decreasing as $\Delta t \to 0$ (Figure 3.9a). In contrast, little change in these predictions is observed when the presented

formulation is adopted (Figure 3.9b). The contrast between the two methods can also be observed when comparing the pressure contours in Figure 3.10. The snapshots shown in this figure are taken when the obstacle experiences a maximum lift. The dependency and lack of dependency of the conventional and present formulation on the time step size are evident in this figure.

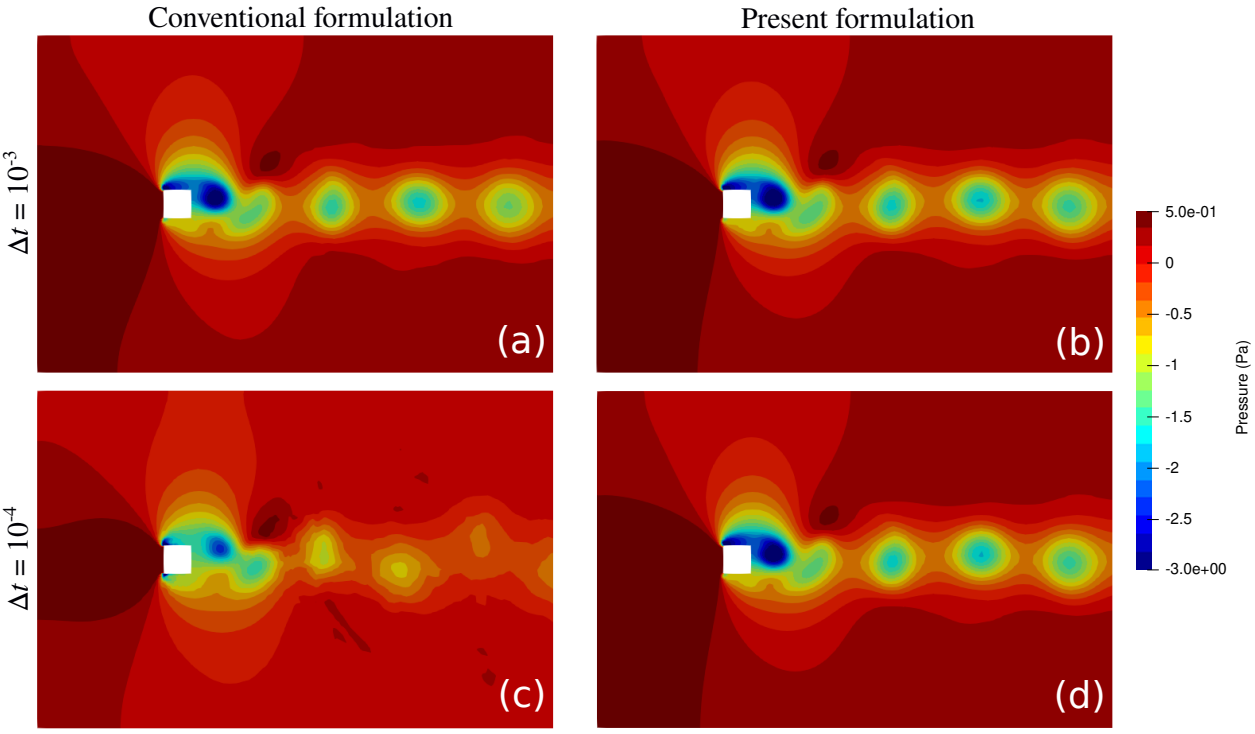

Figure 3.10: Pressure contour for the flow over a square obstacle (Figure 3.7) captured at the maximum lift. Re = 332. (a) and (c) are the results obtained from the conventional formulation while (b) and (d) are the results obtained from the present formulation. (a) and (b) are obtained using $\Delta t = 10^{-3}$ and (c) and (d) using $\Delta t = 10^{-4}$.

The results from the two formulations are compared in terms of mean drag coefficient $\overline{C_d}$, root mean square of drag coefficient fluctuation C'_d, mean lift coefficient $\overline{C_l}$, root mean square of lift coefficient fluctuation C'_l, and Strouhal number St in Table 3.1. This comparison confirms our earlier observation that the present formulation nearly eliminates the dependence of the bulk flow parameters on the time step size.

	$\overline{C_d}$	C'_d	$\overline{C_l}$	C'_l	St
Conventional					
$\Delta t = 1 \times 10^{-3}$	1.74	0.04	0.00	0.74	0.15
$\Delta t = 4 \times 10^{-4}$	1.81	0.03	−0.01	0.61	0.16
$\Delta t = 1 \times 10^{-4}$	2.07	0.01	−0.03	0.29	0.16
Present					
$\Delta t = 1 \times 10^{-3}$	1.72	0.04	−0.01	0.83	0.15
$\Delta t = 4 \times 10^{-4}$	1.72	0.04	−0.01	0.83	0.15
$\Delta t = 1 \times 10^{-4}$	1.72	0.04	−0.01	0.83	0.15

Table 3.1: Comparison of the bulk flow parameters for the flow over a square object case between the conventional and present formulations using three different time step sizes. Re = 332.

Similar to the steady pipe flow, the convergence of the solutions as the time step size decreases is tied to the convergence of ω. With the present formulation, the value of ω, although not steady, converges to periodic values around 3 regardless of Δt. The value of ω^2, which is approximately 9 s^{-2}, can be contrasted against $(2/\Delta t)^2$ that ranges from 4×10^6 to 4×10^8 s^{-2} for the simulated cases. That large change generates a significant variation in the solution as Δt is reduced in the conventional formulation.

To better see the effect of $2/\Delta t$ term on τ_{SUPG}, we have produced a snapshot of τ_{SUPG} over the entire computational domain for the two formulations in Figure 3.11 at two different time step sizes. For the conventional formulation and in particular at $\Delta t = 10^{-4}$, τ_{SUPG} is very small and approximately equal to $\Delta t/2$ over the entire domain. In the vicinity of the obstacle, where flow is the fastest, we observe some deviation from that baseline due to the contribution of the convective term in τ_{SUPG}. Nevertheless, that variation is not as significant as that of the present formulation where we see large changes in τ_{SUPG} depending on the flow velocity, mesh resolution, and flow orientation relative to the element edges.

We also simulated the present flow over a square object case at a higher Reynolds number of $22,000$ to benchmark the two formulations against previously published

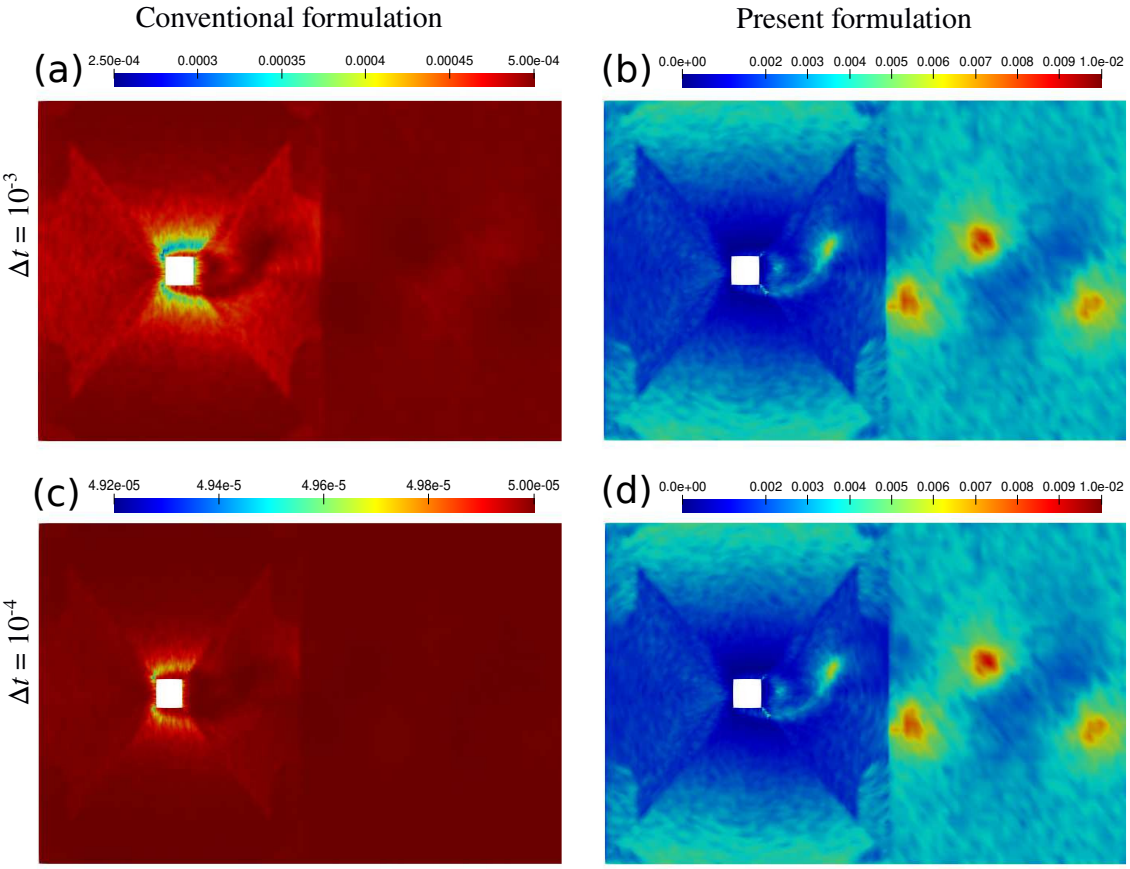

Figure 3.11: The snapshot of τ_{SUPG} obtained at peak lift for the conventional formulation (a,c) and the present formulation (b,d) with $\Delta t = 10^{-3}$ (a,b) and 10^{-4} (c,d) seconds. Re = 332. Note the range used for the color bars.

results[16, 106, 98, 146]. All simulation parameters are kept the same as in the case discussed above except for the dynamic viscosity which is reduced to 2.75×10^{-6} kg/m-s. Simulations are repeated using both formulations at $\Delta t = 5 \times 10^{-3}$ seconds. The obtained results as well as those from the literature are summarized in Table 3.2. Note that the results from the literature were obtained from three-dimensional simulations whereas our computations are performed in two dimensions. Despite such differences, we observe a relatively good agreement with the published results. That is particularly the case for the present formulation that produces predictions closer to the reported range in comparison to the conventional formulation.

	$\overline{C_d}$	C'_d	$\overline{C_l}$	C'_l	St
Conventional	1.62	0.40	−0.15	1.49	0.17
Present	1.67	0.42	−0.03	1.50	0.17
Reference[146, 16]	[1.66,2.77]	[0.10, 0.27]	[-0.09 0.03]	[0.34 1.79]	[0.07 0.15]

Table 3.2: Results for the flow over a square object at Re = 22,000 using the conventional and present formulations, and their comparison against the literature.

In order to investigate the effect of domain size for the present formulation, we extended the domain so that the overall domain size is four times that of the original domain. In doing so, we made sure that the mesh for the subset of the domain corresponding to the original mesh in Figure 3.7 remains unchanged so that the reported results are minimally affected by this change in the domain size. We repeated the original Re = 332 simulations for both formulations using $\Delta t = 10^{-3}$ with the extended domain. The results are summarized in Table 3.3. The variation in results is almost identical for the two formulations indicating that the change is more likely a result of moving the locations of the boundaries rather than the change in the value of ω. Following what we argued earlier, extending the domain reduced ω to approximately half its original value. This change, nevertheless, has a negligible effect on the overall results given that the ω term is much smaller than the sum of the other terms appearing in τ_{SUPG}.

	$\overline{C_d}$	C'_d	$\overline{C_l}$	C'_l	St
Conventional					
Original	1.74	0.04	−0.00	0.74	0.15
Extended	1.79	0.02	−0.00	0.73	0.15
Present					
Original	1.72	0.04	−0.00	0.83	0.15
Extended	1.79	0.03	−0.01	0.82	0.15

Table 3.3: Result comparison between the conventional formulation and present formulation using the original and the extended domains for the flow over a square case. $\Delta t = 10^{-3}$. Re = 332.

The relatively small value of ω, in comparison to the sum of the two other terms ap-

pearing in τ_{SUPG} in Equation (3.8), is a general feature of the present formulation rather than being unique to the case above. Evidently, it was also relatively small for the vascular model discussed earlier as the results obtained from the proposed formulation closely resembled that of the conventional formulation at large Δt (Figure 3.5), where the sum of the other two terms in τ_{SUPG} is dominant.

In general, if we only consider $\mathbf{u}^h \cdot \boldsymbol{\xi}\mathbf{u}^h$ relative to ω^2, we can show the ratio of the two scales as the square of $u/(\omega\Delta x)$. For the present method to be domain-size-dependent, that ratio must be smaller than one, implying that the flow at a node must do a full oscillation before it has the time to advect the fluid across a single element. That is an extremely fast oscillating flow, which even if occurs in reality, requires a much smaller time step to resolve, thereby indicating that the present method will do much better than the conventional method.

We should note that the linear solver convergence, which was not an issue for the previous two cases, posed a problem in this case. In general, the linear solver takes longer to converge as the time step sizes are reduced. In extreme cases, the linear solver may not converge at all. One such scenario occurs when the time step size is very small and there is a significant change in the solution between time steps, e.g., the present simulation starting from a zero velocity field. To overcome such issues, one may start a simulation with a larger time step size and then reduce it to the target value after a few time steps. Nevertheless, this convergence issue is a shortcoming of the present formulation that warrants future research.

3.3.4 Fluid-structure interaction

In this section, we will demonstrate the generalization of the present formulation to moving domain configurations using a fluid-structure interaction (FSI) test case. The chosen

case is a 2D flow over a fixed square with an attached flexible beam, which has been used in the past for verification of the FSI codes[13, 50].

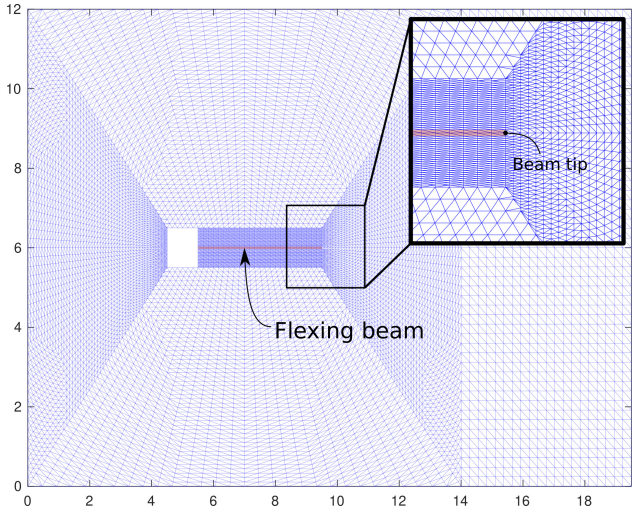

Figure 3.12: The schematic of the FSI case involving a flexible beam attached to a solid square in a cross-flow.

The specifications of the test case are shown schematically in Figure 3.12. The computation domain is 12×19.5 m. The square is 1×1 m with the center of the square placed 5 m from the inlet. The beam is 4×0.06 m centered behind the square. The fluid domain setup is identical to the previous section's flow over a square case, where the fluid density is 1.18×10^{-3} kg/m^3 and the dynamic viscosity is 1.82×10^{-4} kg/m-s with uniform inlet horizontal velocity at 51.3 m/s, resulting in Re= 332. The ω in the stabilization constant, τ_{SUPG}, is calculated in an arbitrary Eulerian-Lagrangian framework, as specified in Equation 3.10.

The solid domain is modeled as a St. Venant–Kirchhoff elastic solid[74]. The discretized weak form of the solid problem is given as

$$\mathbf{R}_m^h(\dot{\mathbf{u}}, \mathbf{d}) = \int_{\Omega_s^0} \left(\rho_s^0 \mathbf{w}^h \cdot \dot{\mathbf{u}}^h + \nabla \mathbf{w}^h : (\mathbf{F}\tilde{\mathbf{S}})^h \right) d\Omega = \mathbf{0}, \tag{3.11}$$

where

$$\tilde{\mathbf{S}} = \lambda \text{tr}(\mathbf{E})\mathbf{I} + 2\mu\mathbf{E}, \tag{3.12}$$

is the second Piola-Kirchhoff stress, in which

$$\mathbf{E} = \frac{1}{2}(\mathbf{C} - \mathbf{I}) \tag{3.13}$$

is the Green-Lagrange strain tensor, with

$$\mathbf{C} = \mathbf{F}^{\mathrm{T}}\mathbf{F} \tag{3.14}$$

as the Cauchy-Green deformation tensor, where

$$\mathbf{F} = \nabla\mathbf{d} + \mathbf{I} \tag{3.15}$$

is the deformation matrix and $\mathbf{d}$ is the displacement vector. The density of the beam at $t = 0$ is $\rho_s^0 = 0.1\mathrm{kg/m}^3$. The Young's modulus, $E = 2.5 \times 10^6$ kg/(s^{2}m), and Poisson's ratio, $\nu = 0.35$ are used to calculate Lamé parameters λ and μ in Equation 3.12 as

$$\mu = \frac{E}{2(1+\nu)}, \tag{3.16}$$

$$\lambda = \frac{E\nu}{(1+\nu)(1-2\nu)}. \tag{3.17}$$

The details of the FSI formulation are presented in a previous paper and not repeated here for brevity [50]. In summary, an arbitrary Lagrangian-Eulerian (ALE) approach and a quasi-direct FSI solution strategy are employed[189, 13, 179, 15]. The increments of the fluid and structure solution are monolithically computed. Jacobian-based stiffening is used for the elastic mesh motion without re-meshing[15, 92, 164]. A back-flow stabilization scheme is employed at the Neumann boundaries to prevent simulation divergence caused by partial flow reversal at the outlet[125].

The mesh used for all cases contains roughly 20 thousand triangular elements for the combined fluid and solid domains (Figure 3.12). The simulations were run for 10 seconds with two different time step sizes $\Delta t = 1\times10^{-3}$ and 5×10^{-4} seconds using the conventional and present formulations of τ_{SUPG}, resulting in four simulations in total.

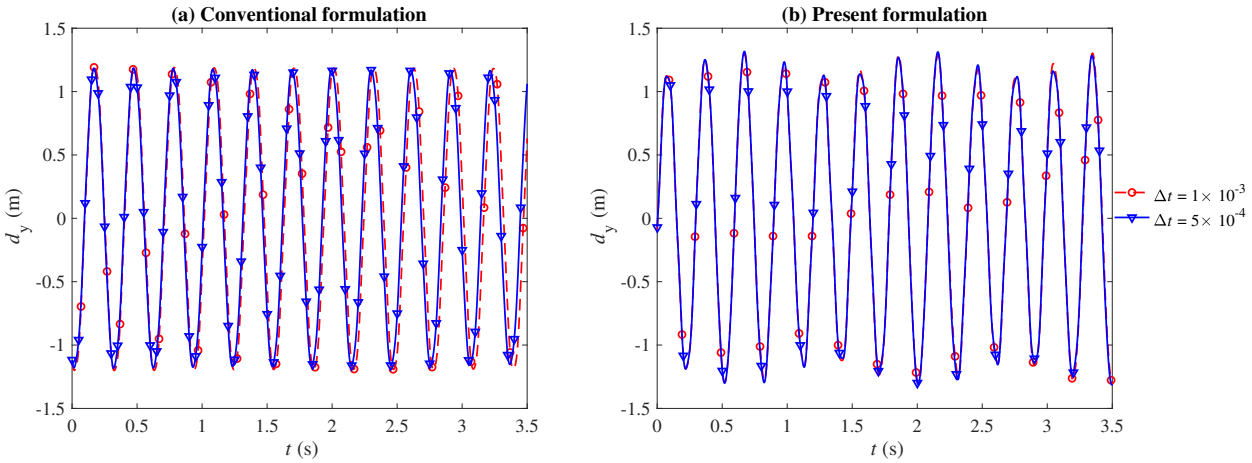

Figure 3.13: The beam tip vertical displacement, d_y, for the case shown in Figure 3.12 computed using the conventional (a; left) and present formulation (b; right). The two curves shown as a function of time for each case correspond to the simulations run with $\Delta t = 1 \times 10^{-3}$ (dashed line) and 5×10^{-4} (solid line).

Figure 3.13 shows the vertical displacement of the beam tip (marked in Figure 3.12). The conventional formulation produces an oscillation period that slightly varies as the time step size is changes by a factor of two. The change in period is approximately 0.5%, increasing from 0.305 s at $\Delta t = 5 \times 10^{-4}$ s to 0.307 s at $\Delta t = 10^{-3}$ s. On the contrary, the present formulation produced significantly closer results for both time step sizes. The predicted period, in this case, is approximately 0.299 s, which agrees well with the literature [189, 13, 50].

In terms of stability and computational cost, we observe a behavior similar to the flow over the square case from the previous section. For cases reported above, the total simulation cost of the present formulation is around 4 times that of the conventional formulation (1.3 versus 5.1 hours using 16 cores). Using a time step size smaller than $\Delta t = 5 \times 10^{-4}$ s causes linear solver convergence issues in the case of the present formulation.

3.4 Conclusion

In this study, we propose a new formulation for the stabilization parameter (τ_{SUPG}) that appears in the streamline upwind Petrov-Galerkin and pressure stabilizing Petrov-Galerkin method (SUPG/PSPG) to overcome the historical limitation of the conventional formulation that produces a large error at the small time step size. The proposed formulation uses a flow time scale instead of the time step size to account for the contribution of the acceleration term to τ_{SUPG}. Using the new formulation of τ_{SUPG}, we successfully produce an overall stable technique that is consistent with regard to the time step size. The new definition of τ_{SUPG} (Equation (3.8)) is simple to implement in existing SUPG/PSPG formulated fluid solvers. Although the present formulation comes at the cost of increasing the number of linear solver iterations, it significantly improves the overall accuracy of the stabilized finite element methods for computational fluid dynamics, making it an attractive choice for cardiovascular simulations.

CHAPTER 4

CHARACTERIZATION OF THE EJECTOR PUMP PERFORMANCE FOR THE ASSISTED BIDIRECTIONAL GLENN PROCEDURE

4.1 Introduction

Infants born with a single ventricle undergo three stages of palliation to survive, starting with the first stage performed within a few days after birth. This procedure establishes a systemic-to-pulmonary shunt, such as the modified Blalock-Taussig shunt (mBTS) [132, 133], to create a parallel circulation between the systemic and pulmonary beds. The second stage procedure, the bidirectional Glenn (BDG), is performed at around two months of age, during which the systemic-to-pulmonary shunt is removed, and the superior vena cava (SVC) is connected directly to the pulmonary arteries (PA). [66, 67] The upper body venous return through the SVC thus becomes the sole source of the pulmonary blood flow. The third stage operation, the Fontan procedure, further connects the inferior vena cava to the pulmonary arteries, after which the pulmonary and systemic circulations are then placed in series. [61, 62]

The long-term mortality rate among single-ventricle patients remains high, owing to single ventricle failure, SVC syndrome, underdeveloped or unevenly developed pulmonary arteries, and other complications resulting from the first and second stage operations. [40, 9] Despite many efforts in improving the mBTS physiology, [118, 162, 119, 192, 21, 53, 126, 120] it remains as a fundamentally flawed operation due to the unavoidable high ventricle load and the high chance of shunt occlusion due to thrombosis.

Some of the drawbacks of the mBTS are addressed at the next stage by the BDG procedure. That may motivate the total replacement of the mBTS by the BDG or an earlier transition to the BDG physiology. Historically, however, the BDG procedure can not be

used for stage-one palliation due to complications related to elevated pulmonary vascular resistance (PVR) after birth, including SVC syndrome, insufficient pulmonary flow, and low oxygen saturation. [38, 99, 193] More recent studies have explored the feasibility of performing the BDG operation at an earlier age. [86, 141] However, other studies have reported underdeveloped pulmonary arteries due to insufficient pulmonary arterial flow for patients with early BDG adaptation. [28, 69]

In order to overcome the shortcomings associated with the mBTS and the BDG, an alternative operation called the assisted bidirectional Glenn (ABG) was recently proposed that is a hybrid between those two standard operations. [51, 157, 185, 197, 60] The assisted bidirectional Glenn is based on the BDG circulation with the addition of a systemic-to-pulmonary shunt between the brachiocephalic artery (BA) and the SVC to assist the pulmonary flow. The effectiveness of the ABG circulation depends on the successful adaptation of the ejector pump effect. As it operates in industrial devices, the ejector pump uses a high energy flow as the energy source, which is jetted into a low energy flow and assists the low energy flow downstream. In the ABG circulation, the high-energy blood through the shunt would mix with the upper body return flow in the SVC, and provide the energy necessary for pulmonary circulation. Our latest study introduced a modified ABG by connecting the shunt to the SVC at the brachiocephalic veins (BV) and SVC juncture, creating a slit-shaped nozzle at that anastomosis. [90] Our multiscale simulation showed that at a pulmonary vascular resistance (PVR) of 2.3 Wood units-m^2, the modified ABG procedure increased the pulmonary flow by 76% and reduced the SVC pressure by 26% compared to the BDG while reducing the heart workload by 43% comparing to the mBTS. Other improvements were observed, including higher oxygen delivery, higher aortic oxygen saturation, and more even left and right pulmonary flow distribution.

Despite the encouraging results for the modified ABG at normal PVR, this improved circulation still poses excessively high SVC pressure when the PVR is elevated. In fact,

at a PVR of 7 Wood units-m^2, the SVC pressure was around 15 mmHg, which is 28% higher than that of the BDG. Since newborns experience episodes of high PVR, such high SVC pressure could potentially cause other complications, including cerebral ventriculomegaly, recanalization, and obliterated vessels. [36, 129, 73] The elevated SVC pressure at high PVR can be understood by two competing effects: the first is the ejector pump effect that reduces the upstream (SVC) pressure relative to the downstream (PA) pressure. The second effect results from the additional blood flow introduced by the shunt that goes through the pulmonary bed, thereby elevating the PA pressure. While the ejector pump effect at low PVR is dominant, it is overcome at higher PVR by the competing effect, leading to a higher overall SVC pressure. Therefore, at certain PVRs, the SVC pressure produced by the ABG will be higher than that of the BDG, which does not have additional flow coming from a systemic-to-pulmonary shunt.

This study aims to gain a deeper understanding of the above-mentioned competing effects and quantitatively establish the regime at which the ABG presents an advantage over the conventional procedures. Achieving this goal requires surveying at minimum a two-dimensional parameter space (i.e., different PVR and nozzle areas). Using high-fidelity computational fluid dynamic (CFD) simulations, which is the approach taken by most cardiovascular simulation studies [138, 151], for this purpose will be prohibitively expensive. To overcome this issue, a multi-fidelity approach is developed in this study, where the CFD simulations are coupled to a newly introduced algebraic model. The algebraic model is then utilized to evaluate the performance of the ABG at different PVR values while identifying the optimal design for each regime. This article is organized as the following. In Section 4.2.1 we will review the improved version of the ABG that is to be used as the baseline in this study. Then in Section 4.2.2 and 4.2.3, we will discuss our CFD framework and present the construction of the newly introduced algebraic model, respectively. We will compare the predictions of the algebraic model against the CFD results in Section 4.3.1. Our full parametric study using the algebraic model is presented

in Section 4.3.2 The physicality of the algebraic model and the clinical implication of our findings are discussed in Section 4.4.

4.2 Materials and Method

4.2.1 Modified assisted bidirectional Glenn

The most recent modifications to the ABG circulation are constructed on top of the BDG circulation where the SVC is connected to the PAs (Figure 4.1). The shunt is connected to the brachiocephalic artery on the systemic side. The pulmonary side of the shunt is connected to the BV-SVC juncture via a nozzle-shaped outlet. The nozzle profile is designed to maximize the contact area between the high-energy jet and the upper body return. This profile facilitates the mixing and momentum transfer between the two streams, thus creating the ejector pump effect successfully (Figure 4.3). In addition to improving the ejector pump effect, this nozzle design also minimizes energy loss. In this study, both the shunt diameter and the nozzle width are fixed at 3.5 mm to minimize energy loss due to the wall shear effect that can be created by the high-velocity jet impinging the SVC walls, which is 5 mm in diameter. Also, the jet from the nozzle is parallel to the SVC direction to prevent asymmetric wall impingement that also causes energy loss.

With the above parameters fixed, the only remaining parameter that determines the efficiency of the ejector pump is the nozzle thickness which directly affects the nozzle area. Therefore in this study, we will investigate the effect of nozzle areas by varying the thickness of the nozzle. The second varying parameter in this study is the PVR, which is changed in the lumped parameter network model discussed in the next section.

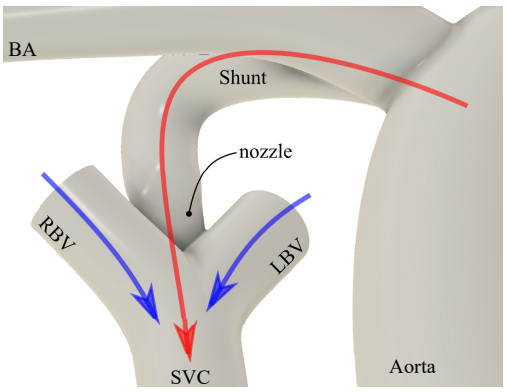

Figure 4.1: Closeup of the insertion location of the shunt in the modified ABG. BA, brachiocephalic artery; SVC, superior vena cava; LBV, left brachiocephalic vein; RBV, right brachiocephalic vein.

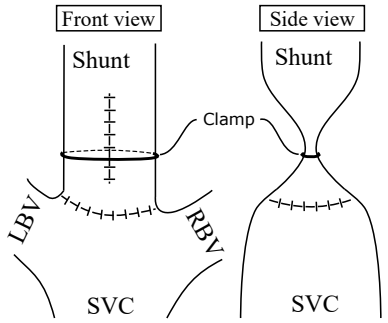

Figure 4.2: Front and side view of potential clinical implementation of the slit-shaped nozzle design. LBV and RBV are removed from the side view.

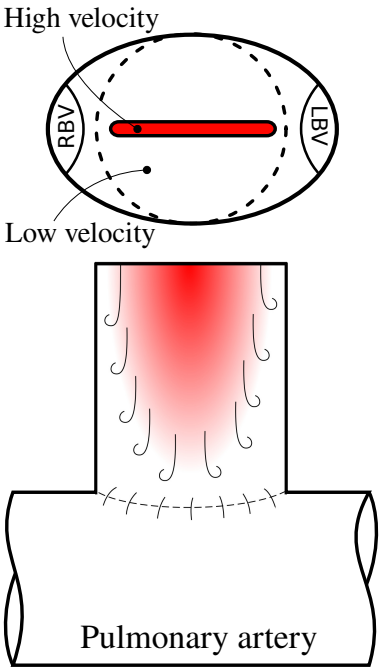

Figure 4.3: nozzle view from the SVC and mixing visualization.

4.2.2 Geometry Construction and CFD Simulation

Five 3D geometries are constructed: four variations of the modified ABG with different nozzle areas and one BDG. All five geometries are idealized representative geometries based on the modified ABG geometry from our previous study [90]. Briefly, the SVC and PA diameters are 5 mm [58] and 5.5 mm [148], respectively, and the left and right BV diameters are set to 4 mm based on Murray's law [22]. For the modified ABG geometries, the shunt is 3.5 mm in diameter, which converges to a slit-shaped nozzle at the shunt-SVC connection (Figure 4.2 and 4.3), with four different nozzle cross-sectional areas of 2.0, 2.5, 3.0, and 3.5 mm^2. For the BDG geometry, the shunt is not present, while all other dimensions are identical to the modified ABG geometries. This BDG geometry is considered a particular case of the modified ABG with zero nozzle area in our algebraic model.

A multiscale CFD framework, which is similar to the previous studies [51, 157, 185] and identical to our previous study [90], is adapted to simulate the various cases. In these simulations, the flow in major vessels (e.g., aorta, PA, SVC, etc.) is fully resolved both spatially and temporally while it is modeled for the rest of the circulatory system (e.g., the heart, lower and upper body microvasculature, etc.) using a 0D lumped parameter network (LPN), where the variables are only functions of time [127, 111].

The CFD simulations are performed using a validated in-house finite-element solver named Multi-physics finite-element solver (MUPFES) [127, 50, 49]. For the 3D simulation, incompressible Newtonian fluid and rigid walls are assumed. The underlying formulation of this solver is based on the weak form of the Navier-Stokes equation, which attempts to find $\boldsymbol{u} \in \left\{\boldsymbol{u}|\boldsymbol{u}(\boldsymbol{x},t) \in (H^1)^d \times [0,T],\ \boldsymbol{u} = \boldsymbol{g} \text{ on } \Gamma_g\right\}$ and $p \in \left\{p|p(\boldsymbol{x},t) \in L^2 \times [0,T]\right\}$ such that for all $\boldsymbol{w} \in \left\{\boldsymbol{w}|\boldsymbol{w}(\boldsymbol{x},t) \in (H^1)^d \times [0,T],\ \boldsymbol{w} = 0 \text{ on } \Gamma_g\right\}$ and $q \in \left\{q|q(\boldsymbol{x},t) \in L^2 \times [0,T]\right\}$,

$$B(\boldsymbol{w},q;\boldsymbol{u},p) = \int_\Omega \rho \boldsymbol{w} \cdot (\dot{\boldsymbol{u}} + \boldsymbol{u} \cdot \nabla \boldsymbol{u}) \mathrm{d}\Omega + \int_\Omega \nabla \boldsymbol{w} : (-p\boldsymbol{I} + \boldsymbol{T}) \mathrm{d}\Omega - \int_\Omega \nabla q \cdot \boldsymbol{u} \mathrm{d}\Omega$$

$$+\int_{\Gamma} q\boldsymbol{u}\cdot\boldsymbol{n}\mathrm{d}\Gamma-\int_{\Gamma_h}\boldsymbol{w}\cdot\boldsymbol{h}\mathrm{d}\Gamma-\beta\int_{\Gamma_h}\rho\boldsymbol{w}\cdot\boldsymbol{u}(\boldsymbol{u}\cdot\boldsymbol{n})_{-}\mathrm{d}\Gamma=0, \tag{4.1}$$

is satisfied. In Equation 4.1, ρ, $\dot{\boldsymbol{u}}$, $\boldsymbol{u}$, p, $\boldsymbol{T}$, $\boldsymbol{h}$, $\boldsymbol{n}$, $\boldsymbol{w}$, and q are the density, acceleration, velocity vector, pressure, viscous stress tensor, Neumann boundary traction, boundary outward normal vector, velocity and pressure test functions, respectively. The Neumann and Dirichlet boundaries are denoted by Γ_h and Γ_g, respectively, and the 3D fluid domain is denoted by Ω. β is a positive coefficient between 0.0 and 0.5 and set to 0.2 in our computations, and $(\boldsymbol{u}\cdot\boldsymbol{n})_{-}$ is defined as,

$$(\boldsymbol{u}\cdot\boldsymbol{n})_{-}\equiv\frac{\boldsymbol{u}\cdot\boldsymbol{n}-|\boldsymbol{u}\cdot\boldsymbol{n}|}{2} \tag{4.2}$$

[126]. The last term in Equation 4.1 is a minimally intrusive backflow stabilization term used to avoid simulation divergence due to partial or bulk backflow on the Neumann boundaries [125]. Provided that the Galerkin's form in Equation 4.1 does not meet LBB condition for identical shape functions for velocity and pressure, the actual formulation implemented in our solver is based on the RBVMS (residual-based variational multiscale) formulation and includes additional terms to ensure the stability of the solution even at highly convective regimes [23, 11]. A specialized iterative algorithm, preconditioner, and parallelization strategy are employed for an efficient and scalable solution of the linear system of equations that arises from the discretization of the RBVMS formulation [49, 50, 47]. The numerical method used in this study can capture the chaotic nature of the flow, which includes the turbulent jet created downstream of the nozzle (Figure 4.7). The Reynolds number in the other vessels, including ascending aorta is less than 1000 and thus the flow remains transitional.

The 0D LPN model, which consists of five blocks to model upper body, lower body, pulmonary bed, coronary circulation, and heart, is also identical to our previous study [90], where the component values are taken from a modeling study of 28 Norwood-procedure patients [120]. The schematic for the LPN system of the ABG is presented in Figure 4.4. The numerical implementation of the LPN is described in our previous

study. [127]. The LPN values and calculations related to the heart model are included in Appendix A. PVR of 2.3, 4.7, and 7 Wood units-m^2 are simulated for all five models, representing normal, slightly elevated, and high PVR values in an infant. [51]. The two higher PVR values are simulated to account for patient-to-patient variability, PVR change with age, and uncertainties in the clinical measurements. To mimic the long-term effect of the auto-regulatory system, we used the blood volume control system that regulates the average aortic pressure at an average of 67 mmHg. [90]

The boundary conditions at the 3D-0D interface are not prescribed but obtained by solving the lumped parameter network. [49] For the coupled Neumann boundary conditions, the CFD solver will send the flow rate and receive the pressure in exchange from the LPN. The process is similar for coupled Dirichlet boundary condition with the difference that the pressure is sent and flow is received from the LPN. The ascending aorta, LBV, and RBV are coupled Dirichlet boundaries, where we impose a parabolic profile. The remaining boundaries are coupled Neumann boundaries. The initial conditions for the LPN are taken from prior studies. The final results do not depend on those initial conditions.

Blood density is 1060 kg/m^3 and viscosity is 0.004 Pa-s. We treated the blood as a Newtonian fluid because the shear rates in our simulation are outside of the range that produces non-Newtonian effects. [42] All geometries are meshed using tetrahedral elements and an adaptive mesh refinement algorithm to improve accuracy (Figure 4.5). Our mesh refinement algorithm is detailed in our previous study [90]. A rigorous convergence study was performed to ensure results are independent of the mesh size, the linear solver tolerance, and the number of Newton-Raphson iterations. On average, the mesh geometries contain 2 million elements after 6 iterations of adaptive mesh refinement, resulting in an accuracy that is comparable to that of a 10 million elements uniform mesh. We used a time step size of 10^{-4} second for the simulations. Each simulation is continued for 10

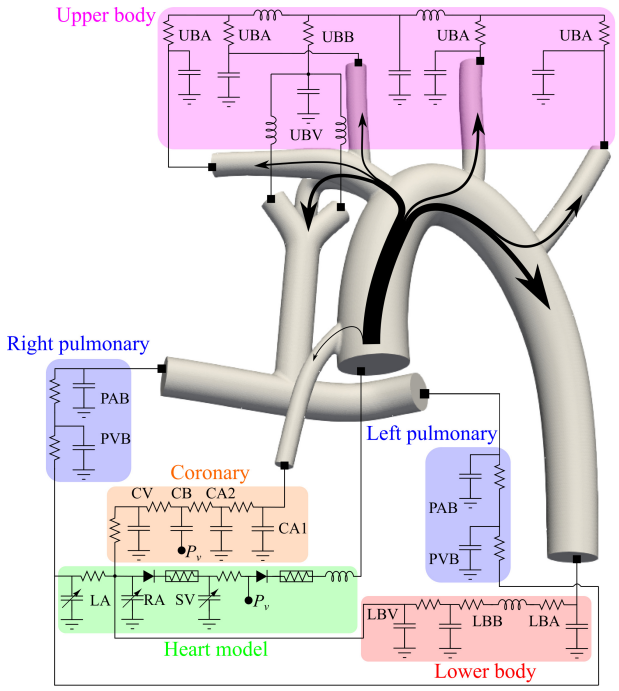

Figure 4.4: Lumped parameter network coupled with physical domain geometry for the ABG procedure. See Appendix A for details.

seconds corresponding to 20 cardiac cycles. This number of cycles is selected to ensure both mean value and cycle-to-cycle convergence. This convergence is clearly shown in Figure 4.8 for the case with 2.0 mm^2 nozzle area and PVR value of 7.0 Wood units-m^2. The SVC pressure is observed to be the last parameter to converge in our simulations. Therefore, as long as the SVC converges, the simulation is considered converged in our study. The simulation results are calculated from the last cardiac cycle in every case. A typical simulation takes around 40 physical hours with 224 processors, or around 9000 computational hours, at a 2.4 GHz clock rate. In total, fifteen simulations were performed for five geometries at three different PVR values.

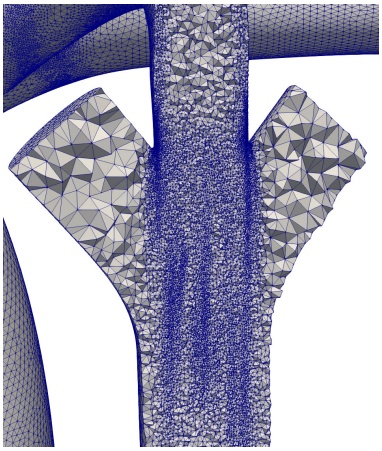

Figure 4.5: Tetrahedral mesh cross section at the shunt-SVC junction for the ABG simulation with a nozzle size of 3 mm^2 and PVR of 4.7 Wood units-m^2 at end systole.

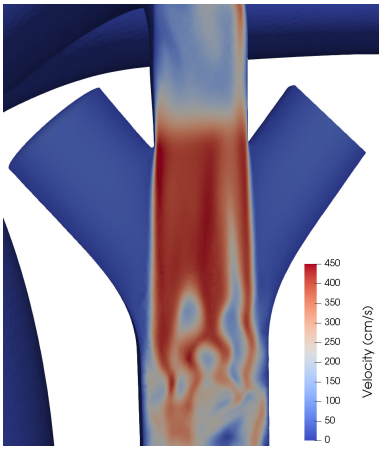

Figure 4.6: Velocity field at the shunt-SVC junction for the ABG simulation with a nozzle size of 3 mm^2 and PVR of 4.7 Wood units-m^2 at end systole.

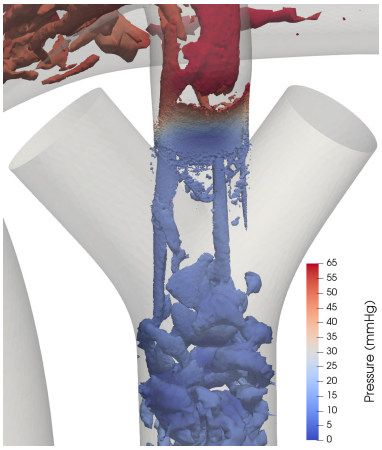

Figure 4.7: Q-criterion contour at the shunt-SVC junction for the ABG simulation with a nozzle size of 3 mm^2 and PVR of 4.7 Wood units-m^2 at end systole.

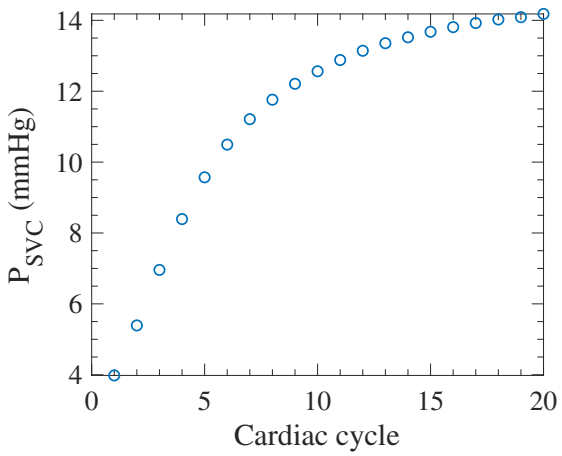

Figure 4.8: Mean SVC pressure over one cardiac cycle as the simulation progresses for 2.0 mm^2 nozzle area and 7.0 Wood units-m^2 PVR.

4.2.3 Algebraic Model

Each of the simulations described in the previous section takes ≈7 days to run on a cluster when utilizing 192 processors at a 2.4 GHz clock rate. Due to this high cost, it is infeasible to evaluate the full range of nozzle areas and PVRs using multiscale CFD simulations. To overcome this issue, we developed a multi-fidelity approach that utilizes the CFD simulations to tune an algebraic model, which in turn is used to predict the performance of the ABG circulation over a wide range of nozzle areas, A_{nozzle}, and PVR values, R_{PVR}. The construction and parameter tuning of the algebraic model is discussed in the following sections.

Model Construction

The assumptions of this algebraic model (schematically shown in Figure 4.9), which replaces the 3D model, are incompressible, inviscid, steady, and unidirectional flow. The viscous effect is incorporated in this model using loss terms tuned based on the CFD results. The model only includes the shunt, the BV-SVC juncture, the SVC, and the pulmonary branches. The reason for such choice is that the aortic flow and lower body circu-

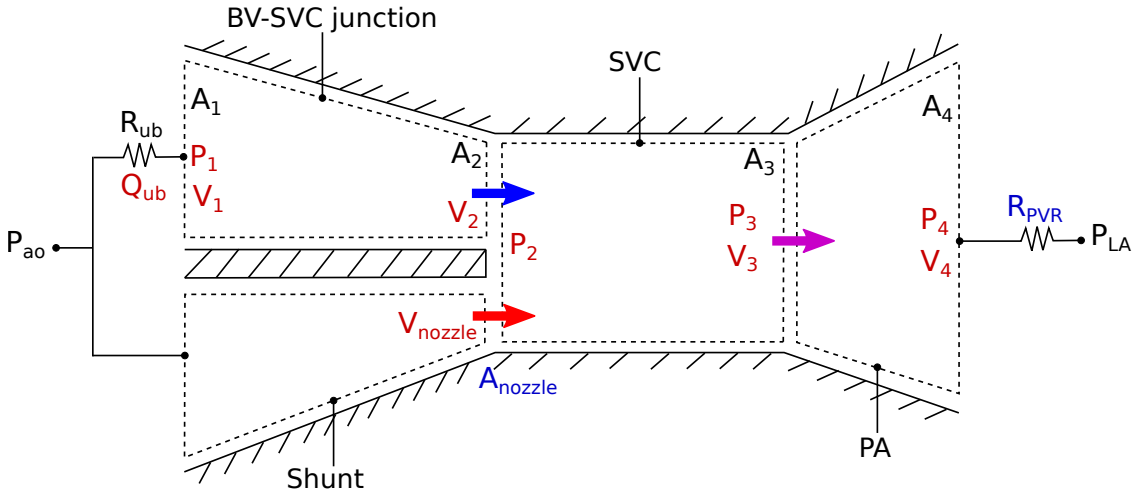

Figure 4.9: Schematic of the algebraic model for modeling the ABG circulation. Variables shown in black, red, and blue are known, unknown, and independent parameters, respectively. Note that the 2D representation of this schematic is only for demonstrating the control volumes. The algebraic model is a 0D model that does not capture variation in time or space.

lation are minimally affected by the nozzle geometry or the PVR values, as confirmed by the CFD simulation results in Section 4.3.1. The dimensional constants of cross-sectional areas are consistent with the dimensions of the CFD geometries. The aortic pressure, P_{ao}, and the left atrial pressure, P_{LA}, are held fixed at 67.0 and 2.1 mmHg, respectively, which are identical to the CFD simulation and based on the clinical measurements [120].

The upper body section is modeled using two equations: one for the upper body circulation and the other for the flow in the BV-SVC juncture. The upper body circulation is modeled using

$$P_{\text{ao}} - P_1 = R_{\text{ub}} Q_{ub}, \tag{4.3}$$

where the total upper body flow rate, Q_{ub}, and the bottom BV pressure, P_1, are the unknown variables. The upper body resistance, $R_{\text{ub}} = 140.9$ mmHg-min/L, is a constant obtained from the LPN used for the CFD simulations. The flow through the BV-SVC juncture is modeled while neglecting losses using the Bernoulli's equation

$$P_1 + \frac{1}{2}\rho {V_1}^2 = P_2 + \frac{1}{2}\rho {V_2}^2, \tag{4.4}$$

where P_2 is the upper SVC pressure. The upper body return velocity, V_1, and the upper SVC velocity, V_2, are defined using mass conservation as

$$Q_{ub} = A_1 V_1 = A_2 V_2. \tag{4.5}$$

Based on the 3D geometry, the total cross-sectional area of both BVs, A_1, is 0.248 cm^2, the SVC corss-sectional area, A_3, is 0.196 cm^2, and the nozzle area, A_{nozzle}, is an independent variable. The effective area of the upper SVC, A_2, is calculated as

$$A_2 = A_3 - A_{\text{nozzle}}. \tag{4.6}$$

Accounting for losses in the shunt, the shunt upstream and downstream conditions can be related via

$$P_{ao} = P_2 + \frac{1}{2}\rho {V_{\text{nozzle}}}^2 + C_s \rho {V_{\text{nozzle}}}^2, \tag{4.7}$$

where the pressure, P_2, and nozzle velocity, V_{nozzle}, are unknown. Due to the high velocity in the shunt, especially at the nozzle, a head loss constant, C_s, is added to the equation to account for the viscous dissipation in the shunt that is similar in form to the Darcy–Weisbach equation. The value of C_s is to be calculated through a tuning process from the CFD simulation results as discussed in Section 4.2.3. The modeling of these two streams inherently assumes that the mixing does not happen in the BV-SVC junction, which is the case demonstrated by CFD results.

The flow in the SVC is modeled by the mass conservation equation between the inlets and outlet

$$Q_{\text{ub}} + A_{\text{nozzle}} V_{\text{nozzle}} = A_3 V_3, \tag{4.8}$$

where V_3 is the fluid velocity at the bottom of the SVC, and the conservation of momentum equation

$$\rho A_2 {V_2}^2 + \rho A_{\text{nozzle}} {V_{\text{nozzle}}}^2 + (A_2 + A_{\text{nozzle}}) P_2 = \rho A_3 {V_3}^2 + A_3 P_3, \tag{4.9}$$

where the bottom SVC pressure, P_3, is unknown.

Three equations model the PA section: a Bernoulli's equation with a head loss constant, C_p, which will be calculated from the CFD results (Equation 4.10), a conservation of mass equation (Equation 4.11), and a pressure-flow rate relation for the pulmonary bed (Equation 4.12).

$$P_3 + \frac{1}{2}\rho {V_3}^2 = P_4 + \frac{1}{2}\rho {V_4}^2 + C_\mathrm{p}\rho {V_4}^2, \tag{4.10}$$

$$Q_\mathrm{p} = A_3 V_3 = A_4 V_4 \tag{4.11}$$

$$P_4 - P_\mathrm{LA} = R_\mathrm{PVR} Q_\mathrm{p}, \tag{4.12}$$

From the 3D geometries, the total cross-sectional area of the PAs, A_4, is 0.475 cm^2. The PA pressure, P_4, and PA velocity, V_4 are two unknowns, and Q_p is the pulmonary flow rate. The PVR value, R_PVR, is the other independent variable in this model.

In total, there are ten equations with ten unknowns (marked in red in Figure 4.9) and two independent variables. The calculation for the head loss constants C_s and C_p is detailed in the next section. Other parameters can be calculated from the unknowns solved from this system of equations. The total cardiac output, CO, is calculated as

$$CO = Q_\mathrm{p} + Q_\mathrm{lb}, \tag{4.13}$$

where the lower body flow, Q_lb, rate is held constant at 0.56 L/min, taken from the simulation results. The systemic flow rate, Q_s is calculated as

$$Q_\mathrm{s} = Q_\mathrm{ub} + Q_\mathrm{lb}. \tag{4.14}$$

The oxygen delivery, OD, and aortic oxygen saturation Sat_ao can be further calculated by

$$OD = Q_\mathrm{s} C_\mathrm{op} - r\frac{Q_\mathrm{s}}{Q_\mathrm{p}} V_{\mathrm{O}_2}, \tag{4.15}$$

and

$$Sat_\mathrm{ao} = \frac{OD/Q_\mathrm{s}}{0.98 C_\mathrm{op}}, \tag{4.16}$$

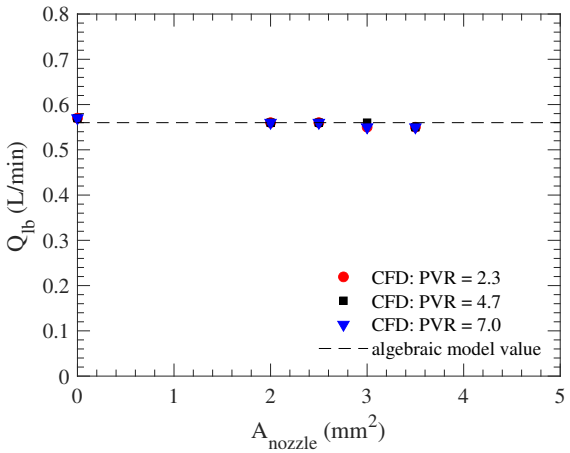

Figure 4.10: Lower body average flow rate, Q_{lb}, obtained from CFD simulations with PVRs of 2.3 (red circle), 4.7 (black square), and 7.0 (blue triangle) Wood units-m^2. Some data points are not clearly visible since they are overlapping. The dotted line is the constant lower body flow rate assumed in the algebraic model.

where C_{op} is the the oxygen concentration in the pulmonary vein, V_{O_2} is the total body oxygen consumption, and assuming half of the total oxygen is consumed by the upper body, i.e., $r = 0.5$. [51]

Parameter Identification

Using the CFD results, we can first verify our earlier assumption that changing the nozzle area or PVR has a negligible effect on the hemodynamics outside the algebraic model. Comparing lower body flow rate of all 15 CFD simulations for this purpose shows its minimal change from 0.56 L/min, thereby confirming our earlier assumption (Figure 4.10).

C_{s} and C_{p} are computed through an optimization procedure. Three parameters from the CFD simulation results are used as target values in the calculations: the mean SVC pressure, $P^{\text{s}}_{\text{SVC}}$, the mean PA pressure, P^{s}_{PA}, and the mean pulmonary flow rate, Q^{s}_{p}. The optimization problem is stated as minimizing the error function

$$e(\mathbf{C}) = \sum_{A_{\text{nozzle}}} \sum_{R_{\text{PVR}}} [(\frac{P_1(\mathbf{C}) - P^{\text{s}}_{\text{SVC}}}{P^{\text{s}}_{\text{SVC}}})^2 + (\frac{P_4(\mathbf{C}) - P^{\text{s}}_{\text{PA}}}{P^{\text{s}}_{\text{PA}}})^2 + (\frac{Q_p(\mathbf{C}) - Q^{\text{s}}_{\text{p}}}{Q^{\text{s}}_{\text{p}}})^2], \tag{4.17}$$

with respect to $\mathbf{C} = \{C_s, C_p\}$.

To find the minimum of the error function, we used a gradient-based iterative approach that is implemented as *fmincon* in MATLAB [112]. The minimum of the function, $e(\mathbf{C})$, is computed such that $\mathbf{C_l} < \mathbf{C} < \mathbf{C_u}$, where the lower bound is $\mathbf{C_l} = \{0, 0\}$ and the upper bound is $\mathbf{C_u} = \{100, 100\}$. The initial value is $\mathbf{C_0} = \{0, 0\}$. The function took 11 iterations to converge to $C_s = 0.313$ and $C_p = 0.830$, producing $e = 0.093$.

4.3 Results

4.3.1 CFD and algebraic model comparison

With the constant values calculated, remaining unknowns in the algebraic model can be calculated and compared against the CFD results. Figures 4.11, 4.12, and 4.13 shows the behavior of three parameters that are most critical to the effectiveness of the ABG circulation, namely the mean pulmonary flow rate, Q_p, the mean SVC pressure, P_{SVC}, and the mean PA pressure, P_{PA}, which are the same parameters used to calculate the constants in the algebraic model. In the figures of this section, the lines are the results from the algebraic model, and the data points are the CFD results. The BDG is represented by the zero nozzle area in these plots.

There is a good overall agreement between the algebraic model and the CFD results. Figure 4.11 shows that the pulmonary arterial pressure at a given PVR increases almost linearly with the nozzle area. This correlation is caused by the pulmonary flow increasing monotonically as the nozzle area increase (Figure 4.13), as the mean velocity at the nozzle is almost constant. Since the PVR is held constant as an independent variable in our models, the pulmonary arterial pressure is linearly proportional to the pulmonary

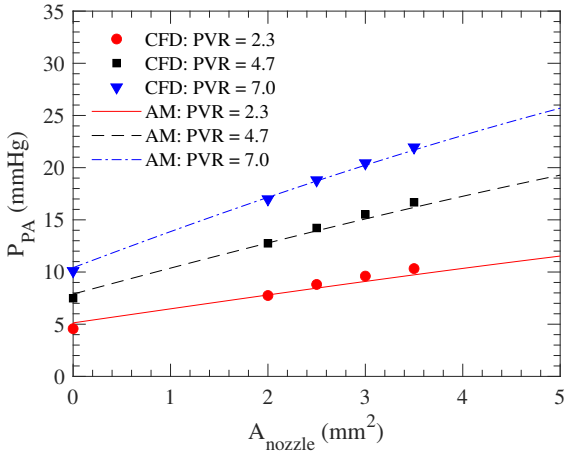

Figure 4.11: The mean pulmonary artery pressure, P_{PA}, as a function of the nozzle area, A_{nozzle}, at different PVR values. Lines correspond to the algebraic model (AM) and symbols to the CFD.

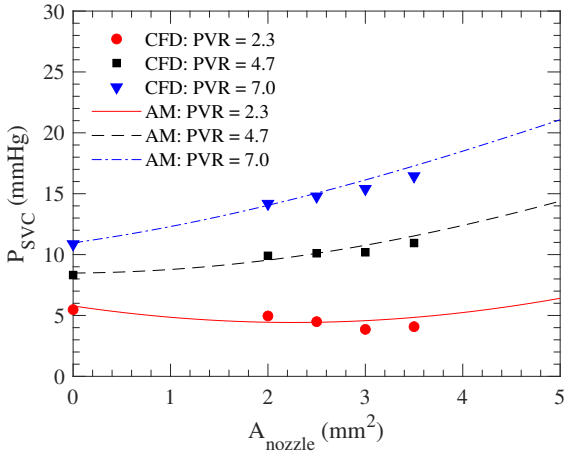

Figure 4.12: The mean SVC pressure, P_{SVC}, as a function of the nozzle area, A_{nozzle}, at different PVR values. Lines correspond to the algebraic model (AM) and symbols to the CFD.

flow rate, thus creating a linear relationship between the nozzle area and the pulmonary arterial pressure. In practice, the pulmonary arterial pressure might plateau when the nozzle area increases beyond a certain value since studies show that the PVR drops as the pulmonary arterial pressure increases. [101, 113] Also, as expected, the rate at which the pulmonary arterial pressure increases with the nozzle area, as well as its absolute value, increases with the PVR.

The SVC pressure, P_{SVC}, initially decreases as the nozzle area increases owing to the

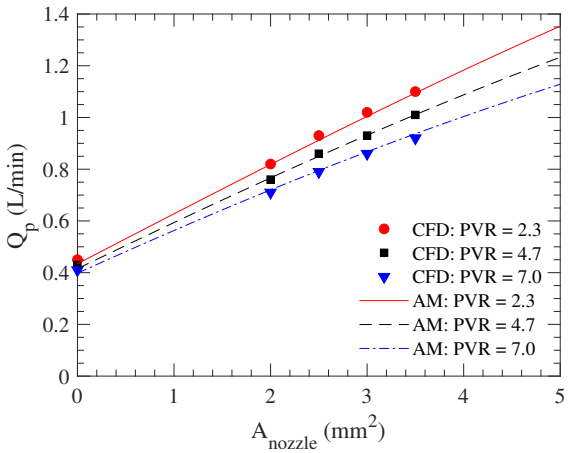

Figure 4.13: The pulmonary average flow rate, Q_p, as a function of the nozzle area, A_{nozzle}, at different PVR values. Lines correspond to the algebraic model (AM) and symbols to the CFD.

ejector pump effect. However, at sufficiently large nozzle areas or PVRs, it increases as the increase in P_{PA} beyond that of the BDG (corresponding to a zero nozzle area) as the increase in the pulmonary arterial pressure cannot be compensated by the ejector pump effect. For higher PVRs, any additional flow from the shunt is non-beneficial to the lowering SVC pressure. The exact cut-off value of the PVR for such adverse effect is presented in Section 4.3.2.

Other parameters calculated from the algebraic model also show good agreement with the CFD results (Figure 4.13, 4.14, 4.15, and 4.16). The systemic flow rate, Q_s, remains relatively constant as it is a function of aortic and venous pressures and systemic vascular resistance, which do not depend on the nozzle area. The cardiac output, CO, and pulmonary-to-systemic flow ratio, Q_p/Q_s, both linearly increase with the nozzle area, which is the direct consequences of the systemic flow rate being constant and the pulmonary flow rate linearly increasing with the nozzle area. These three parameters are relatively insensitive to the PVR, especially at smaller nozzle areas.

Figure 4.17 and 4.18 shows the oxygen delivery, OD, and systemic oxygen saturation obtained from the CFD simulation and the algebraic model. These parameters show rapid

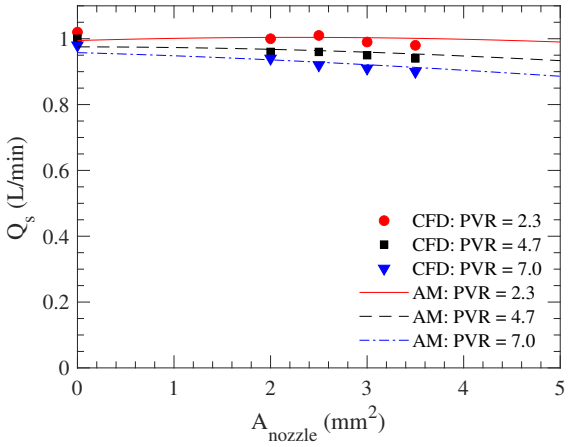

Figure 4.14: The average systemic flow rate, Q_s, as a function of the nozzle area, A_{nozzle}, at different PVR values. Lines correspond to the algebraic model (AM) and symbols to the CFD.

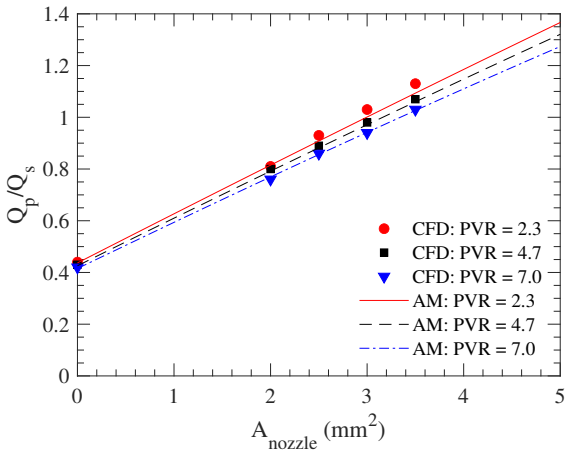

Figure 4.15: The pulmonary-to-systemic flow ratio, Q_p/Q_s, as a function of the nozzle area, A_{nozzle}, at different PVR values. Lines correspond to the algebraic model (AM) and symbols to the CFD.

growths at small nozzle areas up to approximately 2 mm^2. Increasing the nozzle area beyond 2 mm^2 has a smaller effect on oxygen delivery and saturation as the increase in the pulmonary flow is countered by a drop in systemic flow rate owing to the shunt flow.

The effectiveness of the ejector pump effect can be further demonstrated with two additional parameters: the pressure recovery, ΔP_{EP}, and the ejector pump efficiency, η_{EP}. The pressure recovery is calculated as the difference in pressure between the downstream and upstream of the ejector pump, which are the PA pressure and the SVC pressure, respec-

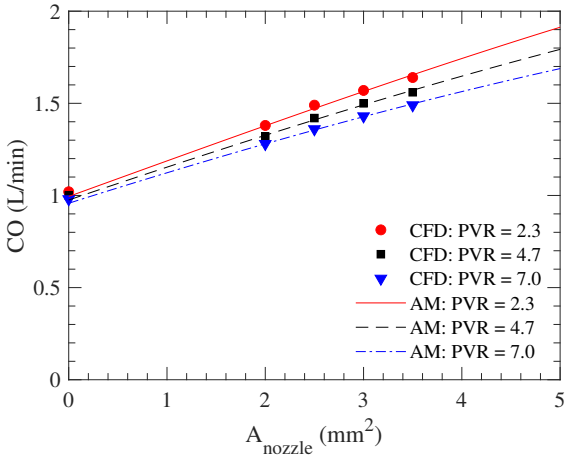

Figure 4.16: The average cardiac output, CO, as a function of the nozzle area, A_{nozzle}, at different PVR values. Lines correspond to the algebraic model (AM) and symbols to the CFD.

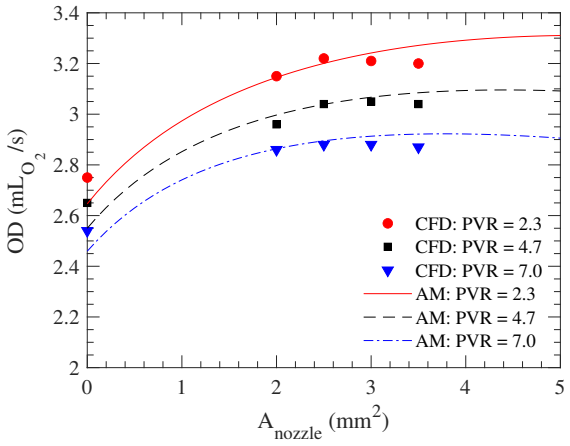

Figure 4.17: The oxygen delivery, OD, as a function of the nozzle area, A_{nozzle}, at different PVR values. Lines correspond to the algebraic model (AM) and symbols to the CFD.

tively. As shown in Figure 4.19, the pressure recovery is almost independent of the PVR according to both the CFD and algebraic model. It increases linearly with the nozzle area up to a certain value, around 3 mm^2 for the CFD result and 2 mm^2 for the algebraic model. The pressure recovery then plateaus before trending slightly downwards at large nozzle areas. The ejector pump efficiency is calculated as the ratio between the actual pressure recovery and the pressure recovery when the losses associated with C_s and C_p terms are removed from the model. Figure 4.20 shows that there is an optimal nozzle area for the ejector pump efficiently. For very small nozzle areas, the nozzle flow dissipates its energy

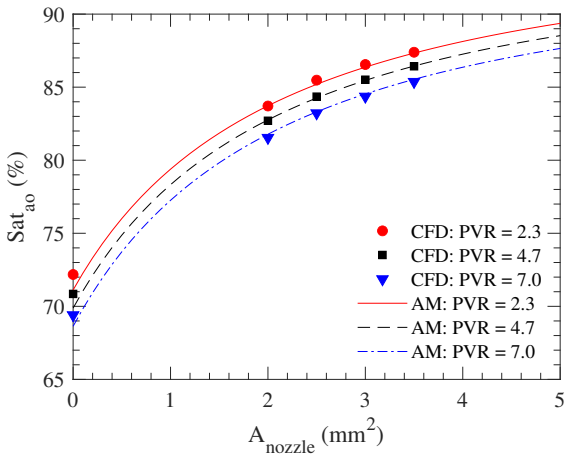

Figure 4.18: The aortic oxygen saturation, Sat_{ao}, as a function of the nozzle area, A_{nozzle}, at different PVR values. Lines correspond to the algebraic model (AM) and symbols to the CFD.

before transferring it to the SVC flow. On the other hand, for very large nozzles, the SVC length is too short for the two streams to mix sufficiently. As a result, the jet created by the nozzle impinges the PA, losing its energy and lowering the ejector pump efficiency. The efficiency metric is very sensitive to the dynamics of the flow in the ejector pump and the approach in modeling the losses. The algebraic model only accounts for the losses that are proportional to the velocity square. Linear losses are excluded in the algebraic model to prevent over-fitting. In reality, some losses may scale linearly rather than quadratically with the flow, such as Poiseuille's law at low Reynolds number. These simplifications likely cause those disagreements between the CFD and the algebraic model predictions.

The overall agreement between the CFD and the algebraic model indicates the relative accuracy of the algebraic model in characterizing the ABG circulation and predicting its hydrodynamic response for different nozzle areas and PVRs.

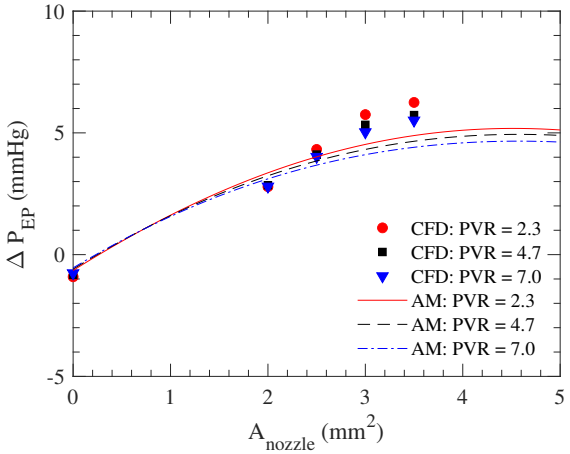

Figure 4.19: The pressure recovery, ΔP_{EP}, as a function of nozzle area, A_{nozzle}, at different PVR values. Lines correspond to the algebraic model (AM) and symbols to the CFD.

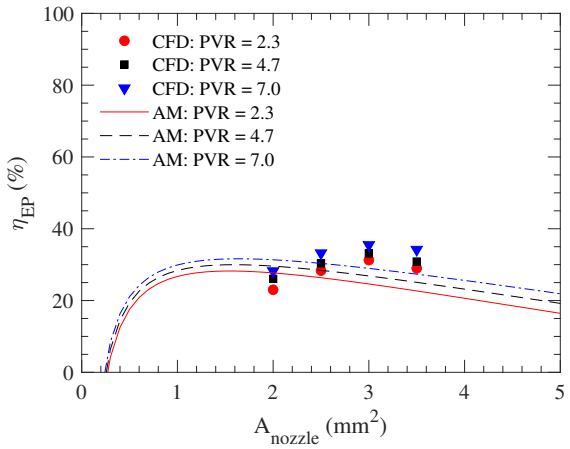

Figure 4.20: The ejector pump efficiency, η_{EP}, as a function of nozzle area, A_{nozzle}, at different PVR values. Lines correspond to the algebraic model (AM) and symbols to the CFD.

4.3.2 Algebraic model predictions

With the algebraic model, we can further analyze where the losses are occurring in the ejector pump. The shunt and PA losses are calculated using the loss terms in Equation 4.7 and 4.10 whereas the SVC loss is inherent due to the momentum balance formulation of the SVC mixing in the algebraic model. The loss in the SVC is calculated from the energy difference between the inlets and the outlet of the SVC. Thus, while other losses can be avoided by improving the design of the ejector pump, the SVC mixing loss is unavoidable as it is inherent to the ejector pump function. As shown in Figure 4.21 and 4.24,

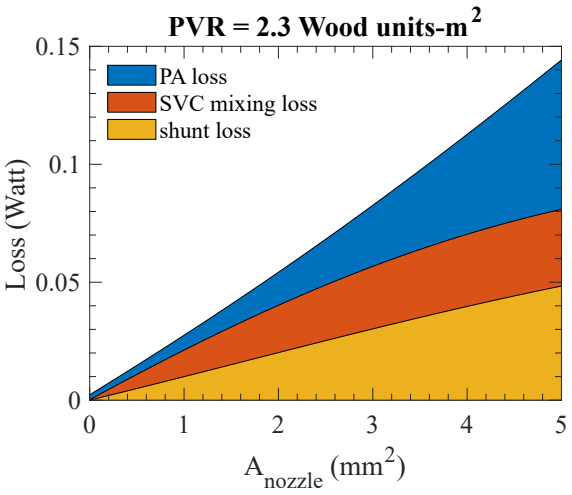

Figure 4.21: The locations where energy losses occur in the ABG circulation at normal PVR. These results are obtained from the algebraic model.

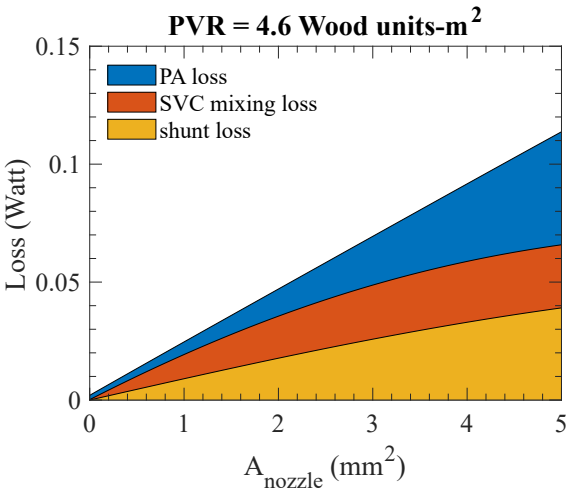

Figure 4.22: The locations where energy losses occur in the ABG circulation at elevated PVR. These results are obtained from the algebraic model.

the energy loss mostly occurs in the shunt and through the mixing inside the SVC at a smaller nozzle area. As the nozzle area increases, the loss inside the PA becomes more dominant. Although the energy loss due to the mixing inside the SVC is required for the proper functioning of the ejector pump, the significant energy loss in the shunt and the PA indicates there is still room for improvement by identifying a more optimal design.

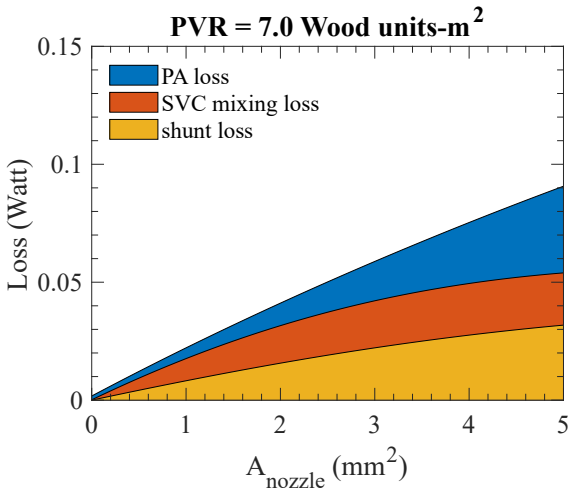

Figure 4.23: The locations where energy losses occur in the ABG circulation at high PVR. These results are obtained from the algebraic model.

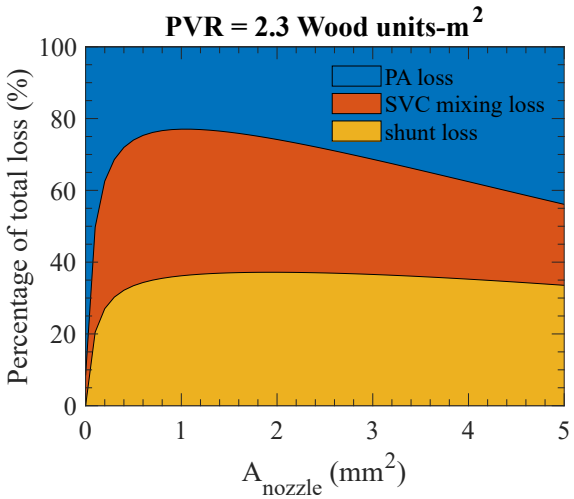

Figure 4.24: Same results as Figure 4.21, namely, losses in the ABG circulation, but on a relative scale.

Figure 4.27 to 4.30 present the 2D survey of the ABG circulation performance for any given nozzle area and PVR. The pulmonary arterial pressure (Figure 4.27) monotonically increases with the PVR and nozzle area since a higher PVR imposes higher resistance against pulmonary perfusion and a larger nozzle area increases the pulmonary perfusion, as described mathematically in Equation 4.12. The ejector pump pressure recovery (Figure 4.28) is almost independent of PVR while monotonically increasing with the noz-

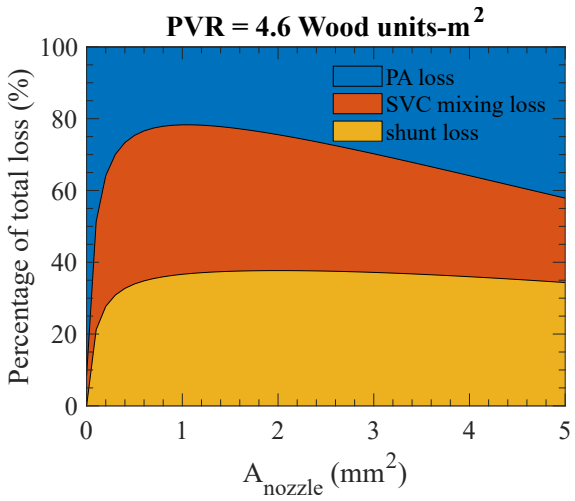

Figure 4.25: Same results as Figure 4.22, namely, losses in the ABG circulation, but on a relative scale.

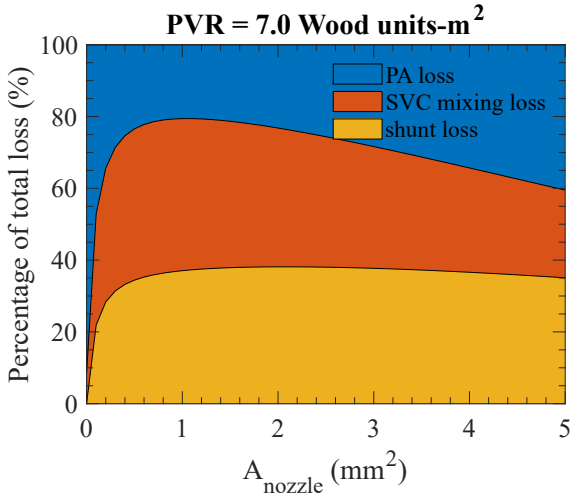

Figure 4.26: Same results as Figure 4.23, namely, losses in the ABG circulation, but on a relative scale.

zle area. A larger nozzle provides more energy for pumping the flow, thereby increasing the overall pumping pressure of the ejector pump. This correlation nonetheless breaks down at a large nozzle area owing to the finite SVC flow and the increase in losses at higher shunt flow (Figure 4.29).

The change in the SVC pressure, which is a result of a competition between the change in the PA pressure and the ejector pump pressure recovery, has a more complex behavior (Figure 4.29). For normal to slightly elevated PVR, that competition leads to an SVC pres-

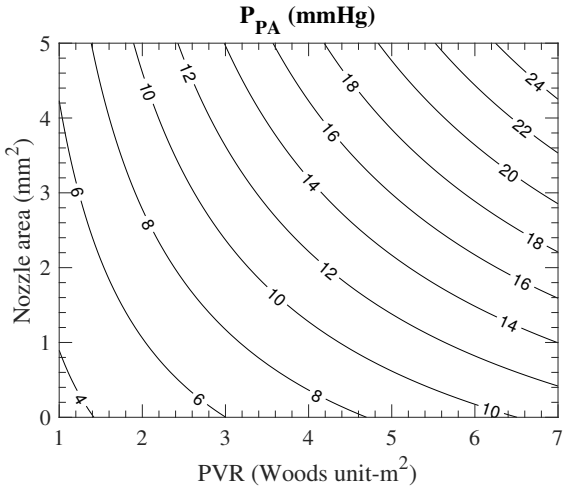

Figure 4.27: The PA pressure as functions of the nozzle area and the PVR. These results are obtained from the algebraic model.

sure that first decreases then increases as the nozzle area increases. This non-monotonic variation creates an optimal nozzle area (shown with a dashed line in Figure 4.29) that yields the lowest SVC pressure. For PVR greater than 4.4 Wood units-m^2, however, the inclusion of the systemic-to-pulmonary shunt will only have an adverse effect on the SVC pressure. This monotonic variation can be explained by the fact that the rate at which the pulmonary arterial pressure increases with the nozzle area is faster than that of the ejector pump pressure recovery.

The ejector pump efficiency (Figure 4.30) depends on the amount of energy extracted from the shunt flow to elevate the ejector pump pressure recovery. The efficiency shows a strong dependence on the nozzle area while weakly varying with the PVR. Its variation with the nozzle area is non-monotonic, reaching a peak at an intermediate nozzle size, around 1.6 mm^2. As explained earlier, lower efficiency at small and large nozzle areas can be attributed to the significant losses in the PA through different mechanisms. One must note that the maximum efficiency of the ejector pump does not necessarily coincide with the maximum pressure recovery or minimum SVC pressure, as each of these parameters depends on a range of other parameters, including the pulmonary arterial pressure.

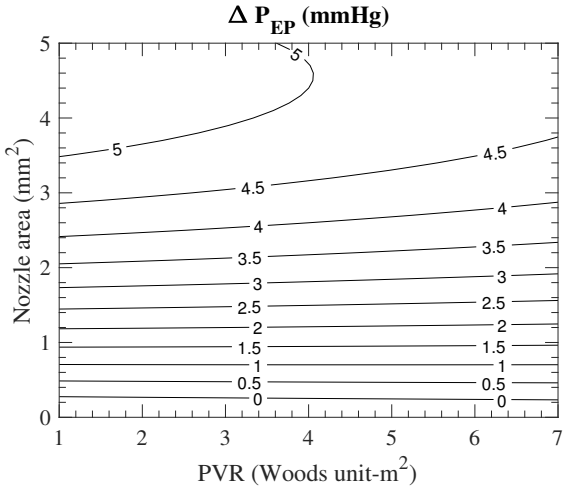

Figure 4.28: The ejector pump pressure recovery as functions of the nozzle area and the PVR. These results are obtained from the algebraic model.

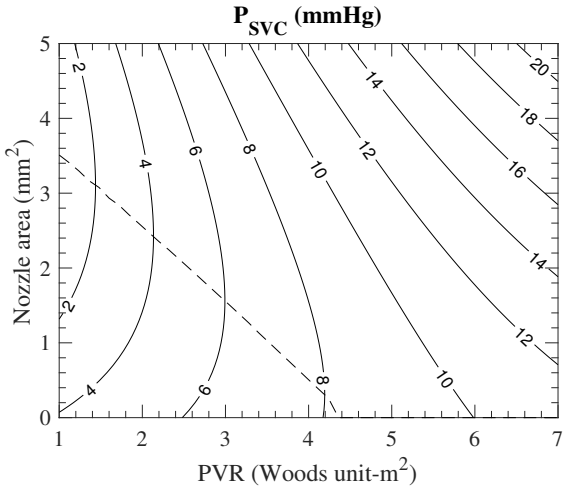

Figure 4.29: The SVC pressure as functions of the nozzle area and the PVR. The dashed line represent the optimal nozzle area that produces the lowest SVC pressure at a given PVR. These results are obtained from the algebraic model.

The cardiac output primarily depends on the nozzle area since a larger nozzle area directs more flow to the pulmonary circulation (Figure 4.31). Similar to the cardiac output, the pulmonary-to-systemic flow ratio is also primarily a function of the nozzle area (Figure 4.32). This is due to the fact that the pulmonary flow rare linearly increases with nozzle area while the systemic flow rate is almost independent of the nozzle size, as shown

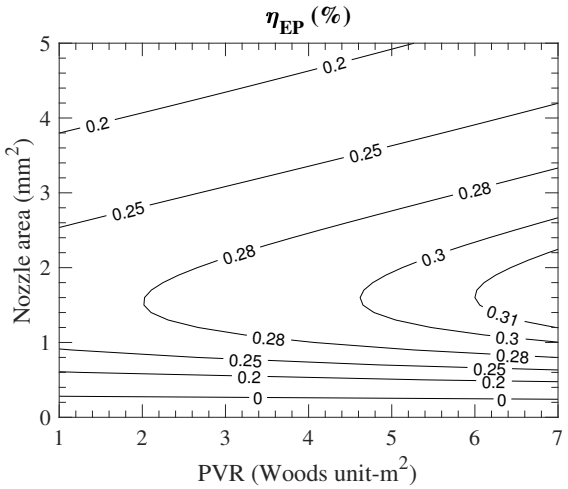

Figure 4.30: The ejector pump efficiency as functions of the nozzle area and the PVR. These results are obtained from the algebraic model.

in Figure 4.14. The aortic oxygen saturation also monotonically increases with the nozzle area (Figure 4.33). This dependence results from the pulmonary flow rate increasing linearly with the nozzle area, which in turn changes the balance between the oxygenated and deoxygenated blood in the atrium. The oxygen delivery shows a rather complex behavior (Figure 4.34). For small nozzle areas, the oxygen delivery increases linearly with the nozzle area and is independent of the PVR. On the other hand, it decreases monotonically with the PVR for large nozzle areas while remaining relatively independent from the nozzle area. This behavior at large nozzle areas can be explained by the gradual drop in cardiac output and systemic saturation as PVR increases (Figure 4.31 and 4.33).

These plots showcase the advantage of the algebraic model over CFD to fully survey all nozzle area and PVR with a fraction of the computational cost. Furthermore, the contour plots can be a powerful tool in clinical decision-making for the ABG procedure. It permits for the fast prediction of the SVC pressure, among others, for different patients. It also provides a means to predict how selecting a larger or smaller nozzle influences the outcome of an operation.

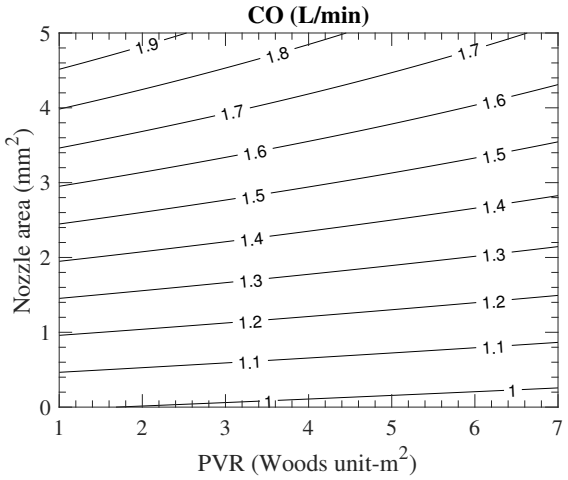

Figure 4.31: The cardiac output as functions of the nozzle area and the PVR. These results are produced by the algebraic model.

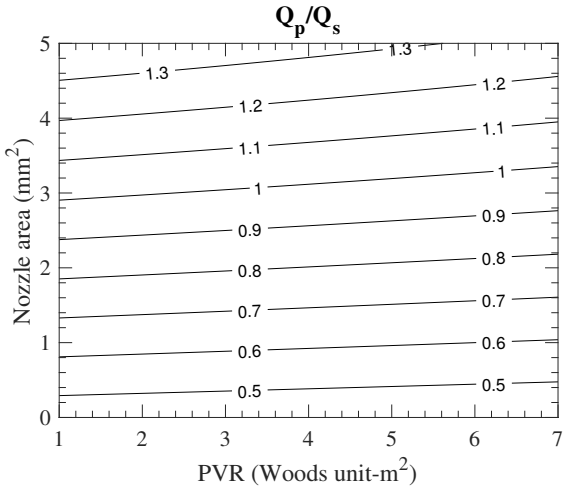

Figure 4.32: The pulmonary-to-systemic flow ratio as functions of the nozzle area and the PVR. These results are produced by the algebraic model.

4.4 Discussion

We introduced an algebraic model as a fast and accurate way to characterize the ABG circulation performance. One key component that dictates the accuracy of the algebraic model is the loss constants, C_s and C_p. Despite the fact that these constants are calculated by minimizing the difference between the model prediction and the CFD results, the computed values are physically reasonable. We introduced two non-dimensional head loss terms as functions of the flow rate-squared because the losses primarily occur due to the

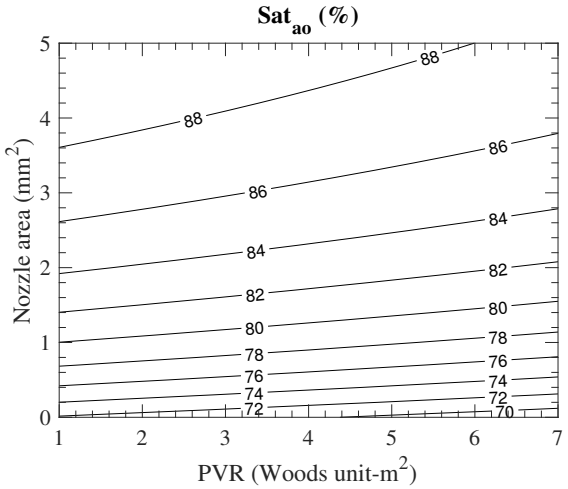

Figure 4.33: The aortic oxygen saturation as functions of the nozzle area and the PVR. These results are produced by the algebraic model.

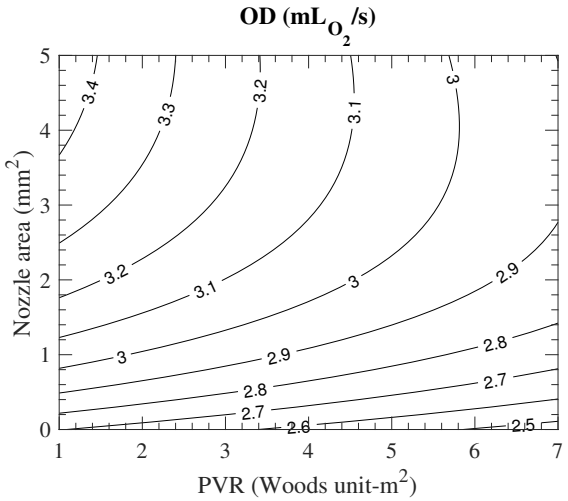

Figure 4.34: The oxygen delivery as functions of the nozzle area and the PVR. These results are produced by the algebraic model.

sharp change in flow directions in the shunt and SVC-PA regions. These loss terms can be compared to the Darcy–Weisbach equation (Equation 4.17) for head loss, Δp, in a pipe flow,

$$\Delta p = f_{\mathrm{D}} \frac{\rho L}{2D} \langle v \rangle^2, \tag{4.18}$$

where L is the pipe length, D is the pipe diameter, $\langle v \rangle$ is the mean velocity in pipe, and f_{D} is the friction factor. [24] In our study, the head loss constants, C_{s} and C_{p}, are related to

friction factors via

$$C = \frac{f_{\mathrm{D}} L}{2D}. \tag{4.19}$$

The lengths, L, of the shunt and pulmonary arteries are 1.7 and 3.5 cm, respectively, and the diameters, D, of the shunt and pulmonary arteries are 0.3 and 0.55 cm, respectively. Knowing the constants in our case, the friction factors for the shunt and the pulmonary arteries $f_{\mathrm{D}}^{\mathrm{s}}$ and $f_{\mathrm{D}}^{\mathrm{p}}$, are calculated to be 0.11 and 0.26, respectively. Both of the friction factors are comparable to the friction factors in pipe flow for the Reynolds numbers ($\approx$ 1000) of our simulation.

Three interesting observations can be made from the algebraic model results. First, parameters such as the pulmonary flow rate and the cardiac output are less sensitive to the PVR for smaller nozzle areas ($A_{\mathrm{nozzle}} \leq 2.0\mathrm{mm}^2$). This lack of sensitivity can be beneficial for infants who experience episodes of increased PVR after birth, during which sufficient blood circulation can be maintained. Second, even a small nozzle of 2.0 mm^2 is better than no nozzle when the oxygen delivery and systemic oxygen saturation are concerned. Regardless of PVR, these two parameters are elevated by 15% to 20% when a 2 mm^2 nozzle is added to the BDG. Such improvement in these metrics is significant considering that the early BDG complications are partly related to low oxygen saturation. [86, 141] Lastly, the version of the ejector pump utilized in this study can reduce the upper body (SVC) pressure for normal PVR and limit the pressure rise to a minimum when episodes of high PVR occur, thereby mitigating the risk of SVC syndrome reported in older studies. [38, 99] A more recent study on successful BDG operation further shows that the infant can endure an SVC pressure as high as 13.2 mmHg. [141] If we consider that pressure to be the maximum allowable SVC pressure, then a patient receiving a 2 mm^2 nozzle should remain in the safe zone as long as the PVR remains below 7 Wood units-m^2. Moreover, studies showed that the PVR value generally decreases as the oxygen saturation and the pulmonary arterial pressure are increased. [101, 113] For its higher

saturation and PA pressure, the ABG operation patients are expected to have a lower PVR than those undergoing the mBTS or BDG. Thus, the higher SVC pressure observed in the case of ABG may not materialize in practice.

Overall, the optimal nozzle size is in the range of 2 mm^2 and 3 mm^2. Smaller nozzle areas ($\approx$ 2 mm^2) are more suited for patients with wider ranges of PVR as the SVC pressure remains reasonably low even at high PVR values. Also, as discussed above, the flow rate parameters such as the pulmonary flow rate and cardiac output are more stable for smaller nozzle areas as PVR changes. Furthermore, since the cardiac output will be lower for smaller nozzle areas, the overall workload on the heart will be less. On the other hand, if the patient has relatively stable PVR, and can handle a larger ventricle load, a larger nozzle area ($\approx$ 3 mm^2) has more physiological benefits. The SVC pressure will be even lower than that of the case of smaller nozzle areas for normal PVR, as seen in Figure 4.12, which will further alleviate complications related to high SVC pressure. The aortic oxygen saturation and oxygen delivery will also be slightly higher. Finally, the pulmonary-to-systemic flow ratio will be exactly 1, which is considered the ideal situation. Outside of our optimal range, if the nozzle area is even smaller, the benefits of the ABG circulation are diminished since most of the energy through the shunt is lost through dissipation. For a nozzle larger than 3 mm^2, the excessive flow through the shunt overloads the pulmonary circulation, impeding the upper body circulation while creating unnecessarily high ventricle load.

An essential advantage of the algebraic model is its negligible cost that enables real-time predictions of post-operating conditions. That can be in the form of using this algebraic model in clinical settings to select the appropriate nozzle size that is patient-specific. One limitation of our algebraic model is the assumption of a constant PVR. As we discussed in this paper, the PVR changes as a function of the pulmonary arterial pressure and the pulmonary oxygen saturation. [101, 113] Such dynamic response is therefore

missing in the algebraic model. Accounting for this dependence in the future models will allow us to determine whether the improved pulmonary arterial pressure and oxygen saturation in the ABG are sufficient to prevent an elevated SVC pressure. Improvements on the shunt and nozzle design can help further reduce losses and improve the efficiency of the ABG to obtain an even lower SVC pressure. For example, a more smooth shunt transition can help reduce energy loss in the shunt. The SVC downstream loss due to the flow impingement can also be reduced if the SVC-PA junction is Y-shaped instead of T-shaped. However, any of these changes must be made while considering surgical feasibility, patient growth, and vascular remodeling.

4.5 Conclusion

An accurate algebraic model that was informed by the CFD was constructed to characterize the performance of the ABG procedure. With this algebraic model, we can explore and characterize the full relationship between design parameters and patient conditions, a feat that would not have been possible using CFD simulations alone. Optimization study shows that the mABG shunt is only successful in reducing the SVC pressure when the PVR is lower than 4.4 Woods unit-m^2. The model shows that there is little benefit in increasing the nozzle area beyond 2 mm^2 in terms of oxygen delivery and saturation. Our study introduces, for the first time, a procedure for real-time simulation of the ABG at an accuracy comparable to CFD.

CHAPTER 5

CONCLUSION AND FUTURE WORKS

This dissertation presented three numerical studies utilizing CFD and modeling techniques, focusing on enhancing the accuracy and speed of cardiovascular simulations. The harmonic balance frequency CFD solver proposed in Chapter 2 demonstrated its effectiveness for a range of cardiovascular simulations, providing a speedup of 10 to 100 times compared to conventional time-domain solvers. The harmonic balance solver's requirements are similar to those of conventional CFD simulations, making it a practical and efficient option for hemodynamics studies within the human circulatory system. The solver also demonstrated strong scaling advantages, making it more suitable for parallel processing on high-performance computing (HPC) systems. The truncation error from the boundary conditions used in the harmonic balance solver is a reliable indicator of overall solution error. The harmonic balance CFD solver is a valuable and promising tool for various cardiovascular and fluid dynamics applications, with the potential for further advancements and innovations.

The proposed solver's significant improvement in CFD speed brings us one step closer to performing patient-specific cardiovascular simulations in clinical settings. However, further research is still required in clinical imaging model construction, boundary condition acquisition, and understanding the physiological and pathological associations between fluid dynamics parameters and cardiovascular performance and diseases. Moreover, integrating different computational tools and designing user interfaces remains challenging for clinical adaptation since most clinicians are unfamiliar with Unix systems.

The harmonic balance solver also holds potential for other applications. Based on the physics of the flow, there are two fundamental requirements for the solver: (1) the flow must be laminar or close to laminar, and (2) the flow must exhibit steady periodic behav-

ior with a known frequency. Other flow situations that satisfy these requirements include respiratory flows, cerebrospinal fluid flows, microchannel flows, and similar cases. All these possible applications involve Reynolds numbers below 1000 and exhibit oscillatory behavior. Further studies can explore the accuracy and cost-efficiency of the harmonic balance solver when applied to these cases.

Additional functionalities can be developed for the harmonic balance solver, such as handling more complex boundary conditions, coupling the inlets and outlets with reduced-order models, or calculating the mesh motion with fluid-structure interactions. An interesting research direction specific to the harmonic balance solver is addressing the closure problem for periodic flows with unknown oscillation periods. For example, the solution is inherently periodic in flows over a cylinder that exhibit vortex shedding. However, the vortex shedding frequency is unknown prior to performing the simulation. The closure problem associated with unknown flow frequencies currently lacks a satisfactory solution. This issue can also be extended to turbulent flows, where the turbulence frequency forms a continuous spectrum. Further research should investigate how the turbulence closure problem can be addressed for the harmonic balance solver.

Solving the linear system resulting from the finite element method was a common challenge in this dissertation's first and second studies. A pseudo time-stepping scheme was used to improve the conditioning of the left-hand-side matrix to resolve the linear system convergence issue in the harmonic balance solver. In the second study, a new formulation was introduced for the stabilization parameter (τ_{SUPG}) used in the Streamline Upwind Petrov-Galerkin and Pressure Stabilizing Petrov-Galerkin method (SUPG/PSPG). The proposed formulation successfully provided a consistent solution across varying time step sizes, resolving the historical inconsistency observed with small time step sizes using the conventional τ_{SUPG} formulation. However, as discussed in Chapter 3, this formulation increased the number of linear solver iterations required. Both

studies employed the Generalized Minimal Residual Method (GMRES) to solve the linear system, using a standard Jacobi preconditioner for the tangent matrix. The results indicated that the current standard linear solver may not perform optimistically for solving these systems. Similar to the linear solver specialized for the conventional finite element solver for Navier-Stokes equations [50], future research can focus on developing specialized linear solvers or preconditioners for the harmonic balance solver and/or the consistent stabilization formulation. Such specialized linear solvers could further enhance simulation speed.

The final study presented in this dissertation developed a CFD-based 0D mathematical model to analyze the performance of a specific surgical procedure for single-ventricle patients. This model enabled a thorough investigation of the relationship between design parameters and patient conditions, which would have been cost-prohibitive using CFD simulations alone. The study introduced a novel method for real-time simulation of the procedure using the reduced order mathematical model with accuracy comparable to CFD simulations. As this study demonstrated, reduced-order modeling is a valuable tool for design optimization, parametric studies, and real-time simulations of specific procedures. The primary challenge for this study was the computational time required to generate fifteen CFD solutions as the training data, which took approximately three weeks using 288 CPU cores. Recently developed data-driven deep learning models have required even more CFD solution sets for training, often in the hundreds. This high demand for CFD data underscores the value of the harmonic balance frequency solver, which can generate tens to hundreds of high-accuracy simulation results using the same computational resources as a single conventional CFD simulation. Future research can explore the integration between the harmonic balance solver and reduced-order models, such as lumped parameter networks and neural network-based models.

In conclusion, this paper represents significant progress in performing fast and highly

accurate cardiovascular simulations. The numerical methods developed in this dissertation can also benefit other fields that utilize CFD simulations as a research tool. There are still unanswered problems and potential improvements that could lead to impactful research in the future.

APPENDIX A

APPENDIX FOR CHAPTER 4

The values of the LPN (Figure 4.4) elements are shown in Table A.1. Outside the heart model, all the resistors, capacitors, and inductors have linear behavior. To model turbulence associated with the heart valves, two resistances are included in the LPN, which pressure drop through them is proportional to the square of their flow rate. Heart chambers pressure is considered to be composed of active and passive parts. The atrial pressure is model using,

$$P_a = A_a E_a (V_a - V_{a_u}) + P_{a_0}(e^{K_a(V_a - V_{a_u})} - 1). \tag{A.1}$$

A_a is modeled with sinusoidal function which is non-zero during atrium contraction and E_a, P_{a_0}, K_a, and V_{a_u} are the constants of this model. The same model is used for ventricle, except the active pressure, that is, first term in Equation (A.1), is replaced with a parabolic function,

$$P_v = A_v[E_{v_1}(V_v - V_{v_u}) + E_{v_2}(V_v - V_{v_u})^2] + P_{v_0}(e^{K_v(V_v - V_{v_u})} - 1). \tag{A.2}$$

All the constants of the heart model along with the rest of LPN are shown in Table A.1.

Table A.1: Figure 4.4 parameters values. R, resistance; C, capacitance; L, inductance. The locations of UBA, UBB, UBV, etc.) are marked in Figure 4.4. E, elastance; P, pressure; K, constant; V, volume; v, single ventricle; u, unstressed; a, atrium; *tric*, tricuspid; *ao*, aorta; *asd*, atrial septal defect. Data from [120, 51].

Parameter	Value	Unit
R_{UBA}	28.0899	mmHg s/mL
C_{UBA}	0.04430	mL/mmHg
L_{UBA}	0.02138	mmHg s^2/mL
R_{UBB}	0.64510	mmHg s/mL
C_{UBB}	0.15515	mL/mmHg
R_{UBV}	0.16529	mmHg s/mL
C_{UBV}	2.03945	mL/mmHg

Table A.1: *Cont.*

Parameter	Value	Unit
R_{PAB}	0.83376	mmHg s/mL
C_{PAB}	0.02039	mL/mmHg
R_{PVB}	0.02194	mmHg s/mL
C_{PVB}	0.44375	mL/mmHg
R_{LBA}	7.02239	mmHg s/mL
C_{LBA}	0.07758	mL/mmHg
L_{LBA}	0.01069	mmHg s^2/mL
R_{LBB}	0.64510	mmHg s/mL
C_{LBB}	0.07758	mL/mmHg
R_{LBV}	0.16529	mmHg s/mL
C_{LBV}	2.03945	mL/mmHg
R_{CA1}	10.6739	mmHg s/mL
C_{CA1}	1.9435×10^{-3}	mL/mmHg
R_{CA2}	10.6739	mmHg s/mL
C_{CA2}	5.1827×10^{-3}	mL/mmHg
R_{CB}	21.3477	mmHg s/mL
C_{CB}	7.7741×10^{-3}	mL/mmHg
R_{CV}	10.6739	mmHg s/mL
C_{CV}	0.05×10^{-3}	mL/mmHg
E_{v_1}	18.5	mmHg/mL
E_{v_2}	−0.042	mmHg/mL^2
V_{v_u}	4.0	mL
P_{v_0}	0.9	mmHg
K_v	0.062	1/mL
E_a	7.35	mmHg/mL
V_{a_u}	1.0	mL
P_{a_0}	0.17	mmHg
K_a	0.484	1/mL
$\hat{R}_{tric}$	4×10^{-5}	mmHg s^2/mL^2
$\hat{R}_{ao}$	4×10^{-4}	mmHg s^2/mL^2
R_v	0.09	mmHg s/mL
R_{asd}	0.001	mmHg s/mL
C_{ao}	0.041555	mL/mmHg

BIBLIOGRAPHY

[1] Naveed Ahmed, Tomas Chacon Rebollo, Volker John, and Samuele Rubino. A review of variational multiscale methods for the simulation of turbulent incompressible flows. *Archives of Computational Methods in Engineering*, 24:115–164, 2017.

[2] I Akkerman, Y Bazilevs, VM Calo, TJR Hughes, and S Hulshoff. The role of continuity in residual-based variational multiscale modeling of turbulence. *Computational Mechanics*, 41:371–378, 2008.

[3] Jamal A Alhashemi, Maurizio Cecconi, and Christoph K Hofer. Cardiac output monitoring: an integrative perspective. *Critical Care*, 15(2):214, 2011.

[4] Luca Antiga, Marina Piccinelli, Lorenzo Botti, Bogdan Ene-Iordache, Andrea Remuzzi, and David A Steinman. An image-based modeling framework for patient-specific computational hemodynamics. *Medical & biological engineering & computing*, 46:1097–1112, 2008.

[5] Peter Arbenz, Daniel Hupp, and Dominik Obrist. Comparison of parallel time-periodic Navier-Stokes solvers. In *International Conference on Parallel Processing and Applied Mathematics*, pages 57–67. Springer, 2017.

[6] Gregory Arbia, Chiara Corsini, Mahdi Esmaily Moghadam, Alison L. Marsden, Francesco Migliavacca, Giancarlo Pennati, Tain-Yen Hsia, and Irene E. Vignon-Clementel. Numerical blood flow simulation in surgical corrections: what do we need for an accurate analysis? *Journal of Surgical Research*, 186(1):44–55, 2014.

[7] Christopher J Arthurs, Rostislav Khlebnikov, Alex Melville, Marija Marčan, Alberto Gomez, Desmond Dillon-Murphy, Federica Cuomo, Miguel Silva Vieira, Jonas Schollenberger, Sabrina R Lynch, et al. Crimson: An open-source software framework for cardiovascular integrated modelling and simulation. *PLoS computational biology*, 17(5):e1008881, 2021.

[8] Michael R Avendi, Arash Kheradvar, and Hamid Jafarkhani. A combined deep-learning and deformable-model approach to fully automatic segmentation of the left ventricle in cardiac mri. *Medical image analysis*, 30:108–119, 2016.

[9] Ulrike Bartram, Jürg Grünenfelder, and MD Richard Van Praagh. Causes of death after the modified norwood procedure: a study of 122 postmortem cases. *The Annals of thoracic surgery*, 64(6):1795–1802, 1997.

[10] Y Bazilevs and I26011061290 Akkerman. Large eddy simulation of turbulent taylor–couette flow using isogeometric analysis and the residual-based variational multiscale method. *Journal of Computational Physics*, 229(9):3402–3414, 2010.

[11] Y Bazilevs, VM Calo, JA Cottrell, TJR Hughes, A Reali, and G Scovazzi. Variational multiscale residual-based turbulence modeling for large eddy simulation of incompressible flows. *Computer methods in applied mechanics and engineering*, 197(1-4):173–201, 2007.

[12] Y. Bazilevs, J.R. Gohean, T.J.R. Hughes, R.D. Moser, and Y. Zhang. Patient-specific isogeometric fluid-structure interaction analysis of thoracic aortic blood flow due to implantation of the Jarvik 2000 left ventricular assist device. *Computer Methods in Applied Mechanics and Engineering*, 198(45-46):3534–3550, 2009.

[13] Yuri Bazilevs, Victor M Calo, Thomas JR Hughes, and Yongjie Zhang. Isogeometric fluid-structure interaction: theory, algorithms, and computations. *Computational mechanics*, 43:3–37, 2008.

[14] Yuri Bazilevs, Victor M Calo, Yongjie Zhang, and TJR2246128 Hughes. Isogeometric fluid–structure interaction analysis with applications to arterial blood flow. *Computational Mechanics*, 38:310–322, 2006.

[15] Yuri Bazilevs, M-C Hsu, David J Benson, Sethu Sankaran, and Alison L Mars-

den. Computational fluid–structure interaction: methods and application to a total cavopulmonary connection. *Computational Mechanics*, 45:77–89, 2009.

[16] P. W. Bearman and E. D. Obasaju. An experimental study of pressure fluctuations on fixed and oscillating square-section cylinders. *Journal of Fluid Mechanics*, 119:297–321, 1982.

[17] R.M. Berne and M.N. Levy. *Cardiovascular Physiology*. Mosby physiology monograph series. Mosby, 2001.

[18] Rajesh Bhaskaran and Lance Collins. Introduction to cfd basics. *Cornell University-Sibley School of Mechanical and Aerospace Engineering*, pages 1–21, 2002.

[19] Pavel B. Bochev, Max D. Gunzburger, and John N. Shadid. Stability of the supg finite element method for transient advection–diffusion problems. *Computer Methods in Applied Mechanics and Engineering*, 193(23):2301–2323, 2004.

[20] Matthew D Bockman, Akash P Kansagra, Shawn C Shadden, Eric C Wong, and Alison L Marsden. Fluid mechanics of mixing in the vertebrobasilar system: comparison of simulation and mri. *Cardiovascular Engineering and Technology*, 3:450–461, 2012.

[21] Edward L Bove, Francesco Migliavacca, Marc R de Leval, Rossella Balossino, Giancarlo Pennati, Thomas R Lloyd, Sachin Khambadkone, Tain-Yen Hsia, and Gabriele Dubini. Use of mathematic modeling to compare and predict hemodynamic effects of the modified blalock–taussig and right ventricle–pulmonary artery shunts for hypoplastic left heart syndrome. *The Journal of thoracic and cardiovascular surgery*, 136(2):312–320, 2008.

[22] Frieke MA Box, Rob J van der Geest, Marcel CM Rutten, and Johan HC Reiber. The influence of flow, vessel diameter, and non-newtonian blood viscosity on the wall

shear stress in a carotid bifurcation model for unsteady flow. *Investigative radiology*, 40(5):277–294, 2005.

[23] Alexander N Brooks and Thomas JR Hughes. Streamline upwind/petrov-galerkin formulations for convection dominated flows with particular emphasis on the incompressible navier-stokes equations. *Computer methods in applied mechanics and engineering*, 32(1-3):199–259, 1982.

[24] Glenn O. Brown. *The History of the Darcy-Weisbach Equation for Pipe Flow Resistance*, pages 34–43.

[25] Erik Burman. Consistent supg-method for transient transport problems: Stability and convergence. *Computer Methods in Applied Mechanics and Engineering*, 199(17):1114–1123, 2010.

[26] N Byrne, M Velasco Forte, A Tandon, I Valverde, and T Hussain. A systematic review of image segmentation methodology, used in the additive manufacture of patient-specific 3d printed models of the cardiovascular system. *JRSM cardiovascular disease*, 5:2048004016645467, 2016.

[27] Carlos E Cardenas, Jinzhong Yang, Brian M Anderson, Laurence E Court, and Kristy B Brock. Advances in auto-segmentation. In *Seminars in radiation oncology*, volume 29, pages 185–197. Elsevier, 2019.

[28] Joseph Caspi, Timothy W Pettitt, Theodorus Mulder, and Aluizio Stopa. Development of the pulmonary arteries after the norwood procedure: comparison between blalock-taussig shunt and right ventricular–pulmonary artery conduit. *The Annals of thoracic surgery*, 86(4):1299–1304, 2008.

[29] Chen Chen, Chen Qin, Huaqi Qiu, Giacomo Tarroni, Jinming Duan, Wenjia Bai, and Daniel Rueckert. Deep learning for cardiac image segmentation: a review. *Frontiers in cardiovascular medicine*, 7:25, 2020.

[30] Bongjae Chung and Juan Raul Cebral. Cfd for evaluation and treatment planning of aneurysms: review of proposed clinical uses and their challenges. *Annals of biomedical engineering*, 43:122–138, 2015.

[31] ALAIN Cloutier, JUDITH M Ash, JEFFREY F Smallhorn, WG Williams, GA Trusler, RD Rowe, and M Rabinovitch. Abnormal distribution of pulmonary blood flow after the glenn shunt or fontan procedure: risk of development of arteriovenous fistulae. *Circulation*, 72(3):471–479, 1985.

[32] R. Codina, M. Vázquez, and O. C. Zienkiewicz. A general algorithm for compressible and incompressible flows. part iii: The semi-implicit form. *International Journal for Numerical Methods in Fluids*, 27(1-4):13–32, 1998.

[33] Ramon Codina. Stabilization of incompressibility and convection through orthogonal sub-scales in finite element methods. *Computer methods in applied mechanics and engineering*, 190(13-14):1579–1599, 2000.

[34] Ramon Codina, Javier Principe, Oriol Guasch, and Santiago Badia. Time dependent subscales in the stabilized finite element approximation of incompressible flow problems. *Computer Methods in Applied Mechanics and Engineering*, 196(21-24):2413–2430, 2007.

[35] Lester A Critchley, Anna Lee, and Anthony M-H Ho. A critical review of the ability of continuous cardiac output monitors to measure trends in cardiac output. *Anesthesia & Analgesia*, 111(5):1180–1192, 2010.

[36] William M DeCampli. The steam locomotive makes a comeback: A new solution to staged single-ventricle palliation? *The Journal of thoracic and cardiovascular surgery*, 149(3):706–707, 2015.

[37] Marcelo F Di Carli, Tal Geva, and Ravin Davidoff. The future of cardiovascular imaging. *Circulation*, 133(25):2640–2661, 2016.

[38] Duccio di Carlo, William G Williams, Robert M Freedom, George A Trusler, and Richard D Rowe. The role of cava-pulmonary (glenn) anastomosis in the palliative treatment of congenital heart disease. *The Journal of thoracic and cardiovascular surgery*, 83(3):437–442, 1982.

[39] Roel S Driessen, Ibrahim Danad, Wijnand J Stuijfzand, Pieter G Raijmakers, Stefan P Schumacher, Pepijn A Van Diemen, Jonathon A Leipsic, Juhani Knuuti, S Richard Underwood, Peter M van de Ven, et al. Comparison of coronary computed tomography angiography, fractional flow reserve, and perfusion imaging for ischemia diagnosis. *Journal of the American College of Cardiology*, 73(2):161–173, 2019.

[40] Yves d'Udekem, Mary Y Xu, John C Galati, Siming Lu, Ajay J Iyengar, Igor E Konstantinov, Gavin R Wheaton, James M Ramsay, Leeanne E Grigg, Johnny Millar, et al. Predictors of survival after single-ventricle palliation: the impact of right ventricular dominance. *Journal of the American College of Cardiology*, 59(13):1178–1185, 2012.

[41] Petter Dyverfeldt, Malenka Bissell, Alex J Barker, Ann F Bolger, Carl-Johan Carlhäll, Tino Ebbers, Christopher J Francios, Alex Frydrychowicz, Julia Geiger, Daniel Giese, et al. 4d flow cardiovascular magnetic resonance consensus statement. *Journal of Cardiovascular Magnetic Resonance*, 17(1):1–19, 2015.

[42] David M Eckmann, Shelly Bowers, Mark Stecker, and Albert T Cheung. Hematocrit, volume expander, temperature, and shear rate effects on blood viscosity. *Anesthesia & Analgesia*, 91(3):539–545, 2000.

[43] Mahdi Esmaily, Yuri Bazilevs, Tain-Yen Hsia, Irene Vignon-Clementel, and Alison Marsden. A comparison of outlet boundary treatments for prevention of backflow divergence with relevance to blood flow simulations. *Computational Mechanics*, 48(3):277–291, 2011.

[44] Mahdi Esmaily and Dongjie Jia. An augmented streamline upwind/petrov-galerkin method for the time-spectral convection-diffusion equation. *Petrov-Galerkin Method for the Time-Spectral Convection-Diffusion Equation*, 2023.

[45] Mahdi Esmaily and Dongjie Jia. A stabilized formulation for the solution of the incompressible unsteady stokes equations in the frequency domain. *Journal of Computational Physics*, 473:111736, 2023.

[46] Mahdi Esmaily and Dongjie Jia. A new stabilized time-spectral finite element solver for fast simulation of blood flow. *Computer Methods in Applied Mechanics and Engineering*, 425:116939, 2024.

[47] M Esmaily-Moghadam, Y Bazilevs, and AL Marsden. Impact of data distribution on the parallel performance of iterative linear solvers with emphasis on cfd of incompressible flows. *Computational Mechanics*, 55(1):93–103, 2015.

[48] Mahdi Esmaily-Moghadam, Yuri Bazilevs, and Alison Marsden. Low entropy data mapping for sparse iterative linear solvers. In *Proceedings of the conference on extreme science and engineering discovery environment: gateway to discovery*, pages 1–4, 2013.

[49] Mahdi Esmaily-Moghadam, Yuri Bazilevs, and Alison L Marsden. A new preconditioning technique for implicitly coupled multidomain simulations with applications to hemodynamics. *Computational Mechanics*, 52(5):1141–1152, 2013.

[50] Mahdi Esmaily-Moghadam, Yuri Bazilevs, and Alison L Marsden. A bi-partitioned iterative algorithm for solving linear systems arising from incompressible flow problems. *Computer Methods in Applied Mechanics and Engineering*, 286:40–62, 2015.

[51] Mahdi Esmaily Moghadam, Tain-Yen Hsia, Alison L Marsden, Modeling of Congenital Hearts Alliance (MOCHA) Investigators, et al. The assisted bidirectional glenn: A novel surgical approach for first-stage single-ventricle heart palliation. *The Journal of thoracic and cardiovascular surgery*, 149(3):699–705, 2015.

[52] Mahdi Esmaily Moghadam, Francesco Migliavacca, Irene E Vignon-Clementel, Tain-Yen Hsia, Alison L Marsden, Modeling of Congenital Hearts Alliance (MOCHA) Investigators, et al. Optimization of shunt placement for the norwood surgery using multi-domain modeling. *Journal of biomechanical engineering*, 134(5), 2012.

[53] Mahdi Esmaily-Moghadam, Bari Murtuza, Tain-Yen Hsia, and Alison Marsden. Simulations reveal adverse hemodynamics in patients with multiple systemic to pulmonary shunts. *Journal of biomechanical engineering*, 137(3):031001, 2015.

[54] John A. Evans, Christopher Coley, Ryan M. Aronson, Corey L. Wetterer-Nelson, and Yuri Bazilevs. *Residual-Based Large Eddy Simulation with Isogeometric Divergence-Conforming Discretizations*, pages 91–130. Springer International Publishing, Cham, 2018.

[55] Robert Eymard, Thierry Gallouët, and Raphaèle Herbin. Finite volume methods. *Handbook of numerical analysis*, 7:713–1018, 2000.

[56] Yurun Fan, Roger I Tanner, and Nhan Phan-Thien. Galerkin/least-square finite-element methods for steady viscoelastic flows. *Journal of Non-Newtonian Fluid Mechanics*, 84(2-3):233–256, 1999.

[57] Edward Ferdian, Avan Suinesiaputra, David J Dubowitz, Debbie Zhao, Alan Wang, Brett Cowan, and Alistair A Young. 4dflownet: super-resolution 4d flow mri using deep learning and computational fluid dynamics. *Frontiers in Physics*, 8:138, 2020.

[58] Benjamim Ficial, Anna E Finnemore, David J Cox, Kathryn M Broadhouse, Anthony N Price, Giuliana Durighel, Georgia Ekitzidou, Joseph V Hajnal, A David Edwards, and Alan M Groves. Validation study of the accuracy of echocardiographic measurements of systemic blood flow volume in newborn infants. *Journal of the American Society of Echocardiography*, 26(12):1365–1371, 2013.

[59] C Alberto Figueroa, Irene E Vignon-Clementel, Kenneth E Jansen, Thomas JR Hughes, and Charles A Taylor. A coupled momentum method for modeling blood flow in three-dimensional deformable arteries. *Computer methods in applied mechanics and engineering*, 195(41-43):5685–5706, 2006.

[60] Casey M Fleeter, Gianluca Geraci, Daniele E Schiavazzi, Andrew M Kahn, and Alison L Marsden. Multilevel and multifidelity uncertainty quantification for cardiovascular hemodynamics. *Computer methods in applied mechanics and engineering*, 365:113030, 2020.

[61] F Fontan and E Baudet. Surgical repair of tricuspid atresia. *Thorax*, 26(3):240–248, 1971.

[62] Francis Fontan, John W Kirklin, Guy Fernandez, Francisco Costa, David C Naftel, Francesco Tritto, and Eugene H Blackstone. Outcome after a" perfect" fontan operation. *Circulation*, 81(5):1520–1536, 1990.

[63] Centers for Disease Control and Prevention. Heart disease facts. `https://www.cdc.gov/heart-disease/data-research/facts-stats/index.html`. Accessed: 2024-09-13.

[64] Leopoldo P Franca and Sérgio L Frey. Stabilized finite element methods: Ii. the incompressible navier-stokes equations. *Computer Methods in Applied Mechanics and Engineering*, 99(2-3):209–233, 1992.

[65] Matteo Frigo and Steven G Johnson. The design and implementation of fftw3. *Proceedings of the IEEE*, 93(2):216–231, 2005.

[66] William WL Glenn. Circulatory bypass of the right side of the heart: shunt between superior vena cava and distal right pulmonary artery—report of clinical application. *New England Journal of Medicine*, 259(3):117–120, 1958.

[67] William WL Glenn, Nelson K Ordway, Norman S Talner, and EDWARD P CALL JR. Circulatory bypass of the right side of the heart: Vi. shunt between superior vena cava and distal right pulmonary artery; report of clinical application in thirty-eight cases. *Circulation*, 31(2):172–189, 1965.

[68] Arathi Gopinath, Edwin van der Weide, Juan Alonso, Antony Jameson, Kivanc Ekici, and Kenneth Hall. Three-dimensional unsteady multi-stage turbomachinery simulations using the harmonic balance technique. In *45th AIAA Aerospace Sciences Meeting and Exhibit*, page 892, 2007.

[69] Massimo Griselli, Simon P McGuirk, Victor Ofoe, Oliver Stümper, John GC Wright, Joseph V de Giovanni, David J Barron, and William J Brawn. Fate of pulmonary arteries following norwood procedure. *European journal of cardio-thoracic surgery*, 30(6):930–935, 2006.

[70] Kenneth C Hall, Kivanc Ekici, Jeffrey P Thomas, and Earl H Dowell. Harmonic balance methods applied to computational fluid dynamics problems. *International Journal of Computational Fluid Dynamics*, 27(2):52–67, 2013.

[71] Kenneth C Hall, Jeffrey P Thomas, and William S Clark. Computation of unsteady nonlinear flows in cascades using a harmonic balance technique. *AIAA journal*, 40(5):879–886, 2002.

[72] K Harrison, H Pullen, C Welsh, O Oktay, J Alvarez-Valle, and R Jena. Machine learning for auto-segmentation in radiotherapy planning. *Clinical Oncology*, 34(2):74–88, 2022.

[73] M Heinemann, J Breuer, V Steger, E Steil, L Sieverding, and G Ziemer. Incidence and impact of systemic venous collateral development after glenn and fontan procedures. *The Thoracic and cardiovascular surgeon*, 49(03):172–178, 2001.

[74] Gerhard A Holzapfel. *Nonlinear solid mechanics: a continuum approach for engineering science*. Kluwer Academic Publishers Dordrecht, 2002.

[75] M.-C. Hsu, Y. Bazilevs, V.M. Calo, T.E. Tezduyar, and T.J.R. Hughes. Improving stability of stabilized and multiscale formulations in flow simulations at small time steps. *Computer Methods in Applied Mechanics and Engineering*, 199(13):828–840, 2010.

[76] Thomas JR Hughes. A multidimentional upwind scheme with no crosswind diffusion. *Finite element methods for convection dominated flows, AMD 34*, 1979.

[77] Thomas JR Hughes. *The finite element method: linear static and dynamic finite element analysis*. Prentice-Hall, Inc., Englewood Cliffs, 1987.

[78] Thomas JR Hughes. Recent progress in the development and understanding of SUPG methods with special reference to the compressible Euler and Navier-Stokes equations. *International journal for numerical methods in fluids*, 7(11):1261–1275, 1987.

[79] Thomas JR Hughes and Michel Mallet. A new finite element formulation for computational fluid dynamics: III. the generalized streamline operator for multidimensional advective-diffusive systems. *Computer methods in applied mechanics and engineering*, 58(3):305–328, 1986.

[80] Thomas JR Hughes and Michel Mallet. A new finite element formulation for computational fluid dynamics: III. the generalized streamline operator for multidimensional advective-diffusive systems. *Computer methods in applied mechanics and engineering*, 58(3):305–328, 1986.

[81] Thomas JR Hughes, Guglielmo Scovazzi, and Tayfun E Tezduyar. Stabilized methods for compressible flows. *Journal of Scientific Computing*, 43:343–368, 2010.

[82] Daniel Hupp, Peter Arbenz, and Dominik Obrist. A parallel Navier–Stokes solver

using spectral discretisation in time. *International journal of computational fluid dynamics*, 30(7-10):489–494, 2016.

[83] Antony Jameson, J Alonso, and M McMullen. Application of a non-linear frequency domain solver to the euler and navier-stokes equations. In *40th AIAA aerospace sciences meeting & exhibit*, page 120, 2002.

[84] Kenneth E Jansen, Christian H Whiting, and Gregory M Hulbert. A generalized-α method for integrating the filtered Navier–Stokes equations with a stabilized finite element method. *Computer methods in applied mechanics and engineering*, 190(3-4):305–319, 2000.

[85] Kenneth E. Jansen, Christian H. Whiting, and Gregory M. Hulbert. A generalized-α method for integrating the filtered navier–stokes equations with a stabilized finite element method. *Computer Methods in Applied Mechanics and Engineering*, 190(3):305–319, 2000.

[86] Robert DB Jaquiss, Nancy S Ghanayem, George M Hoffman, Raymond T Fedderly, Joseph R Cava, Kathleen A Mussatto, and James S Tweddell. Early cavopulmonary anastomosis in very young infants after the norwood procedure: impact on oxygenation, resource utilization, and mortality. *The Journal of thoracic and cardiovascular surgery*, 127(4):982–989, 2004.

[87] Dongjie Jia and Mahdi Esmaily. Characterization of the ejector pump performance for the assisted bidirectional glenn procedure. *Fluids*, 7(1):31, 2022.

[88] Dongjie Jia and Mahdi Esmaily. A time-consistent stabilized finite element method for fluids with applications to hemodynamics. *Scientific Reports*, 13(1):19120, 2023.

[89] Dongjie Jia, Byunghwan Jeon, Hyung-Bok Park, Hyuk-Jae Chang, and Lucy T Zhang. Image-based flow simulations of pre-and post-left atrial appendage closure in the left atrium. *Cardiovascular Engineering and Technology*, 10:225–241, 2019.

[90] Dongjie Jia, Matthew Peroni, Tigran Khalapyan, and Mahdi Esmaily. An efficient assisted bidirectional glenn design with lowered superior vena cava pressure for stage-one single ventricle patients. *Journal of Biomechanical Engineering*, 143(7), 2021.

[91] Volker John and Ellen Schmeyer. Finite element methods for time-dependent convection–diffusion–reaction equations with small diffusion. *Computer Methods in Applied Mechanics and Engineering*, 198(3):475–494, 2008.

[92] A.A. Johnson and T.E. Tezduyar. Mesh update strategies in parallel finite element computations of flow problems with moving boundaries and interfaces. *Computer Methods in Applied Mechanics and Engineering*, 119(1):73–94, 1994.

[93] David Kamensky, Ming-Chen Hsu, Dominik Schillinger, John A Evans, Ankush Aggarwal, Yuri Bazilevs, Michael S Sacks, and Thomas JR Hughes. An immersogeometric variational framework for fluid–structure interaction: Application to bioprosthetic heart valves. *Computer methods in applied mechanics and engineering*, 284:1005–1053, 2015.

[94] David Kamensky, Ming-Chen Hsu, Yue Yu, John A Evans, Michael S Sacks, and Thomas JR Hughes. Immersogeometric cardiovascular fluid–structure interaction analysis with divergence-conforming b-splines. *Computer methods in applied mechanics and engineering*, 314:408–472, 2017.

[95] George Karypis and Vipin Kumar. MeTis: Unstructured Graph Partitioning and Sparse Matrix Ordering System, Version 4.0. `http://www.cs.umn.edu/~metis`, 2009.

[96] Hyun Jin Kim, IE Vignon-Clementel, JS Coogan, CA Figueroa, KE Jansen, and CA Taylor. Patient-specific modeling of blood flow and pressure in human coronary arteries. *Annals of biomedical engineering*, 38:3195–3209, 2010.

[97] Taha Sabri Koltukluoğlu, Gregor Cvijetić, and Ralf Hiptmair. Harmonic balance techniques in cardiovascular fluid mechanics. In *International Conference on Medical Image Computing and Computer-Assisted Intervention*, pages 486–494. Springer, 2019.

[98] Bruno Koobus and Charbel Farhat. A variational multiscale method for the large eddy simulation of compressible turbulent flows on unstructured meshes—application to vortex shedding. *Computer Methods in Applied Mechanics and Engineering*, 193(15):1367–1383, 2004. Recent Advances in Stabilized and Multiscale Finite Element Methods.

[99] Gary S Kopf, Hillel Laks, Horace C Stansel, William E Hellenbrand, Charles S Kleinman, and Norman S Talner. Thirty-year follow-up of superior vena cava-pulmonary artery (glenn) shunts. *The Journal of thoracic and cardiovascular surgery*, 100(5):662–671, 1990.

[100] Pierre Ladeveze and Dominique Leguillon. Error estimate procedure in the finite element method and applications. *SIAM Journal on Numerical Analysis*, 20(3):485–509, 1983.

[101] Satyan Lakshminrusimha, Daniel D Swartz, Sylvia F Gugino, Chang-Xing Ma, Karen A Wynn, Rita M Ryan, James A Russell, and Robin H Steinhorn. Oxygen concentration and pulmonary hemodynamics in newborn lambs with pulmonary hypertension. *Pediatric research*, 66(5):539–544, 2009.

[102] Randall J. LeVeque. *Finite Difference Methods for Ordinary and Partial Differential Equations*. Society for Industrial and Applied Mathematics, 2007.

[103] Gaoyang Li, Haoran Wang, Mingzi Zhang, Simon Tupin, Aike Qiao, Youjun Liu, Makoto Ohta, and Hitomi Anzai. Prediction of 3d cardiovascular hemodynamics before and after coronary artery bypass surgery via deep learning. *Communications biology*, 4(1):99, 2021.

[104] Fuyou Liang and Hao Liu. A closed-loop lumped parameter computational model for human cardiovascular system. *JSME International Journal Series C Mechanical Systems, Machine Elements and Manufacturing*, 48(4):484–493, 2005.

[105] Peter Libby and Pierre Theroux. Pathophysiology of coronary artery disease. *Circulation*, 111(25):3481–3488, 2005.

[106] D. A. Lyn, S. Einav, W. Rodi, and J.-H. Park. A laser-doppler velocimetry study of ensemble-averaged characteristics of the turbulent near wake of a square cylinder. *Journal of Fluid Mechanics*, 304:285–319, 1995.

[107] Richard D Mainwaring, John J Lamberti, Karen Uzark, Robert L Spicer, Mark W Cocalis, and John W Moore. Effect of accessory pulmonary blood flow on survival after the bidirectional glenn procedure. *Circulation*, 100(suppl_2):II–151, 1999.

[108] Michael Markl, Frandics P Chan, Marcus T Alley, Kris L Wedding, Mary T Draney, Chris J Elkins, David W Parker, Ryan Wicker, Charles A Taylor, Robert J Herfkens, et al. Time-resolved three-dimensional phase-contrast mri. *Journal of Magnetic Resonance Imaging*, 17(4):499–506, 2003.

[109] Michael Markl, Alex Frydrychowicz, Sebastian Kozerke, Mike Hope, and Oliver Wieben. 4d flow mri. *Journal of Magnetic Resonance Imaging*, 36(5):1015–1036, 2012.

[110] Alison L Marsden. Optimization in cardiovascular modeling. *Annual review of fluid mechanics*, 46:519–546, 2014.

[111] Alison L Marsden and Mahdi Esmaily-Moghadam. Multiscale modeling of cardiovascular flows for clinical decision support. *Applied Mechanics Reviews*, 67(3):030804, 2015.

[112] The Mathworks, Inc., Natick, Massachusetts. *MATLAB version 9.11.0.1751886 (R2021b)*, 1990-2021.

[113] Emilio Mazza and Darren B. Taichman. Chapter 1 - functions and control of the pulmonary circulation. In Jess Mandel and Darren Taichman, editors, *Pulmonary Vascular Disease*, page 1–19. W.B. Saunders, Philadelphia, 2006.

[114] Matthew McMullen, Antony Jameson, and Juan Alonso. Acceleration of convergence to a periodic steady state in turbomachinery flows. In *39th aerospace sciences meeting and exhibit*, page 152, 2001.

[115] David M McQueen and Charles S Peskin. A three-dimensional computer model of the human heart for studying cardiac fluid dynamics. *ACM Siggraph Computer Graphics*, 34(1):56–60, 2000.

[116] Alan M Mendelsohn, Edward L Bove, Flavian M Lupinetti, Dennis C Crowley, Thomas R Lloyd, and Robert H Beekman III. Central pulmonary artery growth patterns after the bidirectional glenn procedure. *The Journal of thoracic and cardiovascular surgery*, 107(5):1284–1290, 1994.

[117] Chenwei Meng, Anirban Bhattacharjee, and Mahdi Esmaily. A scalable spectral stokes solver for simulation of time-periodic flows in complex geometries. *Journal of Computational Physics*, 445:110601, 2021.

[118] Francesco Migliavacca, Gabriele Dubini, Giancarlo Pennati, Riccardo Pietrabissa, Roberto Fumero, Tain-Yen Hsia, and Marc R de Leval. Computational model of the fluid dynamics in systemic-to-pulmonary shunts. *Journal of biomechanics*, 33(5):549–557, 2000.

[119] Francesco Migliavacca, Giancarlo Pennati, Elena Di Martino, Gabriele Dubini, and Riccardo Pietrabissa. Pressure drops in a distensible model of end-to-side anastomosis in systemic-to-pulmonary shunts. *Computer Methods in Biomechanics & Biomedical Engineering*, 5(3):243–248, 2002.

[120] Francesco Migliavacca, Giancarlo Pennati, Gabriele Dubini, Roberto Fumero, Riccardo Pietrabissa, Gonzalo Urcelay, Edward L Bove, Tain-Yen Hsia, and Marc R de Leval. Modeling of the norwood circulation: effects of shunt size, vascular resistances, and heart rate. *American Journal of Physiology-Heart and Circulatory Physiology*, 280(5):H2076–H2086, 2001.

[121] Gerald E. Miller. Chapter 14 - biomedical transport processes. In John D. Enderle and Joseph D. Bronzino, editors, *Introduction to Biomedical Engineering (Third Edition)*, Biomedical Engineering, pages 937–993. Academic Press, Boston, third edition edition, 2012.

[122] Mehran Mirramezani, Scott L Diamond, Harold I Litt, and Shawn C Shadden. Reduced order models for transstenotic pressure drop in the coronary arteries. *Journal of biomechanical engineering*, 141(3):031005, 2019.

[123] Rajat Mittal, Jung Hee Seo, Vijay Vedula, Young J Choi, Hang Liu, H Howie Huang, Saurabh Jain, Laurent Younes, Theodore Abraham, and Richard T George. Computational modeling of cardiac hemodynamics: current status and future outlook. *Journal of Computational Physics*, 305:1065–1082, 2016.

[124] Bhavik N Modi, Sethuraman Sankaran, Hyun Jin Kim, Howard Ellis, Campbell Rogers, Charles A Taylor, Ronak Rajani, and Divaka Perera. Predicting the physiological effect of revascularization in serially diseased coronary arteries: clinical validation of a novel ct coronary angiography–based technique. *Circulation: cardiovascular interventions*, 12(2):e007577, 2019.

[125] Mahdi Esmaily Moghadam, Yuri Bazilevs, Tain-Yen Hsia, Irene E Vignon-Clementel, Alison L Marsden, et al. A comparison of outlet boundary treatments for prevention of backflow divergence with relevance to blood flow simulations. *Computational Mechanics*, 48(3):277–291, 2011.

[126] Mahdi Esmaily Moghadam, Francesco Migliavacca, Irene E Vignon-Clementel, Tain-Yen Hsia, and Alison L Marsden. Optimization of shunt placement for the norwood surgery using multi-domain modeling. *Journal of biomechanical engineering*, 134(5):051002, 2012.

[127] Mahdi Esmaily Moghadam, Irene E Vignon-Clementel, Richard Figliola, Alison L Marsden, Modeling of Congenital Hearts Alliance (MOCHA) Investigators, et al. A modular numerical method for implicit 0d/3d coupling in cardiovascular finite element simulations. *Journal of Computational Physics*, 244:63–79, 2013.

[128] Ryan A Moore, Kyle W Riggs, Soultana Kourtidou, Kristen Schneider, Nicholas Szugye, Weston Troja, Gavin D'Souza, Mantosh Rattan, Roosevelt Bryant III, Michael D Taylor, et al. Three-dimensional printing and virtual surgery for congenital heart procedural planning. *Birth defects research*, 110(13):1082–1090, 2018.

[129] Clinton D Morgan, Michael S Wolf, Truc M Le, Chevis N Shannon, John C Wellons, and Bret A Mettler. Cerebral ventriculomegaly after the bidirectional glenn (bdg) shunt: a single-institution retrospective analysis. *Child's Nervous System*, 31(11):2131–2134, 2015.

[130] Paul D Morris, Andrew Narracott, Hendrik von Tengg-Kobligk, Daniel Alejandro Silva Soto, Sarah Hsiao, Angela Lungu, Paul Evans, Neil W Bressloff, Patricia V Lawford, D Rodney Hose, et al. Computational fluid dynamics modelling in cardiovascular medicine. *Heart*, 102(1):18–28, 2016.

[131] JP Mynard, MR Davidson, DJ Penny, and JJ2946553 Smolich. A simple, versatile valve model for use in lumped parameter and one-dimensional cardiovascular models. *International Journal for Numerical Methods in Biomedical Engineering*, 28(6-7):626–641, 2012.

[132] William I Norwood, James K Kirklin, and Stephen P Sanders. Hypoplastic left heart

syndrome: experience with palliative surgery. *The American journal of cardiology*, 45(1):87–91, 1980.

[133] William I Norwood, Peter Lang, AR Casteneda, and DN Campbell. Experience with operations for hypoplastic left heart syndrome. *The Journal of thoracic and cardiovascular surgery*, 82(4):511–519, 1981.

[134] Ozan Oktay, Enzo Ferrante, Konstantinos Kamnitsas, Mattias Heinrich, Wenjia Bai, Jose Caballero, Stuart A Cook, Antonio De Marvao, Timothy Dawes, Declan P O'Regan, et al. Anatomically constrained neural networks (acnns): application to cardiac image enhancement and segmentation. *IEEE transactions on medical imaging*, 37(2):384–395, 2017.

[135] Ufuk Olgac, Dimos Poulikakos, Stefan C Saur, Hatem Alkadhi, and Vartan Kurtcuoglu. Patient-specific three-dimensional simulation of ldl accumulation in a human left coronary artery in its healthy and atherosclerotic states. *American Journal of Physiology-Heart and Circulatory Physiology*, 296(6):H1969–H1982, 2009.

[136] Marco Pahor, Marshall B Elam, Robert J Garrison, Stephen B Kritchevsky, and William B Applegate. Emerging noninvasive biochemical measures to predict cardiovascular risk. *Archives of internal medicine*, 159(3):237–245, 1999.

[137] Nikos Paragios. A variational approach for the segmentation of the left ventricle in cardiac image analysis. *International Journal of Computer Vision*, 50:345–362, 2002.

[138] Salvatore Pasta, Giovanni Gentile, Giuseppe M Raffa, Francesco Scardulla, Diego Bellavia, Angelo Luca, Michele Pilato, and Cesare Scardulla. Three-dimensional parametric modeling of bicuspid aortopathy and comparison with computational flow predictions. *Artificial organs*, 41(9):E92–E102, 2017.

[139] Kerem Pekkan, Brian Whited, Kirk Kanter, Shiva Sharma, Diane De Zelicourt, Kartik Sundareswaran, David Frakes, Jarek Rossignac, and Ajit P Yoganathan. Patient-

specific surgical planning and hemodynamic computational fluid dynamics optimization through free-form haptic anatomy editing tool (surgem). *Medical & biological engineering & computing*, 46:1139–1152, 2008.

[140] Caroline Petitjean and Jean-Nicolas Dacher. A review of segmentation methods in short axis cardiac mr images. *Medical image analysis*, 15(2):169–184, 2011.

[141] Orlando Petrucci, Philip R Khoury, Peter B Manning, and Pirooz Eghtesady. Outcomes of the bidirectional glenn procedure in patients less than 3 months of age. *The Journal of thoracic and cardiovascular surgery*, 139(3):562–568, 2010.

[142] Martin R Pfaller, Jonathan Pham, Aekaansh Verma, Luca Pegolotti, Nathan M Wilson, David W Parker, Weiguang Yang, and Alison L Marsden. Automated generation of 0d and 1d reduced-order models of patient-specific blood flow. *International journal for numerical methods in biomedical engineering*, 38(10):e3639, 2022.

[143] Ara K Pridjian, Alan M Mendelsohn, Flavian M Lupinetti, Robert H Beekman III, Macdonald Dick II, Gerald Serwer, and Edward L Bove. Usefulness of the bidirectional glenn procedure as staged reconstruction for the functional single ventricle. *The American journal of cardiology*, 71(11):959–962, 1993.

[144] Alfio Quarteroni and Alessandro Veneziani. Analysis of a geometrical multiscale model based on the coupling of ode and pde for blood flow simulations. *Multiscale Modeling & Simulation*, 1(2):173–195, 2003.

[145] Alfio Quarteroni, Alessandro Veneziani, and Christian Vergara. Geometric multiscale modeling of the cardiovascular system, between theory and practice. *Computer Methods in Applied Mechanics and Engineering*, 302:193–252, 2016.

[146] W. Rodi, J. H. Ferziger, M. Breuer, and M. Pourquie´e. Status of Large Eddy Simulation: Results of a Workshop. *Journal of Fluids Engineering*, 119(2):248–262, 06 1997.

[147] Tony J. Rouphael. Chapter 4 - system nonlinearity. In Tony J. Rouphael, editor, *Wireless Receiver Architectures and Design*, pages 179–261. Academic Press, Boston, 2014.

[148] Rodrigo Ruano, Mariane de Fatima Yukie Maeda, Juliana Ikeda Niigaki, and Marcelo Zugaib. Pulmonary artery diameters in healthy fetuses from 19 to 40 weeks' gestation. *Journal of ultrasound in medicine*, 26(3):309–316, 2007.

[149] Youcef Saad and Martin H. Schultz. Gmres: A generalized minimal residual algorithm for solving nonsymmetric linear systems. *SIAM Journal on Scientific and Statistical Computing*, 7(3):856–869, 1986.

[150] Sethuraman Sankaran, Mahdi Esmaily Moghadam, Andrew M Kahn, Elaine E Tseng, Julius M Guccione, and Alison L Marsden. Patient-specific multiscale modeling of blood flow for coronary artery bypass graft surgery. *Annals of biomedical engineering*, 40:2228–2242, 2012.

[151] Francesco Scardulla, Salvatore Pasta, Leonardo D'Acquisto, Sergio Sciacca, Valentina Agnese, Christian Vergara, Alfio Quarteroni, Francesco Clemenza, Diego Bellavia, and Michele Pilato. Shear stress alterations in the celiac trunk of patients with a continuous-flow left ventricular assist device as shown by in-silico and in-vitro flow analyses. *The Journal of Heart and Lung Transplantation*, 36(8):906–913, 2017.

[152] Robert W Schrier and William T Abraham. Hormones and hemodynamics in heart failure. *New England Journal of Medicine*, 341(8):577–585, 1999.

[153] Jeanette Schulz-Menger, David A Bluemke, Jens Bremerich, Scott D Flamm, Mark A Fogel, Matthias G Friedrich, Raymond J Kim, Florian von Knobelsdorff-Brenkenhoff, Christopher M Kramer, Dudley J Pennell, et al. Standardized image

interpretation and post-processing in cardiovascular magnetic resonance-2020 update. *Journal of Cardiovascular Magnetic Resonance*, 22(1):1–22, 2020.

[154] Erica L Schwarz, Luca Pegolotti, Martin R Pfaller, and Alison L Marsden. Beyond cfd: Emerging methodologies for predictive simulation in cardiovascular health and disease. *Biophysics Reviews*, 4(1), 2023.

[155] Farzin Shakib. *Finite element analysis of the compressible Euler and Navier-Stokes equations*. PhD thesis, Stanford University, 1989. Copyright - Database copyright ProQuest LLC; ProQuest does not claim copyright in the individual underlying works; Last updated - 2023-02-23.

[156] Farzin Shakib, Thomas JR Hughes, and Zdeněk Johan. A new finite element formulation for computational fluid dynamics: X. the compressible euler and navier-stokes equations. *Computer Methods in Applied Mechanics and Engineering*, 89(1-3):141–219, 1991.

[157] Jessica K Shang, Mahdi Esmaily, Aekaansh Verma, Olaf Reinhartz, Richard S Figliola, Tian-Yen Hsia, Jeffrey A Feinstein, and Alison L Marsden. Patient-specific multiscale modeling of the assisted bidirectional glenn. *The Annals of thoracic surgery*, 107(4):1232–1239, 2019.

[158] Chunli Shao, Jingjia Wang, Jian Tian, and Yi-da Tang. Coronary artery disease: from mechanism to clinical practice. *Coronary Artery Disease: Therapeutics and Drug Discovery*, pages 1–36, 2020.

[159] Leslee J Shaw, James K Min, Rory Hachamovitch, Eric D Peterson, Robert C Hendel, Pamela K Woodard, Daniel S Berman, and Pamela S Douglas. Cardiovascular imaging research at the crossroads. *JACC: Cardiovascular Imaging*, 3(3):316–324, 2010.

[160] Jerold S Shinbane and Leslie A Saxon. Virtual medicine: Utilization of the advanced

cardiac imaging patient avatar for procedural planning and facilitation. *Journal of Cardiovascular Computed Tomography*, 12(1):16–27, 2018.

[161] Frederic Sicot, Guillaume Dufour, and Nicolas Gourdain. A time-domain harmonic balance method for rotor/stator interactions. *J. Turbomach.*, 134(1):011001, 2012.

[162] Min-Ho Song, Masaru Sato, and Yuichi Ueda. Three-dimensional simulation of the blalock-taussig shunt using computational fluid dynamics. *Surgery today*, 31(8):688–694, 2001.

[163] Zoran Stankovic, Bradley D Allen, Julio Garcia, Kelly B Jarvis, and Michael Markl. 4d flow imaging with mri. *Cardiovascular diagnosis and therapy*, 4(2):173, 2014.

[164] Keith Stein, Tayfun Tezduyar, and Richard Benney. Mesh moving techniques for fluid-structure interactions with large displacements. *J. Appl. Mech.*, 70(1):58–63, 2003.

[165] David A Steinman, Yiemeng Hoi, Paul Fahy, Liam Morris, Michael T Walsh, Nicolas Aristokleous, Andreas S Anayiotos, Yannis Papaharilaou, Amirhossein Arzani, Shawn C Shadden, et al. Variability of computational fluid dynamics solutions for pressure and flow in a giant aneurysm: the asme 2012 summer bioengineering conference cfd challenge. *Journal of biomechanical engineering*, 135(2), 2013.

[166] A. Suarez, S. Sancho, and F. Ramirez. Chapter 3 - nonlinear analysis and design of oscillator circuits. In Antonio Raffo and Giovanni Crupi, editors, *Microwave Wireless Communications*, pages 65–133. Academic Press, 2016.

[167] Salvatore P Sutera and Richard Skalak. The history of poiseuille's law. *Annual review of fluid mechanics*, 25(1):1–20, 1993.

[168] Kenji Takizawa, Tayfun E Tezduyar, and Yuto Otoguro. Stabilization and discontinuity-capturing parameters for space–time flow computations with finite

element and isogeometric discretizations. *Computational Mechanics*, 62:1169–1186, 2018.

[169] C.A. Taylor and C.A. Figueroa. Patient-specific modeling of cardiovascular mechanics. *Annual Review of Biomedical Engineering*, 11(1):109–134, 2009.

[170] Charles A Taylor and Mary T Draney. Experimental and computational methods in cardiovascular fluid mechanics. *Annu. Rev. Fluid Mech.*, 36(1):197–231, 2004.

[171] Charles A. Taylor, Mary T. Draney, Joy P. Ku, David Parker, Brooke N. Steele, Ken Wang, and Christopher K. Zarins. Predictive medicine: Computational techniques in therapeutic decision-making. *Computer Aided Surgery*, 4(5):231–247, 1999.

[172] Charles A. Taylor, Timothy A. Fonte, and James K. Min. Computational fluid dynamics applied to cardiac computed tomography for noninvasive quantification of fractional flow reserve. *Journal of the American College of Cardiology*, 61(22):2233–2241, 2013.

[173] Charles A Taylor, Thomas JR Hughes, and Christopher K Zarins. Finite element modeling of blood flow in arteries. *Computer methods in applied mechanics and engineering*, 158(1-2):155–196, 1998.

[174] Charles A Taylor, Thomas JR Hughes, and Christopher K Zarins. Finite element modeling of three-dimensional pulsatile flow in the abdominal aorta: relevance to atherosclerosis. *Annals of biomedical engineering*, 26:975–987, 1998.

[175] Christian Tesche, Carlo N De Cecco, Stefan Baumann, Matthias Renker, Tindal W McLaurin, Taylor M Duguay, Richard R Bayer 2nd, Daniel H Steinberg, Katharine L Grant, Christian Canstein, et al. Coronary ct angiography–derived fractional flow reserve: machine learning algorithm versus computational fluid dynamics modeling. *Radiology*, 288(1):64–72, 2018.

[176] Tayfun Tezduyar and Sunil Sathe. Stabilization parameters in supg and pspg formulations. *Journal of computational and applied mechanics*, 4(1):71–88, 2003.

[177] Tayfun E Tezduyar. Stabilized finite element formulations for incompressible flow computations. *Advances in applied mechanics*, 28:1–44, 1991.

[178] Tayfun E Tezduyar and Yasuo Osawa. Finite element stabilization parameters computed from element matrices and vectors. *Computer Methods in Applied Mechanics and Engineering*, 190(3-4):411–430, 2000.

[179] Tayfun E. Tezduyar and Sunil Sathe. Modelling of fluid–structure interactions with the space–time finite elements: Solution techniques. *International Journal for Numerical Methods in Fluids*, 54(6-8):855–900, 2007.

[180] G. Troianowski, C. A. Taylor, J. A. Feinstein, and I. E. Vignon-Clementel. Three-Dimensional Simulations in Glenn Patients: Clinically Based Boundary Conditions, Hemodynamic Results and Sensitivity to Input Data. *Journal of Biomechanical Engineering*, 133(11):111006, 12 2011.

[181] Phillip M Trusty, Timothy C Slesnick, Zhenglun Alan Wei, Jarek Rossignac, Kirk R Kanter, Mark A Fogel, and Ajit P Yoganathan. Fontan surgical planning: previous accomplishments, current challenges, and future directions. *Journal of cardiovascular translational research*, 11:133–144, 2018.

[182] Connie W Tsao, Aaron W Aday, Zaid I Almarzooq, Cheryl AM Anderson, Pankaj Arora, Christy L Avery, Carissa M Baker-Smith, Andrea Z Beaton, Amelia K Boehme, Alfred E Buxton, et al. Heart disease and stroke statistics—2023 update: a report from the american heart association. *Circulation*, 147(8):e93–e621, 2023.

[183] Adam Updegrove, Nathan M Wilson, Jameson Merkow, Hongzhi Lan, Alison L Marsden, and Shawn C Shadden. Simvascular: an open source pipeline for cardiovascular simulation. *Annals of biomedical engineering*, 45:525–541, 2017.

[184] FN Van de Vosse, J De Hart, CHGA Van Oijen, D Bessems, TWM Gunther, A Segal, BJBM Wolters, JMA Stijnen, and FPT Baaijens. Finite-element-based computational methods for cardiovascular fluid-structure interaction. *Journal of engineering mathematics*, 47:335–368, 2003.

[185] Aekaansh Verma, Mahdi Esmaily, Jessica Shang, Richard Figliola, Jeffrey A Feinstein, Tain-Yen Hsia, and Alison L Marsden. Optimization of the assisted bidirectional glenn procedure for first stage single ventricle repair. *World Journal for Pediatric and Congenital Heart Surgery*, 9(2):157–170, 2018.

[186] I.E. Vignon-Clementel, C.A. Figueroa, K.E. Jansen, and C.A. Taylor. Outflow boundary conditions for three-dimensional simulations of non-periodic blood flow and pressure fields in deformable arteries. *Computer Methods in Biomechanics and Biomedical Engineering*, 13(5):625–640, 2010.

[187] Irene E. Vignon-Clementel, C. Alberto Figueroa, Kenneth E. Jansen, and Charles A. Taylor. Outflow boundary conditions for three-dimensional finite element modeling of blood flow and pressure in arteries. *Computer Methods in Applied Mechanics and Engineering*, 195(29):3776–3796, 2006. Absorbing Boundary Conditions.

[188] Salim S Virani, Alvaro Alonso, Emelia J Benjamin, Marcio S Bittencourt, Clifton W Callaway, April P Carson, Alanna M Chamberlain, Alexander R Chang, Susan Cheng, Francesca N Delling, et al. Heart disease and stroke statistics—2020 update: a report from the american heart association. *Circulation*, 141(9):e139–e596, 2020.

[189] Wolfgang A Wall. Fluid-struktur-interaktion mit stabilisierten finiten elementen. *02 Fakultät Bau- und Umweltingenieurwissenschaften*, 1999.

[190] Xuechuan Wang, Xiaokui Yue, Honghua Dai, Haoyang Feng, and Satya N. Atluri. Chapter 2 - harmonic balance method and time domain collocation method. In

Xuechuan Wang, Xiaokui Yue, Honghua Dai, Haoyang Feng, and Satya N. Atluri, editors, *Computational Methods for Nonlinear Dynamical Systems*, pages 27–54. Elsevier, 2023.

[191] Xuguang Wang, Monu Jaiswal, Ashton M Corpuz, Shashwot Paudel, Aditya Balu, Adarsh Krishnamurthy, Jinhui Yan, and Ming-Chen Hsu. Photogrammetry-based computational fluid dynamics. *Computer Methods in Applied Mechanics and Engineering*, 417:116311, 2023.

[192] Jacek Waniewski, Weronika Kurowska, Jeremi K Mizerski, Anna Trykozko, Krzysztof Nowiński, Grażyna Brzezińska-Rajszys, and Andrzej Kościesza. The effects of graft geometry on the patency of a systemic-to-pulmonary shunt: A computational fluid dynamics study. *Artificial organs*, 29(8):642–650, 2005.

[193] Girish Warrier, Baiju Sasi Dharan, Sajan Koshy, Shenoj Kumar, Shivaprakasha Krishnanaik, and Suresh Gururaja Rao. Bidirectional glenn operation in infancy. *Indian Journal of Thoracic and Cardiovascular Surgery*, 20(4):159–163, 2004.

[194] Nathan M Wilson, Ana K Ortiz, and Allison B Johnson. The vascular model repository: a public resource of medical imaging data and blood flow simulation results. *Journal of medical devices*, 7(4):040923, 2013.

[195] K Yamakoshi. Non-invasive cardiovascular hemodynamic measurements. *Sensors in medicine and health care: Sensors applications*, 3:107–160, 2004.

[196] Liang Zhong, Jun-Mei Zhang, Boyang Su, Ru San Tan, John C Allen, and Ghassan S Kassab. Application of patient-specific computational fluid dynamics in coronary and intra-cardiac flow simulations: Challenges and opportunities. *Frontiers in physiology*, 9:742, 2018.

[197] Jian Zhou, Mahdi Esmaily-Moghadam, Timothy A Conover, Tain-Yen Hsia, Alison L Marsden, Richard S Figliola, MOCHA Investigators, et al. In vitro assess-

ment of the assisted bidirectional glenn procedure for stage one single ventricle repair. *Cardiovascular engineering and technology*, 6(3):256–267, 2015.